UNIVERSITY OF SOUTHAMPTON

Faculty of Engineering and Physical Sciences
Institute of Sound and Vibration Research

Aerodynamic and Aeroacoustics Characterisation of Tip Leakage Flow

by

Ivan Saraceno

BSc, MSc

ORCiD: 0000-0003-1193-8427

A thesis for the degree of
Doctor of Philosophy

June 2025

University of Southampton

Abstract

Faculty of Engineering and Physical Sciences
Institute of Sound and Vibration Research

Doctor of Philosophy

Aerodynamic and Aeroacoustics Characterisation of Tip Leakage Flow

by Ivan Saraceno

Among the various noise sources related to ducted fans, the noise generated by the interaction of tip leakage flow with the blade's geometric singularities is one of the least understood. This thesis deals with identifying the mechanisms involved in the generation and reduction of tip leakage noise for a single stationary aerofoil, which enables a detailed analysis of this specific noise source. Through a combination of experimental, parametric, and numerical investigations, this research explores the fluid dynamic instabilities responsible for the noise sources, the key parameters influencing these sources, and the effectiveness of noise-reducing treatments. Two dipole-type noise sources were identified and attributed to fluid-dynamic instabilities occurring in the tip-gap region: roll-up and shedding of vortical structures generated during the separation of the flow at the pressure side tip edge. The key non-dimensional parameters influencing these noise sources include the geometric angle of attack, the ratio of maximum aerofoil thickness to gap size, and the ratio of gap size to boundary layer thickness of the bottom wall. This investigation also examines the impact of treatments such as porous material and rounded pressure side tip edge, with both treatments leading to significant noise reductions. Finally, numerical simulations provide a definitive understanding of the tip leakage flow, confirming the presence of instabilities also for the configuration with a rounded pressure side tip.

Contents

Declaration of Authorship

I declare that this thesis and the work presented in it is my own and has been generated by me as the result of my own original research.

I confirm that:

1. This work was done wholly or mainly while in candidature for a research degree at this University;
2. Where any part of this thesis has previously been submitted for a degree or any other qualification at this University or any other institution, this has been clearly stated;
3. Where I have consulted the published work of others, this is always clearly attributed;
4. Where I have quoted from the work of others, the source is always given. With the exception of such quotations, this thesis is entirely my own work;
5. I have acknowledged all main sources of help;
6. Where the thesis is based on work done by myself jointly with others, I have made clear exactly what was done by others and what I have contributed myself;
7. Parts of this work have been published and the list has been indicated in chapter 1 of the thesis.

Signed:..... Date:.....

Acknowledgements

Throughout my PhD, I encountered various dualities, starting from the two tip leakage noise sources, the different approaches of my two supervisors, the dualism between experimental and numerical methods, my involvement in both acoustic and fluid-dynamic groups, and the transition from working from home to being in the office. This introduction sets the stage for the following acknowledgments.

First and foremost, I would like to express my gratitude to both my supervisors Bharath and Chaitanya, for allowing me to see problems from both of your perspectives, which has enriched my understanding immensely. Thank you, Bharath, for choosing me at the start of the Covid, and thank you, Chaitanya, for the infinite support and kindness, which has left me speechless from the beginning. I am truly grateful to have met you.

I would also like to thank Prateek for his patience in answering all my questions. The two months we spent in the lab doing PIV were some of the best moments of my PhD. Thanks also to Stephane for hosting me in Sherbrooke. I still fondly remember our first dinner together, discussing for hours about everything.

I would like to thank my office colleagues, Edo, Long, JSP, RamRamRam and Sergi. Being with you for the last two years has made me realize how much I missed during the first two years of working from home. Thanks to the Aero-Astro colleagues, Craig, Hylia, Murillo, Marco and Tak. I have truly enjoyed every conversation with each of you. Thanks to Canada-colleagues, Andrea, Antonio, Jose, and Zi for making me feel part of a group before even starting.

Additionally, I am thankful to Phil J. for the positive energy he brings every time we meet. I would also like to extend my thanks to Alan, Marlene and Mike Street for their support.

Finally, I am also thankful to the people I met during this PhD journey, including the olden hours members, Giulia, and ISVR friends in particular Esma and Fra, Jona, Renato and Rocio. I would like to thank my parents, my dual-twin sister and Mariano, my cousins, my lifelong friends of Napoli, Lorenza and Peppe, and V. I would not be the person I am without you.

And to my hero. That's who I chase.
When I was 15 years old I had a very important person in my life come and ask me 'Who's your hero?'
'I thought about it and it's me in ten years', I said.
So I turned 25 ten years later and that same person comes to me and goes, 'Are you a hero?'
I said, 'Not even close!' She said why and I said, 'My hero is me at 35.'
You see, every day, and every week, and every month, and every year of my life, my hero is always ten years away. I'm never going to be my hero. I'm not going to obtain that and that's fine with me because it keeps me with somebody to keep on chasing.

Matthew McConaughey. Oscar acceptance, 2014.

Nomenclature

Abbreviations

BPF	Blade Passing Frequency
CFL	Courant-Friedrichs-Lewy
DMD	Dynamic Mode Decomposition
FW-H	Ffowcs Williams and Hawkings
HWA	Hot-Wire Anemometry
IL	Insertion Loss
LBM	Lattice Boltzmann method
LES	Large Eddy Simulation
NACA	National Advisory Committee for Aeronautics
LW	Law-Wendroff
OASPL	Overall Sound Pressure Level
OGV	Outlet Guide Vane
OTR	Over-Tip-Rotor
PIV	Particle Image Velocimetry
POD	Proper Orthogonal Decomposition
RANS	Reynolds-Averaged Navier-Stokes
SPL	Sound Pressure Level
SPOD	Spectral Proper Orthogonal Decomposition
rms	root mean square
TCRV	Tip Counter-Rotating Vortex
TLV	Tip Leakage Vortex
TSV	Tip Separation Vortex

Roman Symbols

b	shear layer thickness
B	number of blades
c	chord
C_D	drag coefficient
C_l	lift coefficient at the tip
C_L	lift coefficient
C_p	pressure coefficient
C_{P_s}	pressure peak on the suction side

C_{xy}	coherence
D	drag
e	gap size
f	frequency
L	lift
M	Mach number
$\overline{p'^2}$	pressure fluctuations
Re	Reynolds number
S	relevant surface area
S_{pp}	Power Spectral Density
St_b	Strouhal number based on the shear layer thickness b
St_c	Strouhal number based on the chord c
St_v	Strouhal number based on the width of the separated flow v
t	thickness of the aerofoil treatment
U_c	convective velocity
U_0	inflow velocity
U_{SL}	shear layer velocity
v	width of the separated flow at the gap exit
V_L	tip leakage velocity
x, y, z	cartesian coordinates

Greek Symbols

α	geometric angle of attack
α_{eff}	effective angle of attack
δ	boundary layer thickness
λ	wavelength
ϕ	phase difference
ρ	air density
θ	polar angle
σ	contraction ratio
σ_{por}	porosity
Ω	shaft rotation rate
τ	local aerofoil thickness
τ_{max}	maximum aerofoil thickness

Chapter 1

Introduction

1.1 Context

As air traffic continues to grow, aircraft noise has become a significant concern for populations living near airports due to its annoyance and potential health impacts. In response, the Advisory Council for Aviation Research and Innovation in Europe set a new target for the year 2050: reducing the perceived noise emissions of aircraft by 65% compared to those of a typical new aircraft in 2000 (Collin et al., 2016).

The main contributors to aircraft noise are the airframe and the engine. Airframe noise is generated by the interaction of airflow with structural components such as the wings, trailing edge, slats, flaps and landing gears. The most commonly used engine in commercial aviation is the turbofan, with primary noise sources generated by the jet, ducted fan, combustor, compressor, and turbine. The contribution of each engine component has changed over the years. Increasing the bypass ratio has reduced jet speed and, consequently, jet noise (Lockard and Lilley, 2004). Compressor and turbine noise are significant at low power settings, particularly in the stages nearest the inlet and outlet core (Hubbard, 1991). In modern high-bypass-ratio turbofans, fan noise dominates during approach and take-off, along with jet noise (Moreau and Roger, 2018).

1.1.1 Fan noise sources: Summary

Turbofan noise can be decomposed into tonal and broadband components. Tonal noise is associated with the periodic rotation of the rotor blades, while broadband noise arises from random fluctuating phenomena, such as turbulent boundary layers and wakes in all rotating stages. Figure 1.1 illustrates the fan noise sources, with tonal and broadband mechanisms represented in green and blue, respectively. The primary tonal and broadband fan noise sources are detailed in the following section, as reported by Peake and Parry (2012).

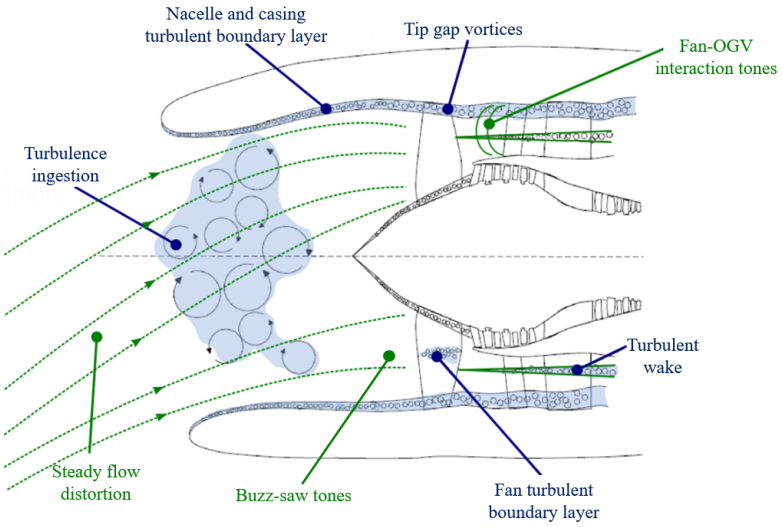

Figure 1.1: Fan noise sources: tonal mechanisms are highlighted in green, broadband sources in blue, from Moreau (2019).

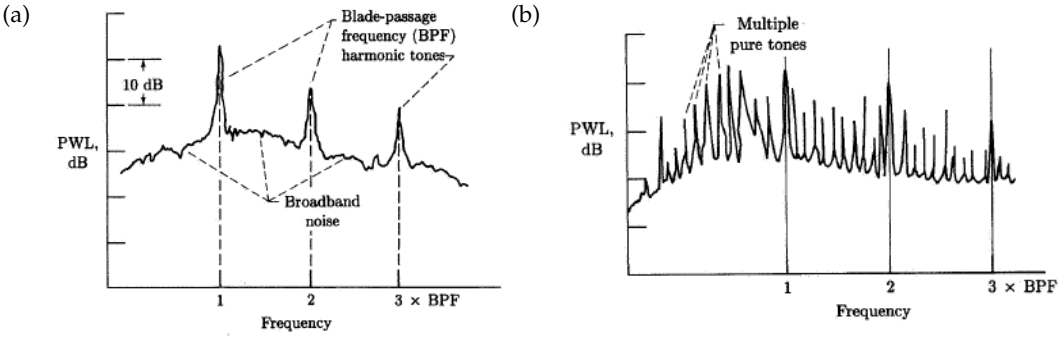

Figure 1.2: Typical turbomachinery sound power spectra for tip with subsonic (a) and supersonic (b) speed, from Hubbard (1991).

Tonal

- **Fan self-noise**: Fan self-noise is generated by periodic lift forces exerted by the rotating blades on the fluid. Each time a blade completes a revolution, it generates a disturbance. A fan with B blades generates noise at multiples of the Blade Passing Frequency (BPF), defined as $B\Omega$, where Ω is the shaft rotation rate. However, this noise is not radiated at subsonic fan tip Mach numbers (e.g., 0.8 during approach). Noise generation occurs when supersonic tip Mach numbers are present (e.g., 1.5 during take-off). In this case, noise is not limited to multiples of the BPF, but also occurs at all multiples of the shaft rotation frequency, as the shocks are particularly sensitive to the non-uniformities of the fan blades. This phenomenon, known as buzz-saw noise, is illustrated in figure 1.2 (b), which displays a typical sound power spectrum of turbomachinery operating under supersonic conditions.

- **Fan-OGVs interaction**: the wakes produced by a fan consist of both steady mean components and unsteady fluctuating components. As these wakes are convected downstream and interact with the Outlet Guide Vanes (OGVs), the steady components contribute to tonal noise at multiples of the Blade Passing Frequency (BPF), while the unsteady components produce broadband noise. Both tonal and broadband components are illustrated in Figure 1.2 (a), which shows a typical sound power spectrum of turbomachinery operating with subsonic tip speed.

- **Steady flow distortion**: The upstream flow impinging on the fan is not circumferentially uniform, resulting in load variations on the fan blades that generate tonal noise. This phenomenon arises from the non-zero angle of incidence to the nacelle axis and the asymmetric nacelle geometry, which is often drooped or scarfed (Astley et al., 2014).

Broadband

- **Fan self-noise**: The aerofoil trailing edges are well-known sources of high-frequency broadband noise, which is generated when the boundary layer eddies on the fan blades interact with the trailing edge. This phenomenon has been extensively studied over the years, from Amiet (1975) to Lee et al. (2021).

  Fan self-noise is sensitive to rotor tip clearance (Ganz et al., 1998), suggesting the presence of an additional noise mechanism caused by the interaction between the tip leakage flow and blade tip geometric singularities. An overview of the noise generated by the tip leakage flow, which is the focus of this thesis, is provided in Section 1.1.2.

- **Fan-boundary layer interaction**: The fan blade tips are immersed in the boundary layer of the casing wall due to the typical small clearance between the fan and casing wall. Therefore, broadband noise is generated from the interaction between turbulent eddies and the blade surfaces. This noise component can be mitigated by applying wall suction upstream of the fan.

- **Fan-OGVs interaction**: As mentioned earlier, the fan wakes contain turbulent fluctuating components that, when interacting with the OGVs, produce broadband noise. This noise is a significant source, comparable to fan self-noise, and becomes the dominant one for frequencies above 5 kHz, according to the measurements conducted by Ganz et al. (1998) on a low-speed scale fan rig.

- **Turbulence ingestion**: The interaction between the turbulent structures of the free stream with the leading edge of the fan blades induces broadband noise.

1.1.2 Tip leakage noise: an Overview

The tip leakage noise arises from the interaction between the blade tip singularities, the casing wall boundary layer, and the tip leakage flow. This flow is three-dimensional and unsteady, occurring within the gap between the blade tip and the duct wall. It is generated by the relative motion between the blade tip and the casing wall, as well as by the pressure difference between the suction side and pressure side of a blade. The tip flow further interacts with the incoming flow, leading to the formation of a vortex structure known as Tip Leakage Vortex (TLV).

The clearance between the fan rotor and the casing wall is typically small, on the order of millimetres. In a test conducted on a Boeing 18-inch fan rig (Ganz et al., 1998), three clearance sizes were analysed: a small configuration with a mid-chord static gap of 0.50 mm, a medium configuration with 0.89 mm, and a large case with 1.27 mm. The ratio of clearance to mid-chord blade height was 0.5% for the small, 0.8% for the medium, and 1.1% for the large. This range of ratios is consistent with typical high-bypass engine fan operation. Four tip clearances were considered in an experimental campaign conducted on a 22-inch fan model by NASA and General Electric Aircraft Engines, as reported by Hughes et al. (2005). These tip gaps were: 0.00 mm (representing newly manufactured engines, as defined by GEAE), 0.50 mm (0.54% of chord, typical of an engine near a maintenance cycle), 0.76 mm (0.83% of chord, characteristic of an engine after hard manoeuvring), and 1.06 mm (1.15% of chord, typical of an engine after a severe landing). The fan tip clearance was investigated at the fan design point of 370 m/s.

The tip leakage area is where three potential broadband noise sources are present: tip leakage noise, fan-boundary layer interaction noise, and trailing edge noise. While fan-boundary layer and trailing edge noise are well-studied, very few studies have focused on tip leakage noise, as it is challenging to isolate and measure in a representative fan rig. Indeed, as reported by Ganz et al. (1998), test data with little or no tip clearance and no boundary layer are needed to separate tip noise from fan noise and to remove the masking of the interaction noise. A similar approach has been followed in the current investigation. However, the operating conditions in this study, such as Mach number or tip gap sizes, detailed in Section 2, do not match those of a real engine fan. To enable flow measurements within the gap, a larger clearance-to-gap ratio of 5%, or a clearance-to-blade height ratio of 7.1%, is considered for the baseline configuration. According to Jacob et al. (2010), who developed the experimental set-up used in the current investigation, the underlying physical mechanisms of tip leakage flow and its sound radiation are similar to those observed in real fans.

1.2 Scope of the thesis

The main goal of this research project is to characterise and reduce tip leakage noise for a stationary aerofoil. Specifically, the objectives are as follows:

- To identify the mechanisms responsible for generating tip leakage noise in a single-stationary aerofoil and to characterise the tip noise sources across a wide range of tip gaps, blade loadings, flow speeds, maximum aerofoil thicknesses and inflow boundary layers in order to identify the parameters influencing them. The experimental investigation, which includes simultaneous near- and far-field pressure measurements along with flow measurement, forms the core of the study and will be complemented by numerical simulations conducted on the same setup.
- To understand the mechanisms behind the reduction of tip leakage noise source achieved by modifying the aerofoil tip using porous treatments or rounding the aerofoil edges.

1.3 Thesis Structure with original contributions

The main contributions of this thesis are outlined below, corresponding to each chapter.

- Chapter 3 deals with understanding the physical mechanisms involved in the generation of the tip leakage noise. Experiments using simultaneous flow and pressure measurements identify two dipole-type noise sources within two non-dimensional frequency ranges, $St_c = fc/U_0 = 2 - 5.5$ and $5.5 - 13$, where f is the frequency, c is the aerofoil chord length and U_0 is the inflow velocity. These noise sources are attributed to fluid-dynamic instabilities within the gap: vortex-shedding and shear layer roll-up, connected to the behaviour of the tip flow. After it separates at the pressure side tip, the shear layer rolls up, forming vortical structures of size equivalent to the shear layer thickness b at the frequency of the second noise source, which allows to define the corresponding non-dimensional frequency $St_b = fb/U_{SL}$, where U_{SL} is the shear layer velocity. Successively, the separated flow can either reattach to the aerofoil or remain separated until the gap exit. In case of extended separation, the vortical structures are shed at the frequency of the first noise source, which can be non-dimensionalised as $St_v = fv/U_0$, where v is the width of the separated flow measured at gap exit, while roll-up continues to occur.
- Chapter 4 identifies three non-dimensional parameters that influence the tip leakage noise sources: the geometric angle of attack α, the ratio between the maximum aerofoil thickness and the gap size τ_{max}/e, and the ratio between the gap

size and the boundary layer thickness of the bottom wall e/δ. A wide range of configurations, varying α, τ_{max} and e, for two distinct δ, has been experimentally investigated. The first noise source develops when $\tau_{max}/e < 4$ and with the tip leakage vortex away from the aerofoil surface for $\alpha \geq 10°$. The location of the vortex detachment from the aerofoil surface can be identified by the minimum pressure peak in the pressure distribution C_p along the aerofoil suction side tip. The magnitude of this peak, directly linked to the noise source strength, depends on the three non-dimensional parameters. The second tip noise source occurs whenever the tip flow separates at the pressure side. Its strength is mainly proportional to the lift coefficient C_l, depending on α, and it decreases as e/δ decreases and τ_{max}/e increases.

- Chapter 5 focuses on treatments to reduce tip leakage noise, including aerofoil tips treated with porous materials or by rounding the pressure side edge, along with an assessment of the associated aerodynamic losses. The porous treatment affects the tip noise sources differently: the first noise source is reduced solely through changes in the flow field, while the second source benefits from both flow field modifications and the inherent properties of porosity. Rounding the pressure side edge alters the flow field, leading to reductions in both noise sources. However, the detailed mechanisms behind these reductions are fully explored in Chapter 6. Both treatments result in worse aerodynamic performances compared to the baseline case, with drag loss influenced by τ_{max}/e and α.

- Chapter 6 numerically investigates the mechanisms behind the tip leakage noise sources, and their changes when the aerofoil pressure side tip is rounded. Large Eddy Simulations provide a novel and definitive overview of the tip flow topology, clearly highlighting the shear layer roll-up and vortex shedding in the configuration with square pressure side tip. With round tip, both instabilities persist but with lower intensity.

The experimental set-up and the measurement techniques employed in this project are described in Chapter 2, with additional details in Appendix A. Appendix B includes additional plots resulting from the numerical simulations. Notably, the literature review is integrated throughout the chapters, with each background section emphasizing past works relevant to the chapter.

1.4 Publications

Journal Papers

- S. Palleja-Cabre, *I. Saraceno*, P. Chaitanya, "On the modification of tip leakage noise sources by over-tip liners", Physics of Fluids, 2024.
- *I. Saraceno*, P. Chaitanya, P. Jaiswal, S. Palleja-Cabre, L. Wu, B. Ganapathisubramani, "On the tip leakage noise mechanisms of a stationary aerofoil", Journal of Sound and Vibration, 2025 (under review).
- *I. Saraceno*, P. Chaitanya, B. Ganapathisubramani, "The non-dimensional parameters influencing the tip leakage noise", Journal of Fluid Mechanics, 2025 (under review).
- *I. Saraceno*, P. Chaitanya, B. Ganapathisubramani, A. Alguacil, S. Moreau, M. Sanjose, 'Numerical investigation of tip leakage noise sources of aerofoils with square and round tip", (under preparation).

Conference proceedings

- *I. Saraceno*, P. Chaitanya, B. Ganapathisubramani, A. Alguacil, S. Moreau, M. Sanjose, "On the numerical investigation of the tip leakage noise sources of a stationary aerofoil", 30th AIAA/CEAS Aeroacoustics Conference, 2024.
- *I. Saraceno*, S. Palleja-Cabre, P. Chaitanya, B. Ganapathisubramani, "Influence of non-dimensional parameters on the tip leakage noise", AIAA AVIATION 2023 Forum, 2023.
- *I. Saraceno*, S. Palleja-Cabre, P. Chaitanya, P. Jaiswal, B. Ganapathisubramani, "On the tip leakage noise generating mechanisms of single-fixed aerofoil", 28th AIAA/CEAS Aeroacoustics Conference, 2022.
- S. Palleja-Cabre, *I. Saraceno*, S. Palani, P. Chaitanya, "Reduction of tip-leakage noise by using over-tip liners", 28th AIAA/CEAS Aeroacoustics Conference, 2022.
- S. Palleja-Cabre, *I. Saraceno*, P. Chaitanya, P. Joseph, "Reduction of tip-leakage noise by using porosity", 28th AIAA/CEAS Aeroacoustics Conference, 2022.

Chapter 2

Experimental set-up and flow characterisation

This chapter introduces the experimental setup, detailing the test rig and the aerofoil configurations analysed throughout the thesis. It also describes the measurement techniques employed, including steady and unsteady pressure measurements, Particle Image Velocimetry (PIV), and Hot-Wire Anemometry (HWA) to assess the flow.

2.1 Set-up

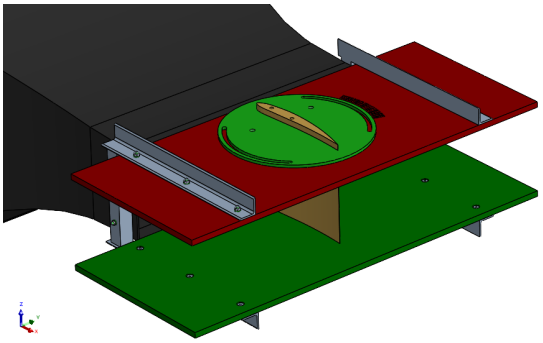

Figure 2.1: CAD model of the experimental set-up.

The set-up, which schematic is shown in figure 2.1, follows a design similar to that developed by Grilliat et al. (2007). A NACA 5510 airfoil (5% camber, 10% thickness) with a chord length of $c = 200$ mm is located in the potential core of an open-jet wind tunnel between two plexiglass plates, which are fixed at the top and the bottom of the nozzle exit. Two parameters can be modified: the gap size e between the bottom wall and the aerofoil tip, and the geometric angle of attack α, defined as the angle between the aerofoil chord line and the inflow direction. The coordinate system used

e \ α	12°	15°	20°
5 mm		P-PIV$_{\text{in}}$ HWA$_{\text{ver}}$	
10 mm	HWA$_{\text{hor}}$	S-PIV$_{\text{in}}$ P-PIV$_{\text{out}}$ HWA$_{\text{ver}}$ HWA$_{\text{hor}}$	S-PIV$_{\text{in}}$ HWA$_{\text{hor}}$
15 mm		HWA$_{\text{ver}}$	

Table 2.1: List of the configurations analysed in Chapter 3, along with the flow measurements conducted. The subscripts refer to the tip flow region assessed: "in" indicates within the tip gap region, "out" indicates outside the region above the aerofoil tip, "hor" stands for measurements in the horizontal mid-gap plane and "ver" for measurements in the vertical direction; while the capital letters P and S refer to Planar and Stereo PIV.

hereafter is based on the inflow direction: the x-axis is aligned with it, pointing from the aerofoil leading edge to the trailing edge; the y-axis is in the cross-stream direction, oriented from the pressure to the suction side; and the z-axis is oriented upwards from the bottom wall.

Chapter 3 deals with identifying the tip leakage noise source mechanisms for the NACA 5510 aerofoil. A wide range of angles of attack ($\alpha = 5°$ to $30°$) and gap size ($e = 0$ to 20 mm) were investigated. However, detailed flow measurements using HWA and PIV were performed only on six configurations, each differing from the baseline, characterised by $\alpha = 15°$ and $e = 10$ mm by changing either the gap size or the angle of attack. The details of these cases are provided in table 2.1, together with the type of flow measurements performed, which are discussed in section 2.2.2. Different inflow velocities were analysed ($U_0 = 20$ to 70 m/s). However, unless indicated, the results are presented by considering $U_0 = 40$ m/s, as the tip leakage noise is found to be a Strouhal-dependent phenomenon in Chapter 3. This results in a chord-based Reynolds number of $Re = 5.6 \times 10^5$ and a Mach number of $M = 0.12$. Moreover, at this inflow velocity, the casing boundary layer near the airfoil's leading edge is turbulent and is characterised by a thickness of approximately 5 mm.

Chapter 4 examines the influence of non-dimensional parameters on the development of tip leakage noise sources, including the angle of attack, the ratio between maximum aerofoil thickness and gap size (τ_{max}/e), and the ratio between gap size and boundary layer thickness (e/δ). To achieve this, various configurations with different maximum aerofoil thicknesses, gap sizes and angles of attack were analysed. Table 2.2 lists all the configurations analysed, obtained by combining six different NACA "XXXX" aerofoils with various gap sizes e (in mm) to achieve a specific thickness-to-gap ratio τ_{max}/e. To investigate the effect of the boundary layer thickness, the experimental set-up was slightly modified. A 2-meter-long duct was inserted between the nozzle and the aerofoil, increasing the boundary layer thickness at the aerofoil leading edge from 5 to approximately 20 mm, displayed in figure A.7 in the appendix. Only the HWA technique

	$\tau_m/e = 1$	$\tau_m/e = 2$	$\tau_m/e = 3$	$\tau_m/e = 4$	$\tau_m/e = 5$	$\tau_m/e = 6$
5505	$e = 10$	$e = 5$	$e = 3.3$	$e = 2.5$	$e = 2$	$e = 1.6$
5507	$e = 14$	$e = 7$	$e = 4.6$	$e = 3.5$	$e = 2.8$	$e = 2.3$
5510	$e = 20$	$e = 10$	$e = 6.6$	$e = 5$	$e = 4$	$e = 3.3$
5512	$e = 24$	$e = 12$	$e = 8$	$e = 6$	$e = 4.8$	$e = 4$
5515	$e = 30$	$e = 15$	$e = 10$	$e = 7.5$	$e = 6$	$e = 5$
5520		$e = 20$	$e = 13$	$e = 10$	$e = 8$	$e = 6.6$

Table 2.2: List of the configurations analysed in Chapter 4.

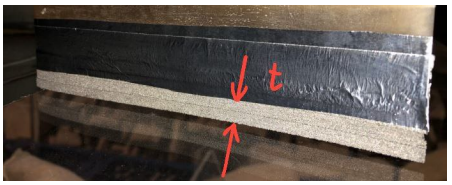

Figure 2.2: Photo of a porous tip treatment of thickness t across the entire chord.

was employed in this chapter to investigate the flow inside the gap and around the suction side region of the aerofoil.

Chapter 5 investigates aerofoil treatments, such as porous and rounded tips, aimed at reducing the tip noise sources, along with an assessment of the associated aerodynamic forces. The porous tip was manufactured from Nickel Chromium Alloy with $\sigma_{por} = 90\%$ porosity and a maximum thickness of $t = 15$ mm in the spanwise direction. Noise reductions for $\sigma_{por} = 90\%$ were found to be higher than those for $\sigma_{porous} = 50\%$ over the frequencies where the tip leakage noise is dominant (Palleja-Cabre et al., 2022). The thickness was adjusted by applying a thin metallic tape to make the surface non-porous, as shown in figure 2.2. Different round tips were designed by either modifying the pressure or the suction side, or by changing the fillet radius. Details of these designs, along with the results, are provided in the chapter.

2.2 Types of measurements

2.2.1 Pressure

Steady and unsteady pressure measurements were conducted in both near-field and far-field regions to evaluate the pressure distribution along the airfoil and the far-field noise spectra. The pressure distribution C_p over the aerofoil was evaluated by connecting surface pinholes to a pressure scanner with thin capillary tubes. These pressure taps are located 1 mm above the aerofoil tip on both aerofoil sides, at 12 different locations

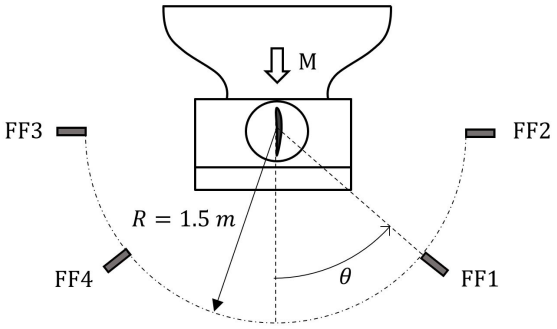

Figure 2.3: Sketch of the location of the far-field microphones

along the chord[1]. The formula used to evaluate C_p is as follows:

$$C_p(x) = \frac{p(x) - p_\infty(x)}{0.5\rho_\infty U_0^2} \tag{2.1}$$

where p_∞ is the pressure measured without flow, $\rho_\infty = 1.225$ kg/m^3 is the density and U_0 is the inflow velocity. The lift coefficient C_l is obtained by numerically integrating the pressure distributions along the chord, following:

$$C_l = \int_0^c [C_{p_p}(x) - C_{p_s}(x)]d(x) \tag{2.2}$$

where $C_{p_p}(x)$ and $C_{p_s}(x)$ represent the pressure distribution along the pressure and suction sides of the aerofoil, respectively.

Unsteady surface pressure measurements were recorded at the same 12-locations along the aerofoil and at three stations on the bottom wall, i.e. at $x/c = 25\%, 50\%$ and 75%, using FG-23329-P07 sensors, omnidirectional electret condenser microphones with 0.75 mm diaphragm. The phase spectra between two remote mics[2] allowed the estimation of the convection velocity U_c of turbulent eddies within the flow. This velocity can be determined from the gradient of the phase spectrum $d\phi_{ij}/df$ between two stream-wise pairs of sensors i and j separated by a distance $\eta_x = x_i - x_j$:

$$U_c(f) = \frac{2\pi\eta_x}{d\phi_{ij}/df} \tag{2.3}$$

as reported in Gruber (2012).

Far-field noise measurements were performed using 4 half-inch condenser microphones (B&K type 4189) located at a radial distance of 1.5 m from the aerofoil mid chord. Two microphones were placed on the aerofoil suction side, while the others on the pressure side, each one at polar angles of $\theta = \pm 90°$ and $\theta = \pm 40°$ relative to the inflow direction, as qualitatively shown in figure 2.3. However, unless indicated, the pressure spectra

[1] Surface pinholes along the aerofoil tip at $x/c = 10\%$, 20%, 30%, 45%, 47.5%, 50%, 52.5%, 55%, 60%, 75%, 80% and 90%.

[2] The remote mics need to be calibrated following the procedure reported in Appendix A.2.

reported in the current work were recorded by the microphone placed on the pressure side at $\theta = -90°$, as maximum noise levels are measured at this location. Calibration is performed with a conventional B&K calibrator (94 dB at 1 kHz).

Both near and far-field pressure signals were acquired simultaneously for 10 seconds at a sampling frequency of 50 kHz. The noise spectra are calculated with Welch's method, using a window size of 1024 data points with no overlap. This corresponds to a frequency resolution of 48.83 Hz and a bandwidth-time product of 488.3, which is sufficient to ensure a 9% uncertainty with a 95% confidence level (Glegg and Devenport, 2017).

The coherence between two pressure signals, $x(t)$ and $y(t)$, which allows for a qualitative localisation of noise sources, is defines as:

$$C_{xy}(f) = \frac{|G_{xy}(f)|^2}{G_{xx}(f)G_{yy}(f)} \tag{2.4}$$

where G_{xy} is the cross-spectral density between $x(t)$ and $y(t)$, while G_{xx} and G_{yy} are the auto spectral density of $x(t)$ and $y(t)$ respectively.

2.2.2 Velocity

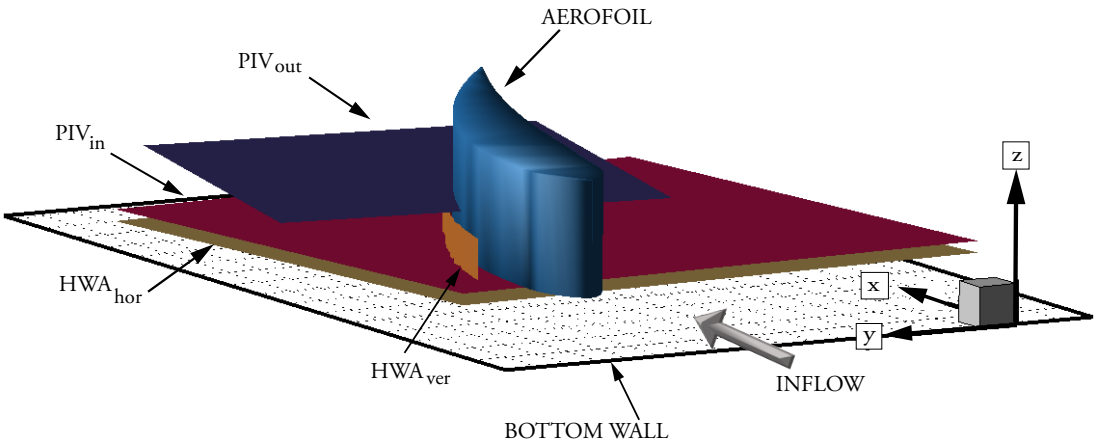

Figure 2.4: Schematic representation of the types of flow measurements conducted using PIV and HWA. The subscripts refer to the tip flow region assessed as reported in table 2.1.

The flow characteristics within the tip gap region and around the aerofoil suction side were assessed using PIV and HWA techniques, as sketched in figure 2.4 and listed in table 2.1. Stereo PIV measurements were conducted within the tip gap, at $z = 7$ mm, for the two cases characterised by $\alpha = 15°$ and 20° with a gap size $e = 10$ mm. Two planar PIV were performed:within the gap region at $z = 3$ mm, for the configuration with $\alpha = 15°$ and $e = 5$ mm, and above the tip edge at $z = 20$ mm, for the baseline

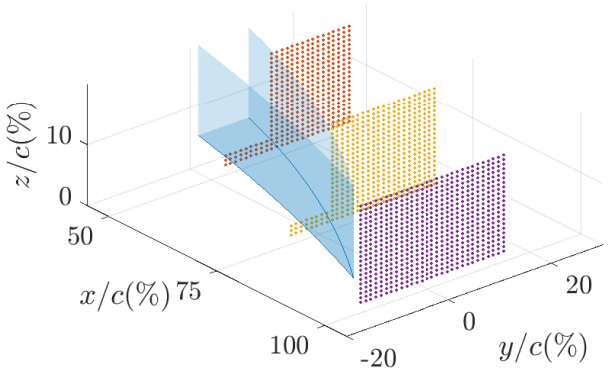

Figure 2.5: Schematic representation of the hot-wire measurement conducted at various chord-wise sections on the aerofoil suction side.

configuration with $\alpha = 15°$ and $e = 10$ mm. Stereo PIV set-up consisted of two LaVision Imager-LX 16 MegaPixel CCD cameras, each fitted with a 105 mm focal lens and located below the bottom plate. Each camera was equipped with a Scheimpflug adaptor to align the image plane with the object plane. The solid angle subtended between the two cameras is about $35°$. One camera orthogonal to the laser sheet was used in the planar cases. The PIV measurements performed inside the tip gap region are indicated in figure 2.4 as PIV_{in}, while those above the aerofoil tip as PIV_{out}.

For the stereo PIV cases, 20 sets of data, each composed of 2 x 80 image pairs (for a total of 1600 snapshots), were acquired at 0.5 Hz. For the planar PIV cases, 13 data sets, each set consisting of 150 image pairs (for a total of 1950 snapshots), were acquired at 0.7692 Hz. The light source is a Nd:YAG laser Bernoulli, which generates a dual pulsed laser sheet of 0.5 mm thickness, aligned parallel to the bottom plate. Specifically, the beam passes through pairs of spherical lenses (with -75 and 150 mm focal length) and is then expanded using a cylindrical lens (with -50 mm length). Vaporised glycerin particles, measuring almost 1 μm, are used for seeding the flow. A fog machine is placed at the inlet of the centrifugal fan, upstream of the nozzle, to ensure particles are homogeneously distributed in the flow.

A single hot-wire probe (Dantec type 55P11) was used in a midgap plane parallel to the bottom wall, and at various heights along the aerofoil suction side. In figure 2.4, the first set of measurements is denoted as HWA_{hor}, while the second one with HWA_{ver}. In the first case, the probe was oriented parallel to the x-axis to be sensitive to the resultant velocity in the $x - z$ plane, i.e. $\sqrt{u^2 + w^2}$. The probe in the HWA_{ver} case was aligned perpendicular to the inflow direction to measure the velocity components contained in the $y - z$ plane, i.e. $\sqrt{v^2 + w^2}$. The transverse region extends from 30% to 95% of the chord and vertically from $z = 1$ mm to a maximum of 20 mm. In Chapter 5, the extension of the assessed region reduces axially from 40% to 80% of the chord, increasing

the number of data points along the z-axis. In Chapter 4, the suction side region of the aerofoil was investigated using HWA in several chord-wise sections, with the probe aligned parallel to the x-axis, as shown in figure 2.5. Additional details on PIV data processing and the uncertainty analysis for both velocity measurement techniques are provided in Appendix A.3.

2.2.3 Forces

A load cell was mounted to the aerofoil to measure the aerodynamic forces acting on the aerofoil. Specifically, a F/T Sensor Mini40 is mounted to the aerofoil between two steel brackets. The position of the upper bracket is set by four adjustable bolts, which regulate the gap size. The lower bracket is attached to the aerofoil but can move freely. This setup ensures that as the aerofoil moves under aerodynamic forces, the lower bracket transfers these forces to the load cell for measurement.

The forces of interest are specifically lift L and drag D, which are non-dimensionalised as follows:

$$C_L = \frac{L}{0.5\rho_\infty U_0^2 S} \tag{2.5}$$

$$C_D = \frac{D}{0.5\rho_\infty U_0^2 S} \tag{2.6}$$

where S is the relevant surface area, calculated as the product of the aerofoil chord and the span length, which varies with the gap size. Additional details are reported in Appendix A.5.

2.2.4 Pressure-velocity correlations

HWA and PIV velocity measurements were performed simultaneously with pressure measurements to calculate the covariance between velocity and pressure signals. This approach, similar to that proposed by Henning et al. (2008) to process PIV data, enables the identification of flow structures involved in the noise generation. The covariance between the velocity and the pressure signals is evaluated by using the following formula:

$$\mathrm{Cov}_{(u,p)}(\mathbf{x},\mathbf{y}) = \frac{1}{N-1}\sum_{n=1}^{N}[u'(\mathbf{x},t_n)p'(\mathbf{y},t_n+\tau)] \tag{2.7}$$

where u' are the velocity fluctuations measured in the near-field at position $\mathbf{x}$ and at discrete times t_n, while p' are the pressure fluctuations measured by the far-field microphone at position $\mathbf{y}$. The term τ represents the time it takes for sound to propagate from the aerofoil to the far-field microphone, and N is the total number of PIV snapshots.

The far-field microphone acquires at discrete times for 0.2 seconds, simultaneously to PIV snapshots, with the first laser pulse of the PIV system triggering the acquisition of the pressure measurements. Clearly, the PIV system operates at a much lower sampling rate compared to the pressure signals. However, the covariance is calculated by correlating $u'(t_n)$ with $p'(t_n + \tau)$ and by averaging over 1600 PIV snapshots. A high number of snapshots is necessary to reduce the contributions of uncorrelated noise and random errors.

The same expression is used to evaluate the covariance between pressure and the velocity fluctuations measured with HWA. However, the covariance is individually assessed in each location occupied by the hot-wire probe. Consequently, N represents the total number of samples of both pressure and velocity signals in each position. Both far-field microphone and hot-wire probe acquire for 6.28 seconds at the same sampling frequency of 50 kHz. Note that the single hot-wire probe cannot quantify one specific component of the velocity, but rather the resultant velocity contained in a plane, depending on the probe orientation. Referring to the formulation used in table 2.1, $\mathrm{Cov}_{\mathrm{ver}}$ is evaluated considering the fluctuations of the resultant velocity measured in the $y-z$ plane, whereas $\mathrm{Cov}_{\mathrm{hor}}$ refers to the measurements in the $x-z$ plane. These covariance values can be compared with those obtained using Stereo PIV technique, as this technique allows the evaluation of the three velocity components.

Chapter 3

Tip leakage noise source mechanisms

This chapter investigates the physical mechanisms involved in the generation of the tip leakage noise for a stationary aerofoil. Through experiments, two dipole-type noise sources are identified and attributed to fluid-dynamic instabilities occurring within the gap, vortex-shedding and shear layer roll-up, which are linked to the behaviour of the tip leakage flow. The chapter first characterises these noise-generating mechanisms for the baseline configuration and then explores their variation across other configurations.

3.1 Background

Fan broadband noise represents one of the dominant noise sources in modern turbofan engines, particularly during take-off and approach conditions (Moreau and Roger, 2018). Among the various sources involved in the generation of fan broadband noise, the tip leakage noise is the least understood mechanism. This noise results from the interaction between the tip leakage flow, the casing boundary layer and the blade tip (Ganz et al., 1998). The tip leakage flow is a three-dimensional unsteady flow that occurs in the gap between the blade tip and the duct wall. It is generated by the pressure difference between the suction side and the pressure side of the blade, as well as by the relative motion between the blade tip and the casing wall.

3.1.1 Tip leakage flow in a cascade

Over the years, tip leakage flow has been studied extensively from the aerodynamic viewpoint due to its impact on efficiency loss. Focusing on a linear turbine cascade,

Bindon (1989) suggested that the major part of the tip gap loss arises when the "slow-moving separation bubble flow" leaves the gap at the aerofoil suction side. The separation bubble, within the tip gap, was formulated for the first time by Rains (1954), who studied the flow through the tip gap of a compressor blade. He proposed a 2-D idealised model where the tip flow enters the clearance, separates at the pressure side tip edge and contracts into a high-speed jet near the bottom wall. He also defined the ratio between the downstream jet width and the gap size e as the contraction ratio $\sigma = 0.611$.

Storer and Cumpsty (1991) measured the flow at the exit of the gap in different chordwise locations, for a configuration characterised by a gap size equal to 4% of the chord. They noticed that the high-speed jet appeared downstream of the mid-chord, where the pressure on the suction side reached minimum value. Upstream of the mid-chord, a fully developed profile, with slightly reduced speed, was found. Graham (1986) measured the velocity profiles in one position close to the aerofoil suction side, for two gap sizes, $e/c = 1.65\%$ and 3.45%. The jet flow near the bottom wall was detected in the configuration with a greater gap size, whereas the fully developed profile was found for the smaller gap size case. Subsequently, Denton (1993) linked these two tip flow behaviours to the ratio between the local aerofoil thickness τ and the gap size e. Specifically, he suggested that for $\tau/e < 4$, the separated flow is unlikely to reattach to the blade, while for $\tau/e > 4$ the separation bubble remains localised and the jet mixes out before leaving the gap.

As hypothesised by Storer and Cumpsty (1991), the pressure distribution along the aerofoil suction side is influenced by the position and the strength of the so-called tip leakage vortex. This vortex was revealed through flow visualisations with oil and wool tufts. Its trajectory coincided with a trough of pressure which moved progressively downstream of the leading edge as the tip clearance was increased from $e/c = 2\%$ to 4%. No vortex signature on the aerofoil suction side was found by Graham (1986) for the configuration characterised by the smallest ratio $e/c = 0.82\%$. One of the first schematics of the tip flow topology was developed by Kang and Hirsch (1993), based on ink-trace flow visualisations on a linear compressor cascade of seven blades with $e/c = 2\%$. The flow topology representation consists of the TLV and a Tip Separation Vortex (TSV), as well as a secondary vortex that rotates in the opposite direction to the TLV, whose generation was unclear. The TLV developed downstream of the aerofoil leading edge and grows in size along the chord. The TSV "was rolled up by the flow separated from the pressure side edge", which is similar to the separation bubble referred to Rains (1954). In this chapter, the influence of the TLV on the tip flow behaviour, which is associated with the noise-generating mechanisms, will be suggested.

The evolution of the tip leakage vortical structures was investigated by You et al. (2007), using Large-Eddy Simulations (LES) on a linear cascade with a moving casing wall, which corresponds to the experimental set-up of Wang and Devenport (2004) with

$e/c = 1.65\%$. The TSV becomes significant in the suction side region of the aerofoil downstream of the mid-chord, while the TLV dominates the flow field from the $15 - 20\%$ of the axial chord. In the core of the TLV, a peak in the energy spectra of the cross-stream velocity component was observed at the chord-based Strouhal number $St_c = fc/U_0 = 1.5$, where f is the frequency, c is the chord length and U_0 is the inflow velocity. This spectral peak is not found in the experiments carried out by Muthanna and Devenport (2004) on the same set-up with a stationary wall. This low-frequency peak was linked to a wandering motion of the TLV and not to a periodic vortex shedding found in the blade wake at $St_c = 5 - 6$. Boudet et al. (2015) found that the non-dimensional frequency associated with such "vortex wandering" phenomenon, i.e. $St_c = 1$, dominated the sound spectrum. They used experimental and numerical methods to study the tip flow in a rotating fan rig with $e/c = 5.5\%$.

3.1.2 Tip leakage noise of a stationary aerofoil

The oscillation of the TLV was suggested by Jacob et al. (2016a) to be responsible for a broad peak in the velocity spectra detected around $St_c = 0.08 - 0.28$ in the vortex core downstream of the aerofoil trailing edge. However, no trace of this oscillation was found in the far-field spectrum. The set-up was characterised by a single-stationary-cambered aerofoil with a gap size of $e/c = 5\%$ positioned within an anechoic wind tunnel. This set-up, which is similar to the one used in the current investigation, was developed by Grilliat et al. (2007) to identify tip leakage noise, as it is quite problematic to distinguish it in a representative fan rig (Ganz et al., 1998). Their investigation highlighted a low-frequency hump, at $St_c = 4$, in the far-field and wall pressure spectra. This noise source was likely attributed to a flow separation occurring at the pressure side edge. Its scaling with the fifth power of the inflow velocity U_0 suggested the possible role of trailing edge scattering in the noise-generating mechanism. Analysing the near-field spectra downstream of the aerofoil mid chord, they hypothesised a flow separation at the gap entrance for large tip gap $e/c = 5\%$, while for small gaps, $e/c = 1.5 - 2.5\%$, the flow "would still reattach before leaving the clearance". Another high-frequency noise source was detected at about $St_c = 10$ and was identified as a "jet-like" source, due to its velocity dependence U_0^7 - U_0^8. According to Jacob et al. (2010), this second source was associated with "secondary turbulent eddies generated by the flow separation at the gap suction side tip edge".

A wavelet-based conditional averaging technique was applied by Camussi et al. (2010) to correlate the pressure and velocity data collected during the experimental campaign of Grilliat et al. (2007). This conditional analysis localised the low-frequency hump of $St_c = 4$ between $40 - 60\%$ of the chord, linking it with "swirling turbulent structures generated by the pressure side tip edge". However, the sound-generating mechanism

of the other noise source remained unclear. The same set-up was used in the LES simulations by Koch et al. (2021). A good agreement with the experimental results of Jacob et al. (2010) was obtained, especially regarding flow topology and pressure fluctuations. Regarding the noise spectra, Koch et al. (2021) hypothesised that the noise source found in the frequency range $St_c = 8$ - 20 results from the interaction between the turbulent structures generated around the mid-chord and the aerofoil suction side tip.

The tip flow around a symmetrical aerofoil was simulated by Decaix et al. (2015) for a range of tip gap sizes to understand the influence of this parameter on the development of the trajectory of the TLV. For the small gap case $e/c = 2\%$, the TSV barely develops underneath the blade, so it could be interpreted more as a shear layer than a vortex. The TSV is clearly identified in the large gap case $e/c = 10\%$. Specifically, downstream of the mid-chord, the TSV wraps the TLV merging into a single vortex near the trailing edge. This is where the pressure fluctuations are likely to be scattered in noise, according to Higgens et al. (2019). Indeed, they observed two vortices generated on both aerofoil sides coalescing at the trailing edge until a critical size $e/c = 7.5\%$. For smaller gap heights, these vortical structures "are pushed" towards the suction side region further upstream, without encountering any solid edge where they can scatter.

3.1.3 Novel contributions of the current chapter

The literature review has highlighted a limited understanding of the physical mechanisms involved in the generation of tip leakage noise of a stationary aerofoil. Previous studies (Grilliat et al., 2007; Jacob et al., 2010) identified two noise sources in the pressure measurements. In this work, we build on these investigations by specifically identifying the fluid-dynamic instabilities responsible for these noise sources. These sources are attributed to the roll-up and the shedding of vortical structures generated by the separation of the tip leakage flow at the pressure side edge. After the separation at the pressure side edge, the tip flow can either reattach to the aerofoil or remain separated until the exit of the gap. Roll-up occurs in both scenarios, whereas shedding occurs only when there is an extended separation. The frequency of the noise source due to the vortex-shedding is found to depend on the position along the chord of the extended separation, while the roll-up noise source is characterised by multiple spectral peaks that are consistent across different configurations. The corresponding non-dimensional frequencies of both noise sources, together with the characteristic length scales, are identified using the similarity between the tip leakage flow and the flow over a Backward-Facing Step (BFS).

This chapter is organized as follows: first, the tip noise sources are characterized for the baseline configuration with $\alpha = 15°$ and $e = 10$ mm, followed by an exploration of these sources across other configurations.

3.2 Baseline configuration

3.2.1 Acoustic measurements

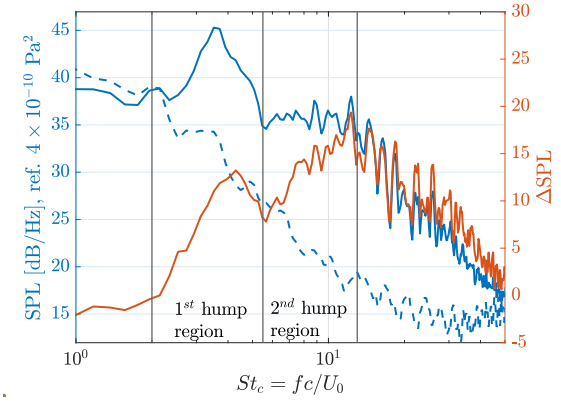

Figure 3.1: Sound pressure level (SPL) spectra detected for baseline case (—) and no gap case (– –), together with the tip leakage noise obtained for the baseline case (—).

The far-field sound pressure level measured for the baseline configuration, with $\alpha = 15°$ and $e = 10$ mm, is plotted in figure 3.1, together with the spectrum obtained without the gap. The abscissa represents the non-dimensional frequency $St_c = fc/U_0$, based on chord length c and inflow velocity U_0. The levels of the first spectral curve are significantly higher when compared to the spectra of the no-gap case, with a maximum increase of approximately 19 dB. The two noise spectra are subtracted to isolate the contribution of the tip leakage noise on the far-field, resulting in the orange curve shown in figure 3.1. The tip leakage noise is then determined by subtracting directly in dB scale, as follows:

$$\Delta SPL = 10\log_{10}(S_{pp,baseline}) - 10\log_{10}(S_{pp,nogap}) \tag{3.1}$$

where S_{pp} is the power spectral density of the far-field acoustic pressure. In this way, the contributions of the leading and trailing edge noise and background noise are partially removed since these contributions are similar with and without the gap.

Two distinct regions of the noise spectra can be identified in this figure: one ranging approximately from 0.5 to 1.1 kHz, which corresponds to a chord-based Strouhal number St_c between 2 and 5.5, and the other between 1.1 kHz and 2.6 kHz, i.e. $St_c = 5.5$ - 13. These areas are labelled, respectively, as first hump and second hump region. The first region presents a clear peak around $St_c = 4$, also observed by Grilliat et al. (2007). The second region displays multiple peaks. However, at $St_c = 10$, an increase in the noise spectra of about 16 dB is reached, surpassing the 6 dB increase reported by Jacob et al. (2016a) at the same Strouhal number. This discrepancy may be due to a lower background and trailing edge noise, caused by a reduced inflow turbulence and a smaller aerofoil span.

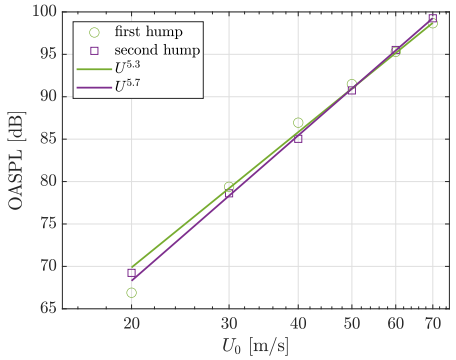

Figure 3.2: Overall sound pressure levels (OASPL) against the inflow velocity U_0 evaluated in the first hump and second hump frequency range.

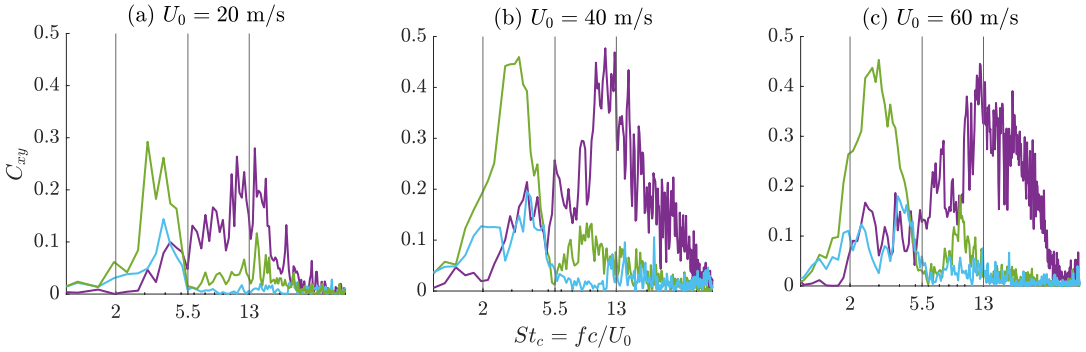

Figure 3.3: Coherence between far and near field signals, acquired using the far-field microphone and the remote probes located at $x/c = 0.50$ (—), 0.75 (—) and $x/c = 0.90$ (—) on the pressure side of the aerofoil, for $U_0 = 20$ (a), 40 (b) and 60 m/s (c).

The possible noise generating-mechanisms linked to the two spectral humps are found to scale approximately between the fifth and sixth power of the inflow velocity, i.e. $U_0^{5.3}$ for the first hump and $U_0^{5.7}$ for the second one. Both trends are shown in figure 3.2, where each value is obtained by integrating the far-field spectra in the first and second hump frequency ranges for different inflow velocities. The observed velocity scaling suggests a mixed source mechanism, rather than a pure dipole. According to the literature (Howe, 2002), dipole and quadrupole sources close to a shape edge scale with U^5, while in the absence of a sharp edge, they would radiate with U^6 and U^8, respectively. A dipole-like directivity pattern was observed in the LES study by Koch et al. (2021).

The coherence between the near and far-field pressure signals are shown in figure 3.3, for three different inflow velocities. A key finding emerges from this figure. The tip leakage noise appears to be a Strouhal-dependent phenomenon, as a similar trend is observed across different velocities. Furthermore, the high coherence values of about 0.5, seen in figure (b) and (c), indicate that the first hump can be localised between the 50% and 90% of the chord, while the second hump is mainly located around the midchord. This qualitative localisation of the two noise sources is confirmed in the following sections by correlating velocity and pressure signals.

3.2.2 Pressure-velocity correlations

3.2.2.1 First spectral hump

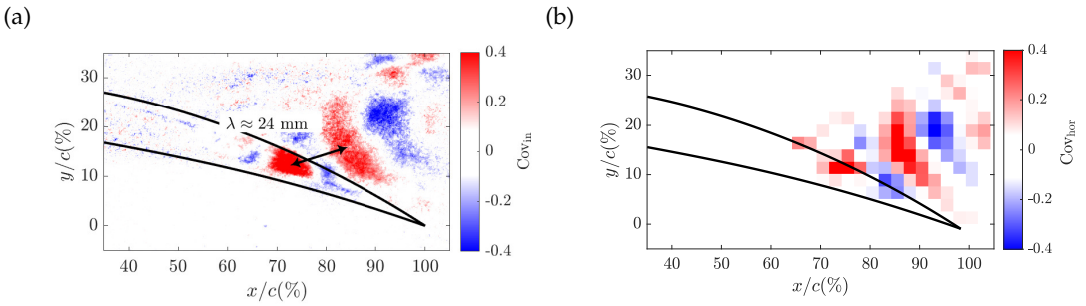

Figure 3.4: Covariance plots obtained by relating the velocity fluctuations, measured in the $x-z$ plane with PIV_{in} (a) and HWA_{hor} (b), with the pressure signals filtered in the first hump frequency range, $St_c = 2-5.5$, for $U_0 = 40$ m/s.

The flow features contributing to the two spectral humps are identified using the procedure described in section 2.2.4. Figure 3.4 (a) and (b) show the covariance plots obtained by correlating the velocity fluctuations measured using PIV and HWA techniques, with the far-field pressure signals, which have been band-pass filtered in the frequency range of the first hump, i.e. $St_c = 2-5.5$. A large-scale coherent pattern, starting around the 60% of the chord, is observed in both figures, with nearly identical covariance values, despite the lower spatial resolution in figure 3.4 (b). This result supports the hypothesis that these coherent structures are responsible for the first spectral hump.

The first-hump pattern is characterised by a hydrodynamic wavelength that needs to satisfy the relationship $\lambda = U_c/f$, where f is the frequency and U_c is the convection velocity (Glegg and Devenport, 2017). This velocity can be evaluated from the gradient of the phase spectra between two remote mics, as reported in formula 2.3. Figure 3.5 shows the phase spectra between two microphones located on the aerofoil pressure side at the 75% and 90% of the chord, for two different inflow velocities $U_0 = 40$ and 60

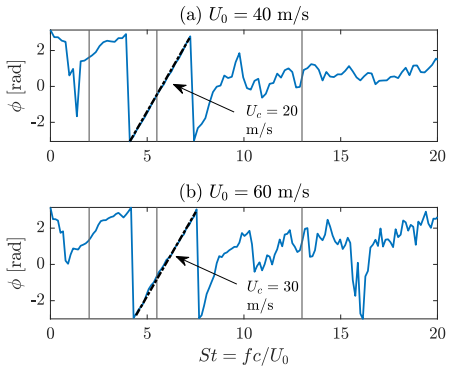

Figure 3.5: Convection velocities estimated from the phase spectra for $U_0 = 40$ (a) and 60 m/s (b).

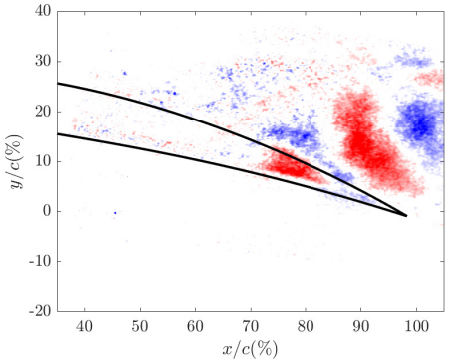

Figure 3.6: Covariance plots obtained by relating the velocity fluctuations, measured in the $x-z$ plane with PIV_{in}, with the pressure signals filtered in the first hump frequency range, $St_c = 2-5.5$, for $U_0 = 60$ m/s.

m/s. Within the frequency range of the two humps, i.e. $St_c = 2-13.$, the convection velocity is estimated to be 0.5 of the inflow velocity. By combining this velocity with the 24 mm wavelength, estimated from 3.4 (a) between the 75% and 90% of the chord, where the two remote mics used to estimate U_c are located, a frequency of 0.8 kHz is obtained, which falls within the range of the first hump. Although the convection velocity agrees with Grilliat et al. (2007), which reported a velocity value oscillating between 0.4 and 0.65 of the inflow velocity in a similar frequency range, it is slightly lower compared to $0.6-0.8$ of U_0 reported in literature (Glegg and Devenport, 2017). This underestimation can be attributed to the remote probes not aligning with the direction of the convected structures. However, the current approach represents a reasonable estimate of the actual convection velocity given the low angle between the direction of convected structures and probe orientation.

The case with $U_0 = 60$ m/s, shown in figure 3.6, exhibits the same covariance pattern as that found for $U_0 = 40$ m/s. Consequently, assuming the same wavelength ($\lambda = 24$ mm) and an increased convection velocity ($U_c = 30$ m/s), a frequency of $f = 1.2$ kHz is obtained, corresponding to $St_c \approx 4$, which still falls within the range of the first hump. This further supports the hypothesis of the Strouhal-dependent nature of the tip noise.

The Proper Orthogonal Decomposition (POD) was applied to the flow field as an alternative method to extract coherent structures (Taira et al., 2017). Figure 3.7 (a) shows the first spatial mode, which is similar to the second mode in (b), with a shift of approximately one-third of the wavelength λ. Because of this translation, this pair of POD modes represents a periodic phenomenon, as suggested by Weiss (2019). Although these two modes account for about 5% of the total kinetic energy, shown in figure (d), these modes align with the covariance plot displayed in (c). This similarity implies that these spatial modes, which are not directly linked to the surface pressure fluctuations but relate only to the flow field, are responsible for the first spectral hump. These spatial modes show the presence of structures resembling vortices in the flow, as the von Karman street of vortices that occur in the wake of a circular cylinder (Henning et al.,

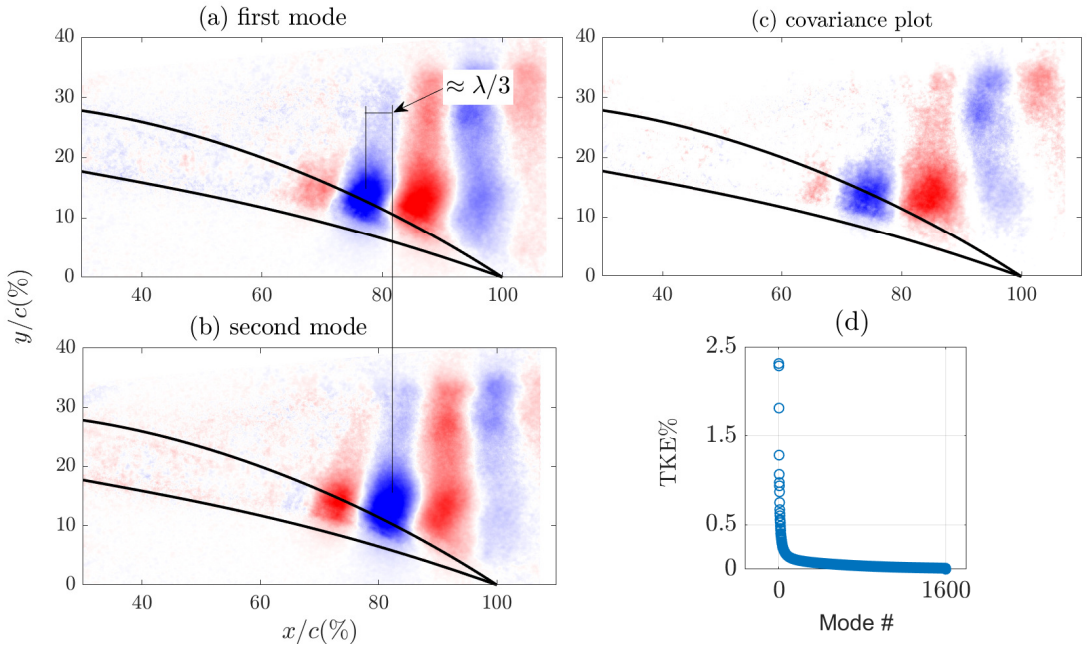

Figure 3.7: First (a) and second (b) spatial mode, and covariance plot (c) obtained by considering the velocity fluctuations in the y-direction, measured with PIV_{in}. The covariance plot is obtained by relating the velocity fluctuations with the pressure signals filtered in the first hump frequency range, $St_c = 2 - 5.5$. (d) Total Kinetic Energy from each mode.

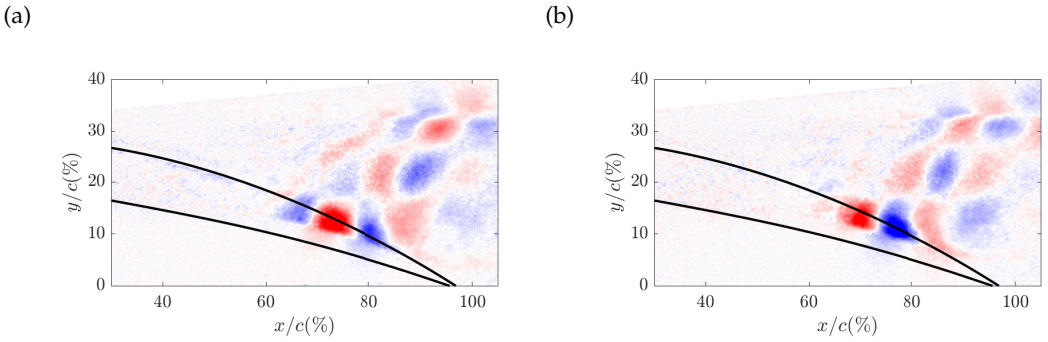

Figure 3.8: Fifth (a) and sixth (b) spatial mode obtained by considering the velocity fluctuations in the x-direction, measured with PIV_{in}.

2008; Weiss, 2019). Therefore, we can hypothesise that the first tip noise source is due to a period phenomenon, i.e. a vortex shedding-type mechanism. Note that figures 3.7 (a), (b) and (d) are obtained by considering the velocity fluctuations in the y-direction. This explains the discrepancy with the covariance plot in figure 3.4 (a) obtained by considering the resultant velocity in the $x - z$ plane, for which the first-hump pattern only appears in higher spatial modes, specifically the fifth and the sixth mode as shown in figure 3.8. The reasons for this higher-mode appearance become clear when analyzing the instantaneous flow fields in section 3.2.3.

3.2.2.2 Second spectral hump

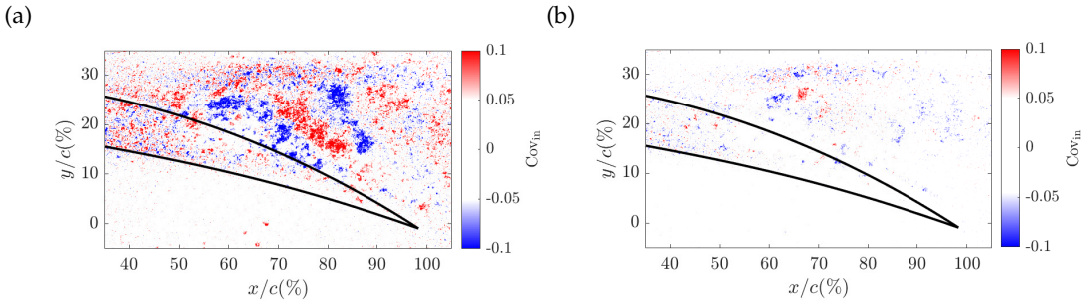

Figure 3.9: Covariance plots obtained by relating the velocity fluctuations, measured in the $x-z$ plane using $\mathrm{PIV_{in}}$, with the pressure signals filtered in two frequency ranges: (a) $St_c = 5.5-13$ and (b) $St_c = 13-50$.

Figure 3.9 (a) displays the covariance plot obtained by relating the velocity fluctuations measured using PIV with the pressure signals, which have been band-pass filtered in the frequency range of the second spectral hump, i.e. $St_c = 5.5-13$. This reveals a pattern of coherent structures with much smaller scales. As expected, these smaller scales correspond to shorter wavelengths and, thus, higher frequencies, which fall within the second hump frequency range. The upper limit of the second hump frequency range was determined based on the observation that no coherence patterns were found when the pressure signals were band-pass filtered beyond this range, i.e. $St_c = 13-50$, as shown in figure 3.9 (b).

To gain insight into the three-dimensional characteristics of the second-hump pattern, it is beneficial to consider the plot of figure 3.10, which depicts the covariance obtained in the span-wise direction, using the hot-wire probe at gap exit along the aerofoil suction side. The second hump is related to vortical structures that develop within the tip gap area. These structures are initially localised around the mid-chord, which is consistent with the coherence plots shown in figure 3.3. Then, they are spread out across the aerofoil suction side region, as observed in figure 3.9 (a).

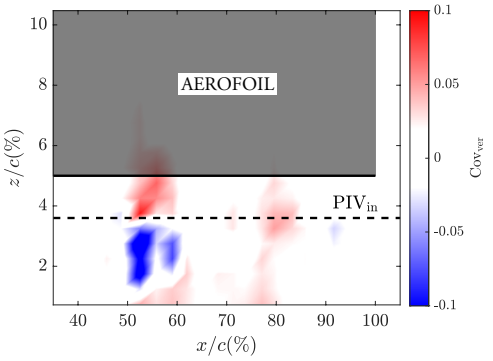

Figure 3.10: Covariance plots obtained by relating the velocity fluctuations in the $y-z$ plane using $\mathrm{HWA_{ver}}$, with the pressure signals filtered in the second hump frequency range, $St_c = 5.5-13$. The grey area represents the aerofoil.

The second-hump pattern resembles the roll-up mechanism of a shear layer. This flow instability has been visualised within the gap in different cross-sections in Chapter 6 through the application of Spectral POD (Schmidt and Colonius, 2020) and Dynamic Mode Decomposition (Schmid, 2010) on LES data (Koch et al., 2021). Both decompositions extract coherent structures at specific frequencies. The numerical simulations address the limitations of using experimental measurement techniques in the small gap region. Due to these limitations, in the current chapter, the tip flow was quantified in the span-wise direction only at the gap exit using HWA, and the connection between the two fluid-dynamic instabilities responsible for the two spectral humps is supported by the similarity with the flow over a backward-facing step, as detailed in section 3.3.

3.2.3 Tip flow topology

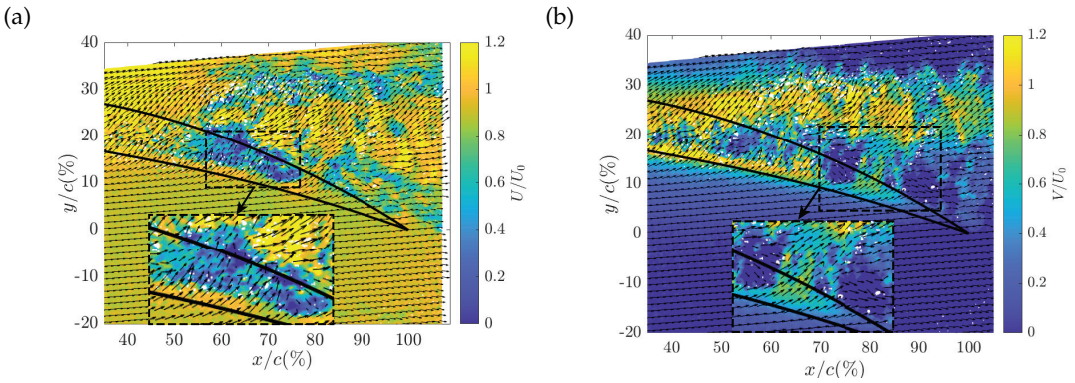

Figure 3.11: Instantaneous velocity fields of the stream-wise (a) and cross-stream velocity component (b) with velocity vectors measured with $\mathrm{PIV_{in}}$.

The presence of a separated flow is a necessary condition for the formation of a vortex-shedding type phenomenon. In the case of tip gap flow, a separated flow can be observed in the instantaneous flow field. Two random PIV snapshots with velocity vectors superimposed on the distribution of the stream-wise and cross-wise velocity components are shown in figure 3.11 (a) and (b), respectively. The separated flow is discernible between 50 and 75% of the chord, where the velocity vectors appear random, compared with those upstream of the mid-chord or in the region close to the pressure side. This separated zone is easily identified by the low-velocity blue region in the stream-wise velocity field, as shown in the zoomed-in portion of figure 3.11 (a). Downstream of 75% of the chord along the aerofoil suction side, the velocity vectors exhibit strong fluctuations, identified by the alternating blue and green spots shown in the zoomed-in part of figure (b). These zones of highly correlated flow correspond to the first-hump pattern found when applying POD analysis to the cross-wise component of the velocity seen in figure 3.7 (a) and (b). These fluctuations disappear completely in the mean fields and are not readily observed in the U/U_0 velocity contour in figure 3.11 (a). This observation may explain why the same pattern only appears in higher spatial modes when applying POD to the streamwise velocity component.

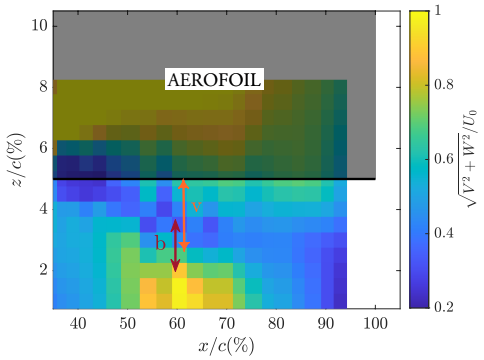

Figure 3.12: Mean velocity field of the resultant velocity in the $y-z$ plane measured along the aerofoil suction side with HWA_{ver}.

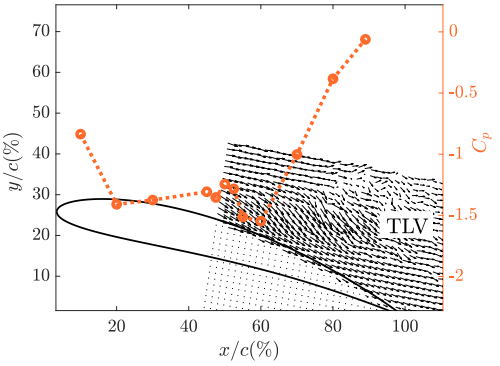

Figure 3.13: Pressure distribution C_p over the aerofoil suction side (-o-) superimposed on the instantaneous velocity vectors field obtained with PIV_{out}

The velocity contour obtained with HWA at the gap exit along the aerofoil suction side, shown in figure 3.12, provides insight into the extension of the separated flow in the span-wise direction and the flow topology within the tip area. The most interesting features are observed between 50% and 75% of the chord. Below the aerofoil tip edge, the separated flow region can be identified by a low-velocity region, whose width is defined by the length v. This separation reduces the passage area, causing the flow close to the bottom wall to contract into a high-speed jet, as modelled by Rains (1954). The gradient of the velocity allows the thickness b of this shear layer to be quantified. The relationship between these two length scales, b and v, and the two fluid dynamic instabilities responsible for the two noise sources, roll-up and vortex shedding, is discussed in the following section 3.3.

The separated flow and the corresponding high-speed jet were also observed at the exit of the gap downstream of the mid-chord by Storer and Cumpsty (1991). Upstream of the mid-chord, they detected a fully developed velocity profile, which can be also identified in figure 3.12 around the mid-chord, where the jet flow near the wall is weaker. Hence, two scenarios can be defined. The first occurs when the tip flow, after separating at the pressure side edge, reattaches to the aerofoil tip. The second scenario occurs

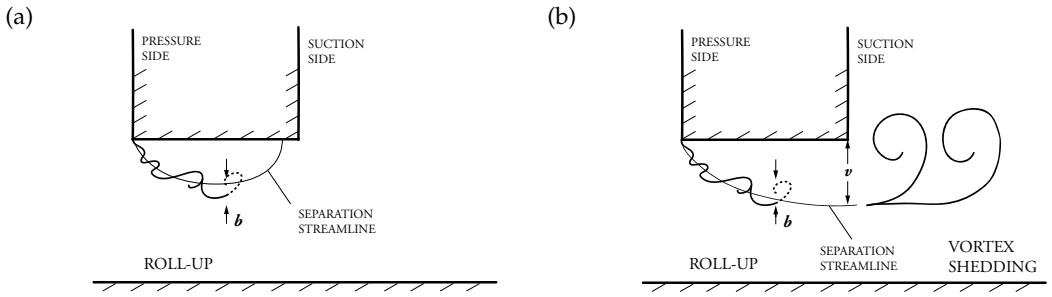

Figure 3.14: Schematic representations of the tip leakage flow: the flow separates and reattaches at the aerofoil tip (a), the flow remains separated at the exit of the gap (b). These sketches are based on the models developed by Denton (1993) and Driver et al. (1986): b is the shear layer thickness, v the separated flow width.

when the flow remains separated until the exit of the gap. The transition from a localised separation to an extended separated flow could be due to the interaction (or lack thereof) between the tip leakage vortex and the flow within the gap. This can be further explored by examining the pressure distribution over the aerofoil suction side and the flow field above the tip. Figure 3.13 shows the pressure distribution C_p which exhibits low values from the aerofoil leading edge till about the mid-chord. Over the same distance, we expect the TLV to be close to the airfoil surface thereby keeping the pressure low (Storer and Cumpsty, 1991). Beyond the mid-chord, the pressure distribution displays a sharp drop in magnitude and this coincides with the TLV moving farther away from the airfoil surface. This movement of the TLV, together with the appearance of extended separated flow within the gap downstream of the mid-chord seen in figure 3.11, suggests that these two phenomena might be linked.

We hypothesise, therefore, that the separated flow tends to reattach upstream of the mid-chord due to the low pressure produced by the TLV. When the TLV moves far enough from the aerofoil surface downstream of the mid-chord, it no longer influences the separated flow, which remains separated at the exit of the gap. These tip flow behaviours are illustrated with two simplified cross-sectional sketches shown in figures 3.14 (a) and (b). In both cases, a shear layer of thickness b develops but only the second case exhibits an extended separated flow of width v at the exit of the gap.

3.3 Similarity with the Backward-Facing Step flow

The tip leakage flow is similar to the flow over a backward-facing step. This flow is characterized by a separation at the step edge and subsequent formation of a thin shear layer. This grows in size due to the growth of span-wise vortices, linked to Kelvin-Helmholtz instabilities, which roll-up into discrete structures of a size equivalent to the thickness of the shear layer b (Scarano et al., 1999; Kostas et al., 2002). Driver et al. (1986) observed that the majority of the energy in a BFS flow is concentrated at the frequency

characteristic of the roll-up of these structures, corresponding to a non-dimensional frequency of $St_b = fb/U_{SL} = 0.2$ where U_{SL} is the shear layer velocity, defined as the average of high and low-speed sides of the shear layer. The same result was also found for free shear layers by Winant and Browand (1974). In section 3.2.2, the second-hump pattern was related to the roll-up mechanisms of a shear layer. Referring to figure 3.12, the shear layer thickness can be estimated to be $b \approx 3$ mm and the shear layer velocity to be $U_{SL} = 21$ m/s, at around $x/c = 60\%$ where the identification of these parameters is easier. Combining these values with the frequency range of the second noise source, $f = 1.1 - 2.6$ kHz, yields a range of non-dimensional frequencies $St_b = 0.16 - 0.37$ that covers $St_b = 0.2$. Hence, this supports the link between the second hump and the roll-up of the shear layer within the gap. Notably, as the tip flow separates along the pressure side edge, roll-up develops along the chord contributing to the broadband second hump, as seen in figure 3.9 (a). This also means that both b and U_{SL} vary in the stream-wise direction and within the tip gap.

The similitary between tip leakage and BFS flow can also be used to confirm the connection between the first hump and a vortex shedding-type phenomenon. According to Hudy et al. (2007), the roll-up of vortical structures in a BFS flow leads to the formation of large-scale structures that are shed once they reach a maximum size equivalent to the height of the step. The non-dimensional frequency of this shedding phenomenon was measured to be $St_h = fh/U_0 = 0.07$, where h is the height of the step. This was also confirmed in other works (Wee et al., 2004; Liu et al., 2005). The step edge represents the maximum size of the separated flow in the span-wise direction. The corresponding length scale in the tip leakage flow is v, which reaches maximum values at the gap exit, as seen in Decaix et al. (2015). A value of $v \approx 4$ mm can be evaluated at $x/c = 60\%$ in figure 3.12, confirmed in Chapter 6 with the numerical simulations. This results in a $St_v = fv/U_0 \approx 0.07$, based on the frequency of the first spectral hump of $f = 0.8$ kHz. Evaluating the contraction ratio σ using the length v, we obtain a value $\sigma = (e - v)/e \approx 0.6$ which is consistent with the value formulated by Rains (1954). From the numerical study of Ma et al. (2023) on a Forward-Backward facing Step, it has been possible to evaluate both shedding frequency and length v at the downstream step edge. In this case, both quantities also lead to a $St_v \approx 0.07$.

The two tip noise sources detected in the pressure spectra can be linked to the flow separation that occurs along the pressure side edge. The roll-up of the vortical structures within the shear layer generates fluctuations in the frequency range of the second noise source, centered around the non-dimensional Strouhal number $St_b = fb/U_{SL} = 0.2$. Once these vortical structures reach maximum size, vortices are shed at the non-dimensional frequency $St_v = fv/U_0 = 0.07$, where f corresponds to the frequency of the first noise source. This occurs when the tip flow does not reattach to the aerofoil, while the second noise source also develops when the flow reattaches to the aerofoil, as will be seen in section 3.4.2. The power laws, plotted in figure 3.2, suggest that the two

noise sources may be generated by the scattering at the aerofoil tip edge of the pressure fluctuations caused by these two fluid dynamic instabilities, roll-up and vortex shedding.

While it is not feasible to obtain exact values for both characteristic lengths b and v due to the limitations of hot wire measurements when immersed in a separated flow, we are still able to provide a rough estimation of these lengths. Despite this uncertainty in v and b, the Strouhal numbers obtained by combining these lengths with the frequencies of the two noise humps are consistent with those documented in the literature for the aforementioned fluid-dynamic instabilities.

3.4 Influence of α and e on the tip noise sources

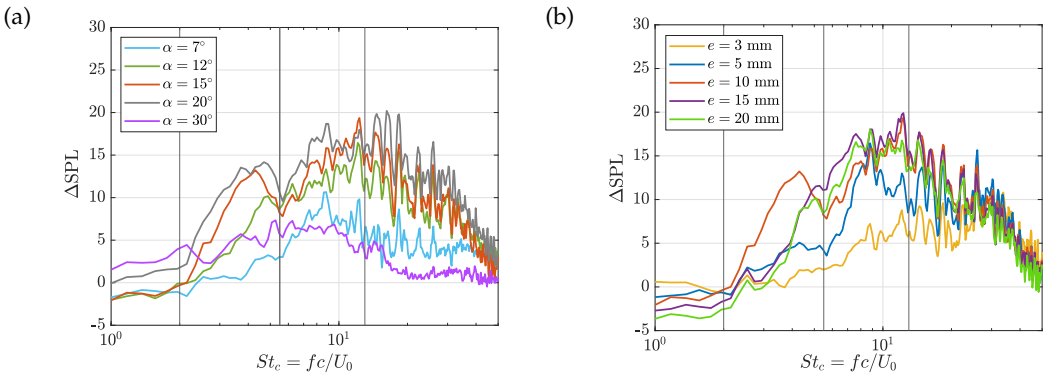

Figure 3.15: Tip leakage noise for different configurations obtained by varying the angle of attack α while keeping the gap size $e = 10$ mm (a), and by changing e for a constant $\alpha = 15°$ (b).

The presence of the extended separated flow has been linked to the formation of a vortex-type shedding phenomenon, which has subsequently been identified as the source of the first spectral hump. Therefore, to investigate the properties of the first hump, the angle of attack is changed to modify the characteristics of this separated flow. Figure 3.15 (a) displays the changes of the tip leakage noise as the angle of attack varies from 7° to 30°, while the gap size is kept constant to $e = 10$ mm. As expected, the first hump changes: it becomes broader for $\alpha = 20°$, compared to the baseline case. It shifts to higher frequencies and becomes narrower for $\alpha = 12°$, whereas it is absent at $\alpha = 7°$. Overall, the tip noise increases as the angle attack grows to $\alpha = 20°$. Beyond this point, a nearly "flat" spectrum is observed for $\alpha = 30°$.

The second hump has earlier been associated with the roll-up mechanism of the shear layer that develops within the tip gap. Considering the simplified sketches in figure 3.14 (a) and (b), it is logical to think that the extent of the shear layer depends on the size of the gap. Therefore, to further investigate the characteristics of the second hump, the effect of varying the gap size is investigated. Figure 3.15 (b) displays the changes

in the tip noise spectra as the gap size e increases from 3 to 20 mm. The angle of attack is fixed at $\alpha = 15°$. The second hump increases as the gap size enlarges from $e = 3$ mm to $e = 10$ mm. Beyond that, the noise ceases to increase. This behaviour suggests that the shear layer develops ($e = 3$ mm) and grows ($e = 5$ and 10 mm) as the gap size increases, until further increases in the gap size no longer cause significant changes in the shear layer ($e = 15$ and 20 mm).

Note that the gap size also influences the first hump. Figure 3.15 (b) shows this peak moving to higher frequencies for $e = 15$ and 20 mm and disappearing for $e = 3$ and 5 mm. Within the frequency range of the second hump, the spectra in figure 3.15 (a) maintain a similar shape, with levels increasing up to $\alpha = 20°$. This trend may be attributed to the stronger shear layer generated by the higher pressure difference between the two sides of the aerofoil at higher angles of attack. Chapter 4 focuses on the non-dimensional parameters that influence the strength of both tip noise sources.

3.4.1 Further considerations about the first hump

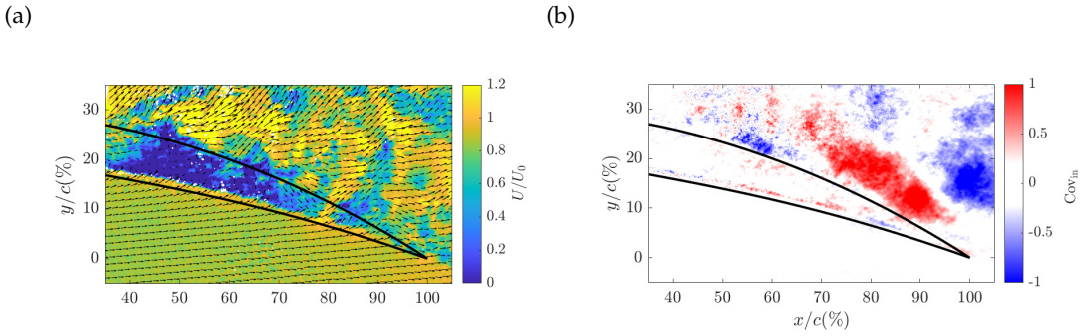

Figure 3.16: Configuration $\alpha = 20°$ and $e = 10$ mm. (a) Instantaneous velocity field of the stream-wise velocity component with velocity vectors measured with $\mathrm{PIV}_{\mathrm{in}}$. (b) Covariance plot obtained by relating the velocity fluctuations, measured in the $x - z$ plane using $\mathrm{PIV}_{\mathrm{in}}$, with the pressure signals filtered in the first hump frequency range, $St_c = 2 - 5.5$.

A detailed analysis has been conducted on the configurations with $\alpha = 12°$ and 20° to investigate further the characteristics of the first hump. The instantaneous stream-wise velocity field and the covariance plot, obtained by considering the pressure signals filtered in the first hump frequency range, are shown respectively in figure 3.16 (a) and (b), for the case with $\alpha = 20°$. Compared to the baseline case, figure 3.16 (a) shows that the extended separated flow, identified by the low-velocity blue region, moves upstream. Figure 3.16 (b) displays the first-hump pattern with wider coherent structures, which corresponds to lower frequencies. Larger vortices, whose size was related to v, are shed upstream of the mid-chord at a lower frequency. Hence, the Strouhal number of the first spectral hump $St_v = fv/U_0$ remains unchanged. In the BFS flow, the vortices are shed once they reach a size equal to the step height (Hudy

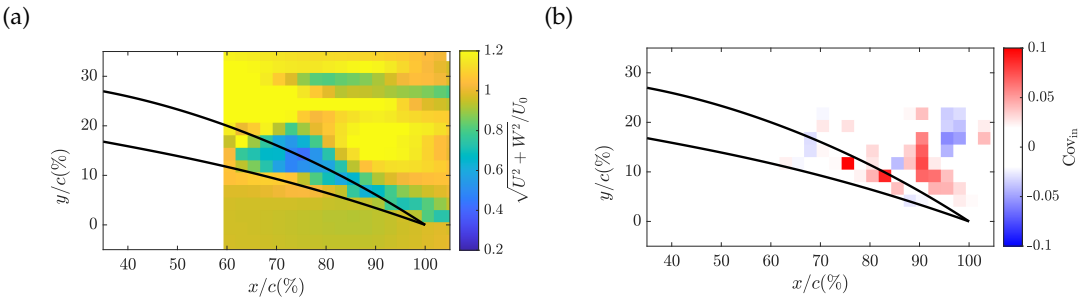

Figure 3.17: Configuration $\alpha = 12°$ and $e = 10$ mm. (a) Mean velocity filed of the resultant velocity in the $x - z$ plane measured withing the gap with $\mathrm{HWA}_{\mathrm{hor}}$. (b) Covariance plot obtained by relating the velocity fluctuations, measured in the $x - z$ plane using $\mathrm{HWA}_{\mathrm{hor}}$, with the pressure signals filtered in the first hump frequency range, $St_c = 2 - 5.5$.

et al., 2007). For $\alpha = 20°$, the shedding of larger vortices starts upstream of the mid-chord where the local thickness τ of the aerofoil is greater compared to that at the mid-chord, where the shedding occurs for the baseline case. This result suggests a link between τ and the size of the vortices. However, further studies are necessary to fully understand this dependency, taking into account factors such as the thickness-to-gap ratio defined by Denton (1993), where the separated flow reattaches to the aerofoil tip when $\tau/e > 4$, the pressure difference between the two sides of the aerofoil and the position of the TLV.

Focusing on the configuration with $\alpha = 12°$, the first hump occurs at higher frequencies as seen in figure 3.15 (a). Therefore, narrower coherent structures are expected, which are qualitatively shown in the covariance plot in figure 3.17 (b). Smaller vortices are expected to be shed in an aerofoil section characterised by a smaller local thickness. This aligns with the extended separated flow found downstream of the 75% of the chord, as shown in the mean flow field of figure 3.17 (a).

These considerations provide insight into the broadband characteristic of the first hump, rather than an expected tonal feature associated with a vortex-shedding phenomenon (Gerrard, 1955). The first-hump frequency changes depending on where the extended separation occurs. In section 3.3, for simplicity, we considered a cross-section around $x/c = 60\%$. However, the extended separated region extends between the 50 and 75% of the chord, as shown in figure 3.11. This means that different aerofoil sections, with different local thicknesses, shed vortices of different sizes which contribute to the broadband characteristic of the first hump. The two cases analysed in this section seem to confirm this observation. The $\alpha = 20°$ case presents a broader first hump and a wider separated flow region from 40 to 70% of the chord, whereas the $\alpha = 12°$ case presents narrower hump and smaller separated flow region around the aerofoil trailing edge.

Figure 3.18 (a) shows the pressure distributions C_p along the aerofoil suction side for

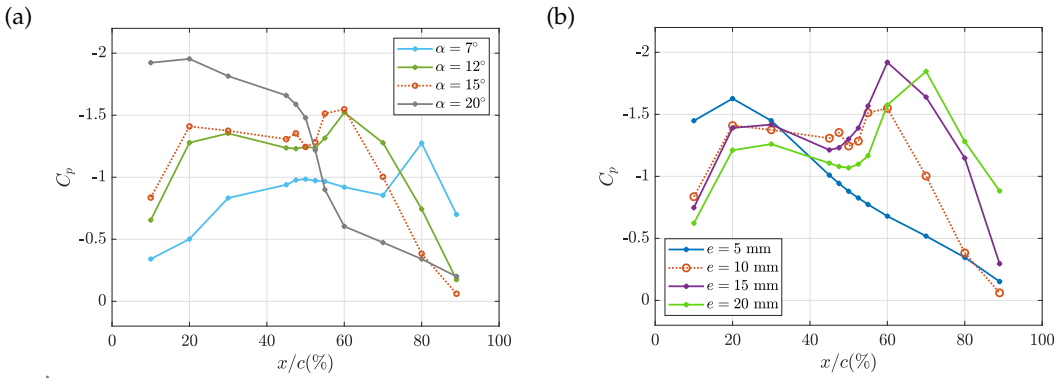

Figure 3.18: Pressure distribution C_p over the aerofoil suction side for different configurations obtained by varying the angle of attack α while keeping the gap size $e = 10$ mm (a), and by changing e for a constant $\alpha = 15°$ (b).

the configurations obtained by varying the angle of attack. As the angle of attack decreases, the pressure drop moves downstream, consistent with the shift of the extended separated flow region towards the trailing edge, as seen in figure 3.16 (a) and 3.17 (a). This trend seems to confirm the influence of the TLV on the tip leakage flow behaviour. The TLV, which aligns with the inflow direction (Decaix et al., 2015; Koch et al., 2021), deviates from the aerofoil suction side further downstream when the angle of attack decreases. For $\alpha = 7°$, the separated zone eventually vanishes resulting in the absence of the first hump in figure 3.15 (a). In contrast, the "flat" spectrum obtained for $\alpha = 30°$ is likely due to the stall of the aerofoil. Chapter 4 explores the influence of the TLV on the separated flow in detail.

The pressure distributions C_p along the aerofoil suction side for the cases obtained by varying the gap size are plotted in figure 3.18 (b). The pressure drop moves progressively towards the trailing edge as the tip gap increases from $e = 10$ to 20 mm, in agreement with Storer and Cumpsty (1991). This explains the shifting of the first hump towards higher frequencies seen in figure 3.15 (b), similar to that observed for the case with $\alpha = 12°$. However, no first hump is found for $e = 5$ mm even though its pressure distribution has a shape similar to that of $\alpha = 20°$. The reason is due to the absence of the extended separated flow, as shown in the instantaneous stream-wise velocity field of figure 3.19 (a). The uniform velocity vectors along the aerofoil pressure side suggest a flow acceleration entering the gap.

3.4.2 Further considerations about second hump

Figures 3.15 (a) and (b) show that the tip leakage noise exhibits a similar trend in the frequency range of the second hump. Specifically, the configuration with $e = 5$ mm is characterised by a covariance plot similar to that of the baseline case, as can be seen comparing figures 3.19 (b) and 3.9 (a). The presence of the second hump, along with the absence of an extended separated flow region seen in figure 3.19 (a), allows us to

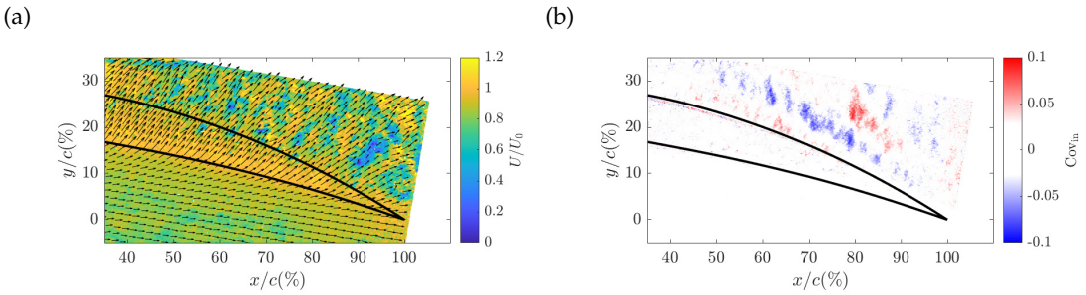

Figure 3.19: Configuration $\alpha = 15°$ and $e = 5$ mm: (a) instantaneous velocity field of the stream-wise velocity component with velocity vectors measured with $\mathrm{PIV_{in}}$. (b) Covariance plot obtained by relating the velocity fluctuations, measured in the y-direction using $\mathrm{PIV_{in}}$, with the pressure signals filtered in the second hump frequency range, $St_c = 5.5 - 13$.

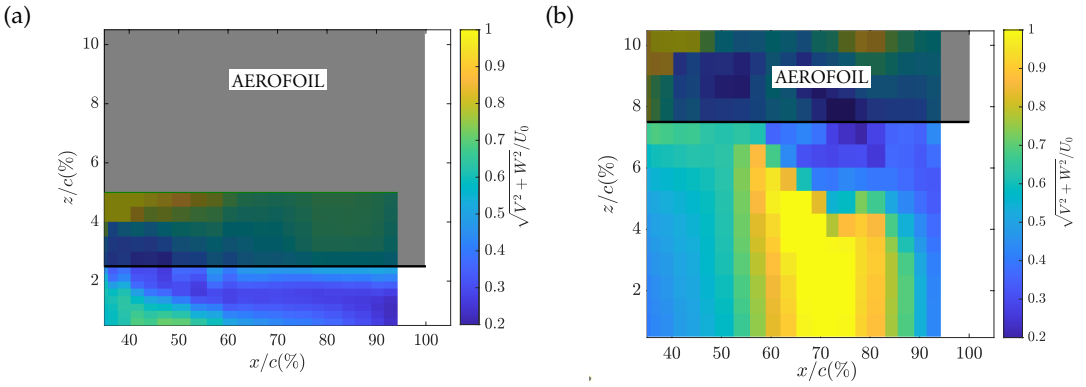

Figure 3.20: Mean velocity fields of the resultant velocity in the $y - z$ plane measured along the aerofoil suction side with $\mathrm{HWA_{ver}}$, for two configurations characterised by $e = 5$ mm (a) and $e = 15$ mm (b), and angle of attack $\alpha = 15°$.

consider the tip flow characterised by a localised separation, as sketched in figure 3.14 (a). However, the second-hump pattern is detected beyond the aerofoil suction side as the shear layer vortical structures persist beyond the reattachment, as occurs in a BFS flow (Kostas et al., 2002).

In section 3.3, we defined the non-dimensional frequency for the second hump as $St_b = fb/U_{SL} = 0.2$. However, since the second-hump frequency does not change significantly with varying the gap size, the other two parameters b and U_{SL} vary accordingly, meaning that if b increases, U_{SL} should also increase, and vice versa. This behaviour is qualitatively evident when comparing the contour plots in figures 3.20 (a) and (b). These plots show the mean velocity measured using HWA for the two configurations with $e = 5$ and 15 mm. In the latter case, a shear layer is observed slightly downstream of the mid-chord around $x/c = 60 - 85\%$, in agreement with the shifting of the pressure drop towards the trailing edge and of the first hump towards higher frequencies. This region is characterised by the separated flow region below the tip edge and the consequent high-speed jet in the bottom part of the figure. In the former case, a small velocity gradient is observed below the tip around the $x/c = 40 - 60\%$.

The growth of the velocity gradient, as the gap size increases, can explain the increase in tip noise intensity observed in figure 3.15 (b) as the gap size increases.

3.5 Conclusions

The tip leakage noise for a single-stationary aerofoil has been investigated experimentally in this chapter. Simultaneous near and far-field pressure measurements were conducted, along with PIV and HWA. Two distinct dipole-type noise sources have been identified within two non-dimensional frequency ranges $St_c = fc/U_0 = 2 - 5.5$ and $5.5 - 13$, attributed to fluid-dynamic instabilities occurring within the tip gap: a vortex-shedding type phenomenon and shear layer roll-up.

The tip flow, driven by the pressure difference across the aerofoil, enters the gap and separates at the pressure-side edge. The subsequent shear layer roll-up forms vortical structures of a size equivalent to the shear layer thickness b at the frequency of the second tip noise source. The corresponding non-dimensional frequency is $St_b = fb/U_{SL} = 0.2$, where U_{SL} is the shear-layer average velocity. Successively, the separated flow can either reattach to the aerofoil tip or remain separated until the exit of the gap. In case of extended separation, the vortical structures can achieve a certain size and be shed at the non-dimensional frequency $St_v = fv/U_0 = 0.07$. In this case, f is centred in the frequency range of the first noise source, and v is the width of the separated flow measured at the exit of the gap. It has been hypothesised that the TLV influences the tip flow behaviour: its presence close to the aerofoil suction side helps the separated flow to reattach to the aerofoil tip. Chapter 4 provides detailed analysis of this TLV effect.

The frequency of the first noise source depends on the position of the extended separated flow along the chord. As the angle of attack decreases or the gap size increases, the separated flow moves towards the aerofoil's trailing edge. As a result, the frequency of the first noise source increases and the spectrum becomes narrower. The second noise source gives rise to multiple spectral peaks at frequencies that are consistent across different configurations. The presence of the first noise source implies the existence of the second, but not vice versa. Vortex shedding occurs only when the separated flow does not reattach at the aerofoil tip, while the roll-up always occurs within the tip gap. In Chapter 4, three non-dimensional parameters influencing the tip noise sources will be identified.

Chapter 4

Influence of non-dimensional parameters on the tip leakage noise

This chapter investigates three key non-dimensional parameters influencing the tip leakage noise sources: the angle of attack α, the ratio between maximum aerofoil thickness and gap size τ_{max}/e, and the ratio between gap size and wall boundary layer thickness e/δ. The vortex-shedding noise source develops when $\tau_{max}/e < 4$ and with the tip vortex positioned away from the aerofoil surface for $\alpha \geq 10°$. The roll-up noise source occurs whenever the tip flow separates at the pressure side edge, with its strength proportional to the lift coefficient, depending on α, and diminishing as e/δ decreases and τ_{max}/e increases.

4.1 Background

The small clearance between a ducted fan rotor and its surrounding casing is a region of three potential broadband noise sources: fan-boundary layer interaction noise, trailing edge noise and tip leakage noise (Ganz et al., 1998). However, the distinction between these noise sources in a representative fan rig has been a persistent challenge. Grilliat et al. (2007) developed an experimental set-up with a single-stationary aerofoil positioned in the core of a wind tunnel jet to focus specifically on the tip leakage noise. This noise arises from interactions between the tip leakage flow, which develops within the clearance due to the pressure difference between the airfoil's pressure and suction sides, the blade tip and the casing wall boundary layer. The tip leakage flow also interacts with the incoming flow, forming a vortex structure known as tip leakage vortex. Two distinct tip leakage noise sources were identified, both linked to flow separation at the pressure side tip (Jacob et al., 2010; Camussi et al., 2010). According to Liu et al. (2024), this separation excited an unsteadiness that is sustained by its interaction with the incoming flow, propagating into the TLV core.

In Chapter 3, we experimentally identified the fluid-dynamic instabilities responsible for two dipole-type tip noise sources: vortex-shedding and shear layer roll-up. Both instabilities were linked to the behaviour of the tip flow after its separation at the pressure side edge. The vortex-shedding phenomenon occurs when the tip flow does not reattach to the aerofoil, and within the non-dimensional frequency range $St_c = fc/U_0 = 2 - 5.5$. In contrast, the shear layer roll-up develops regardless of whether the tip flow reattaches or remains separated, within $St_c = 5.5 - 13$. Here, f is the frequency, c is the chord length, and U_0 is the inflow velocity. The frequency content of the first noise source was found to vary with the chord-wise position of the extended separated flow, which shifts based on the angle of attack and gap size. In contrast, the second noise source produces multiple spectral peaks that remain repeatable across different configurations. In Chapter 6, we employ Large Eddy Simulations (LES) to investigate two aerofoil cross-sections where the tip flow behaviour changes, from a reattachment to an extended separated flow, providing a clear overview of the flow topology and confirming the presence of the two fluid-dynamic instabilities responsible for the noise sources. However, no effort has been made to investigate the key non-dimensional parameters governing the tip leakage noise sources.

4.1.1 Tip leakage flow influences

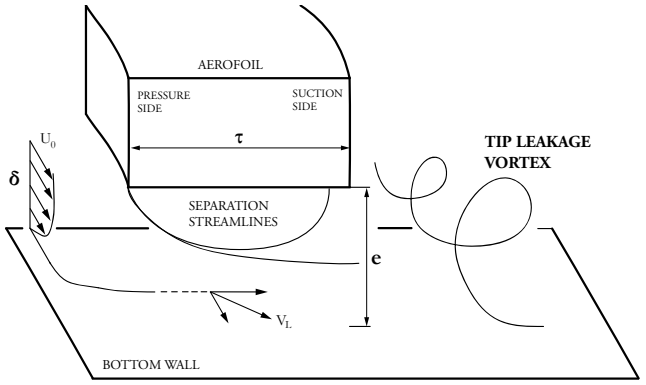

Figure 4.1: Schematic representation of the parameters influencing tip leakage flow behaviour in an aerofoil cross-section: blade thickness τ, gap size e, tip leakage vortex on the aerofoil suction side and boundary layer thickness δ of the incoming flow U_0. V_L is the tip flow velocity close to the bottom wall.

The behaviour of the tip leakage flow plays a crucial role in the generation of associated tip noise sources. While past studies have identified certain dependencies of the tip leakage flow, the exact nature of their influence has remained largely unexplored. This work systematically investigates these dependencies and their interactions to establish their role in tip leakage noise generation. Figure 4.1 illustrates a simplified aerofoil cross-section highlighting the parameters suggested to influence the tip leakage flow. The flow behaviour can vary depending on whether the section is characterised by a certain thickness-to-gap ratio τ/e, and its position relative to the tip leakage vortex,

which is influenced by the angle of attack α and the gap size e. The tip flow can also be influenced by whether the aerofoil tip is immersed in the casing boundary layer of thickness δ.

Storer and Cumpsty (1991) observed that the tip leakage flow does not reattach at the aerofoil downstream of the position of the minimum pressure measured on the endwall. This behaviour was suggested to be related to the ratio between the blade thickness τ and tip gap size e, which was at most 2.5, a value significantly lower than 7 measured by Moore and Tilton (1988), where the tip flow was observed to reattach to the aerofoil at the location downstream of the minimum pressure on the suction side. Graham (1986) measured the velocity profiles at a location close to the aerofoil suction side for three gap sizes, ranging from $\tau/e = 2.5$ to 5.2. The flow did not reattach in the configuration with the largest gap size, whereas a fully developed profile was observed for the smallest gap size case. The thickness-to-gap ratio was measured perpendicular to the chamberline, as Rains (1954) noted that the pressure gradient across the aerofoil is significantly larger than that along the chord, causing the tip flow to enter the clearance in a direction normal to the camber line. Denton (1993) suggested $\tau/e = 4$ as a threshold based on these past studies, indicating that for $\tau/e > 4$, typical in turbines, the tip flow generally reattaches before leaving the gap, whereas in compressors, where this ratio is often lower, reattachment is unlikely. Dambach and Hodson (2001) found even higher ratio, between 5 and 6, for a rotating blade. However, these studies (Graham, 1986; Storer and Cumpsty, 1991; Dambach and Hodson, 2001) were carried out using a single aerofoil while varying only the gap size. One of the key contributions of this study is demonstrating the significance of the thickness-to-gap ratio by varying both aerofoil thickness and gap size, and quantifying its impact on the tip leakage flow and associated noise.

Storer and Cumpsty (1991) also observed that upstream of the position of minimum pressure measured on the wall, which corresponds with the trajectory of the tip leakage vortex, the nature of the tip flow differed, with the flow reattaching to the aerofoil. Specifically, Intaratep (2006) found that the minimum pressure measured along the aerofoil suction side coincides with the position where the vortex begins to separate from the aerofoil surface. As the tip gap increases, the vortex moves further downstream, similar to when decreasing the angle of attack, as noted by Kang and Hirsch (1994). In Chapter 3, an interaction between the moving away of the vortex from the aerofoil surface and the onset of extended separated flow was suggested, as indicated by a shift in the pressure peak in the pressure distribution C_p that corresponds to a relocation of the extended separated region. However, this interaction could not be verified, as no measurements of the tip vortex were performed.

Regarding the casing boundary layer, Zhang et al. (2022) observed that its interaction with the tip flow resulted in weakened pressure fluctuations near the onset of the tip leakage vortex. To investigate this interaction, the aerofoil tip was immersed within

the boundary layer, resulting in a gap-to-boundary layer thickness $e/\delta < 1$. This differs from past investigations (Moore and Tilton, 1988; Storer and Cumpsty, 1991), where the gap size was larger than the boundary layer. According to Jacob et al. (2016a), a thinner boundary layer reduces the interaction noise between the upstream turbulence and the aerofoil leading edge, which might be responsible for a large part of the background noise masking the tip leakage noise in their pressure measurements.

4.1.2 Novel contributions of the current chapter

The previous chapter identified two tip leakage noise sources for a single-stationary aerofoil, specifically attributed to fluid-dynamic instabilities occurring within the tip gap: vortex-shedding and shear layer roll-up. These instabilities are connected to the behaviour of the tip flow after it separates at the pressure side tip. If the flow does not reattach to the aerofoil, both instabilities occur; if reattachment occurs, only roll-up is observed.

In this chapter, a systematic parametric study was carried out, analysing a wide range of configurations obtained by combining six distinct aerofoils with various gap sizes, testing seven angles of attack for each configuration, and considering two boundary layer thicknesses. Through this extensive analysis, three non-dimensional parameters were identified as the most influential on tip leakage flow and associated noise sources: angle of attack α, maximum thickness-to-gap ratio τ_{max}/e and gap-to-boundary layer thickness e/δ, as summarised in the following relationship:

$$\overline{p'^2} \propto f(\alpha, \tau_{max}/e, e/\delta) \tag{4.1}$$

where $\overline{p'^2}$ represents the pressure fluctuations associated with the tip leakage noise sources.

The first noise source develops when $\tau_{max}/e < 4$ and with the tip leakage vortex away from the aerofoil surface for $\alpha \geq 10°$. The location of the vortex detachment from the aerofoil surface can be identified by the minimum pressure peak in the pressure distribution C_p along the aerofoil suction side tip. The magnitude of this peak, directly linked to the noise source strength, depends on the three non-dimensional parameters. The second tip noise source occurs whenever the tip flow separates at the pressure side. Its strength is mainly proportional to the lift coefficient C_l, depending on α, and it decreases as e/δ decreases and τ_{max}/e increases.

This chapter is structured as follows: in section 4.2, the influence of the angle of attack on the tip noise sources is investigated for configurations with the same aerofoil and boundary layer thickness (NACA 5510 and $\delta = 5$ mm). These initial findings are then generalised by considering different aerofoils, emphasizing the impact of the

thickness-to-gap ratio in section 4.3. The influence of boundary layer thickness is discussed through these sections and is completed by examining another boundary layer thickness in section 4.4.

4.2 Influence of the angle of attack α

4.2.1 Tip leakage vortex detachment on tip separated flow

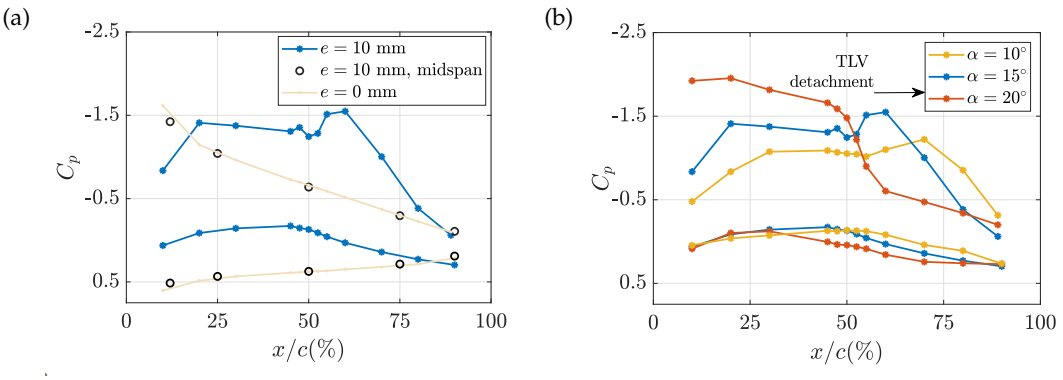

Figure 4.2: (a) Pressure distributions C_p along the aerofoil measured at the tip for two configurations with gap sizes $e = 0$ and 10 mm, and at midspan for $e = 10$ mm. The angle of attack is set to $\alpha = 15°$. (b) Pressure distribution C_p measured at the tip for three configurations with $\alpha = 10°, 15°$ and $20°$. The gap size is set to $e = 10$ mm, corresponding to $\tau_{max}/e = 2$.

The pressure distributions C_p along the aerofoil measured close to the tip for two gap sizes $e = 0$ and 10 mm, and same angle of attack $\alpha = 15°$, are shown in figure 4.2 (a), together with that evaluated at midspan for $e = 10$ mm. In the presence of the gap, the pressure distribution near the tip changes significantly compared to that at midspan, which corresponds to the loading at the tip without clearance, in agreement with previous studies (Jacob et al., 2010; Koch et al., 2021). This indicates that the gap mainly influences the pressure distribution near the tip edge. The loading on the pressure side tends to be lower in the presence of a gap, particularly upstream of the midchord. On the suction side, the pressure decreases downstream of the leading edge reaching a peak around the 60% of the chord, followed by a subsequent drop. The magnitude of the peak and its location along the chord vary with changes in the angle of attack, as shown in figure 4.2 (b). Specifically, when the angle of attach decreases from $20°$ to $10°$, the magnitude of the peak on the suction side diminishes, and the drop shifts downstream, from midchord to 75% of the chord.

Previous studies linked the loading on the aerofoil suction side to the tip leakage vortex (Graham, 1986; Kang and Hirsch, 1993), which remains near the aerofoil surface. The pressure peak, followed by the drop, occurs when the vortex moves away from the surface (Intaratep, 2006). According to figure 4.2 (b), this vortex detachment shifts

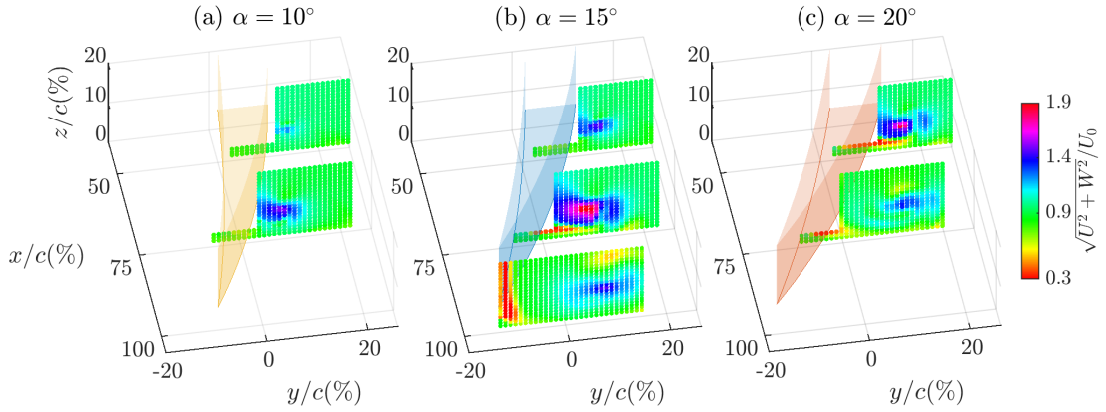

Figure 4.3: Mean velocity fields of the resultant velocity in the $x - z$ plane measured for three configurations with $\alpha = 10°$ (a), $15°$ (b) and $20°$ (c) in different chord-wise sections: at midchord, at 75% of the chord and at 2 mm downstream the trailing edge. The gap size is set to $e = 10$ mm, corresponding to $\tau_{max}/e = 2$.

progressively upstream with the increase of the angle of attack. This behaviour is qualitatively shown in figure 4.3, which displays the resultant velocity contained in the $x - z$ plane measured by the hot-wire probe in different chord-wise sections, precisely at $x/c = 50\%$, 75% and at 2 mm downstream of the trailing edge, for the three configurations with $\alpha = 10°, 15°$ and $20°$. The resultant velocity reaches maximum values in the vortex core. The location of this maximum velocity indeed matches with the centre of the TLV identified by Jacob et al. (2016a) at the same chord-wise section located downstream of the trailing edge, for the configuration with $\alpha = 15°$ shown in figure 4.3 (b). For this configuration, the trajectory of the TLV can be qualitatively inferred from the three sections, showing that it is almost aligned with the inflow direction, consistent with figure 3.13 and other works (Jacob et al., 2016b; Koch et al., 2021). The vortex core remains close to the aerofoil suction side up to the midchord, and then it starts to move away, as expected from its pressure distribution (–) in figure 4.2 (b). For $\alpha = 10°$ in figure 4.3 (a), the vortex core remains close to the aerofoil suction side up to the 75% of the chord, whereas for $\alpha = 20°$ in figure 4.3 (c), the core begins to move away from the surface around the midchord. In summary, the relationship between the tip leakage vortex and the pressure distributions on the aerofoil suction side is clear, with the location of vortex detachment shifting as the angle of attack changes. Furthermore, the vortex is located near the aerofoil tip, so it does not influence the pressure at the midspan. As a result, the pressure distribution at the midspan remains similar to that of the configuration without a gap, as seen in figure 4.2 (a).

Hot-wire measurements were used to trace the vortex core in the suction side area of the aerofoil and evaluate the flow within the gap. The tip flow exhibits low-velocity values at midchord for the configuration with $\alpha = 20°$ in figure 4.3 (c), and at 75% of chord for $\alpha = 15°$ and $20°$, in (b) and (c). Figure 4.4 displays this characteristic more clearly, showing the flow fields in the mid-gap plane for these three configurations with

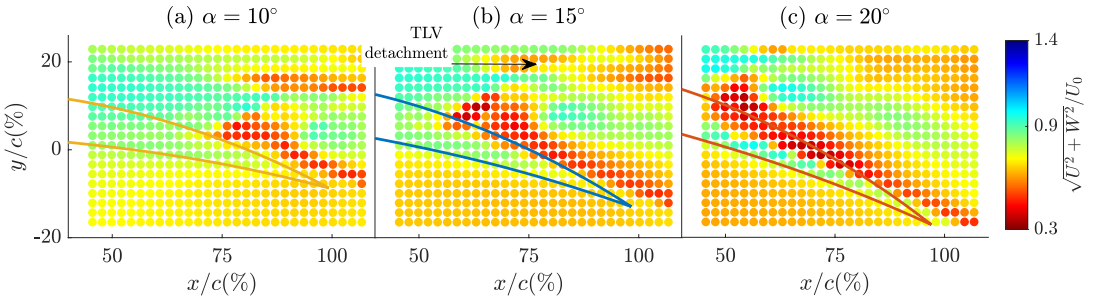

Figure 4.4: Mean velocity fields of the resultant velocity in the $x - z$ plane measured within the gap for three configurations with $\alpha = 10°$ (a), $15°$ (b) and $20°$ (c). The gap size is set to $e = 10$ mm, corresponding to $\tau_{max}/e = 2$.

$\alpha = 10°, 15°$ and $20°$. The low-velocity regions, found for each case in figure 4.4, arise downstream of the pressure peaks identified in the pressure distributions in figure 4.2 (b). The low-velocity region shifts upstream as the angle of attack increases, following the same shifting trend as the pressure peaks. Given the connection between the pressure peak and low-velocity region, as well as between the peak and vortex detachment, it can be suggested that the tip leakage vortex plays a role in the development of the low-velocity region.

In Chapter 6, LES simulations are used to investigate two chord-wise sections of the configuration with $\alpha = 15°$, specifically at midchord and at 75% of the chord. At midchord, the flow was found to separate at the tip but to reattach before leaving the gap. At 75% of the chord, the tip flow remained separated until the exit of the gap and low-axial velocity was measured. This low-velocity region corresponds to those observed in figures 4.3 and 4.4. Figure 4.3 also indicates that the extended separated flow occurs when the TLV is away from the aerofoil suction side. A similar trend was observed by Liu et al. (2024), who found an extended separation developed within the gap downstream of the TLV detachment from the aerofoil surface, while upstream, the flow remained steady and attached. This trend suggests that when the TLV is close to the aerofoil surface, its low pressure can influence the separated flow to reattach to the aerofoil tip. However, as the TLV moves away, this effect vanishes, and the tip flow stays separated until it exits the gap. Figure 4.4 also shows that the velocity values within the low-velocity region decrease as the angle of attack increases. This behaviour appears to be correlated with the intensity of the pressure peaks: as the pressure peak magnitude increases, the vortex is characterised by lower pressure, which may lead to a stronger separation upon its detachment.

Figure 4.5 shows the lift coefficient C_l as a function of the angle of attack α for different gap sizes e. The gap size has been non-dimensionalised using the maximum thickness of the 5510 aerofoil, i.e. $\tau_{max} = 20$ mm. The lift coefficient remains nearly constant as the gap size varies and for a fixed angle of attack. This is unexpected given that the

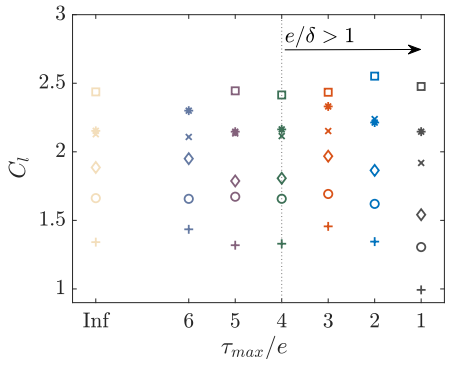

Figure 4.5: Lift coefficient C_l plotted against the non-dimensionalised gap size τ_{max}/e, obtained for different angles of attack. The markers refer to the angles of attack: + 5°, o 7°, ♢ 10°, x 12°, * 15°, □ 17°.

pressure distributions with and without the gap differ significantly, as shown in figure 4.2 (a). Based on this figure, it can be hypothesized that, to keep the lift coefficient constant, the loading on the pressure side is reduced in the presence of the gap to counterbalance the loading on the suction side caused by the TLV. However, the effect of the gap size on the lift coefficient becomes evident for large gaps ($\tau_{max}/e > 2$) and small angles of attack ($\alpha < 12°$), resulting in a significant reduction in lift.

4.2.2 First tip noise source

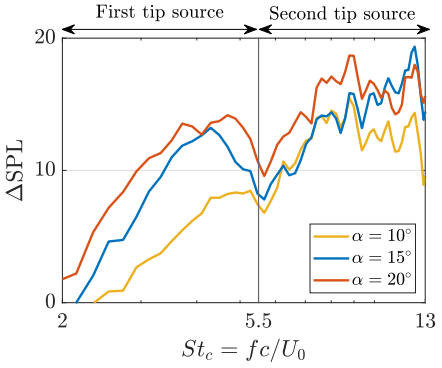

Figure 4.6: Tip leakage noise obtained by subtracting the Sound Pressure Levels measured with and without the gap, for the three configurations with $\alpha = 10°$, 15°, and 20° and gap size $e = 10$ mm, corresponding to $\tau_{max}/e = 2$.

The focus on the low-velocity region is due to its association with a vortex-shedding type phenomenon, which was identified as one of the two tip leakage noise sources in Chapter 3. This noise source was linked to the spectral humps found in figure 4.6, within the non-dimensional frequency range $St_c = fc/U_0 = 2 - 5.5$. The curves plotted in this figure are obtained by subtracting the far-field spectra obtained with and without the gap to highlight the noise increase due to the tip leakage noise. As the angle of attack decreases, the spectral hump narrows and its peak shifts towards higher

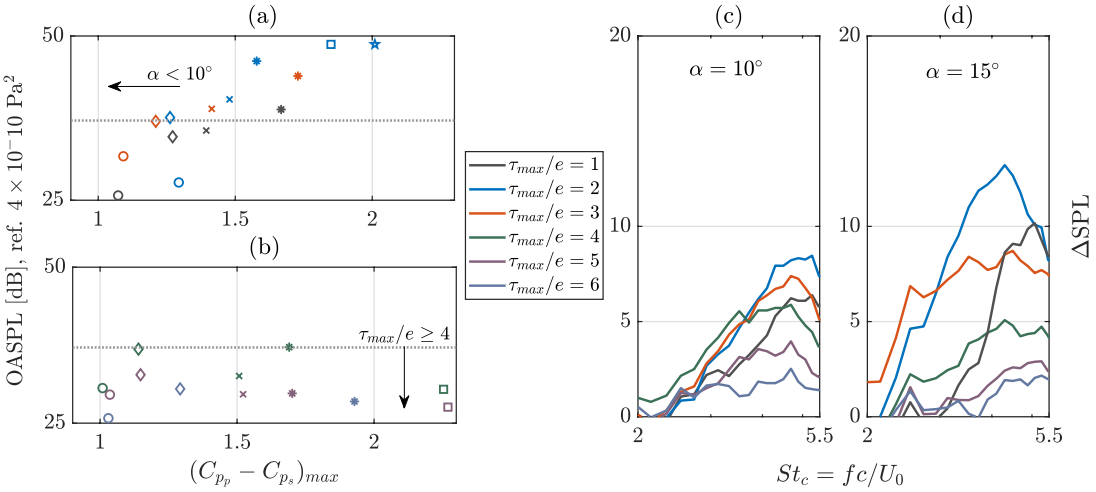

Figure 4.7: Overall Sound Pressure Levels evaluated in the frequency range of the first tip noise source against the maximum difference between C_{p_p} and C_{p_s}, for different configurations characterised by $\tau_{max}/e = 1, 2$ and 3 (a), and $\tau_{max}/e = 4, 5$ and 6 (b). Tip leakage noise for different configurations with $\alpha = 10°$ (c) and $15°$ (d). The markers refer to the angles of attack: o $7°$, $\diamond$ $10°$, x $12°$, * $15°$, $\square$ $17°$, $\star$ $20°$.

frequencies. This behaviour was associated with the location where the low-velocity region starts to appear. As a result of the previous considerations, the first tip noise source depends on the TLV detachment location.

The peaks on the pressure distributions along the suction side have been linked to the flow separation: a higher peak indicates stronger separation, which may lead to more intense vortex-shedding phenomena responsible for the first tip noise source, explaining the louder spectral peak observed in figure 4.6 as the angle of attack increases. This relationship between pressure peak and noise strength is further shown in figure 4.7 (a), where the spectral curves, integrated within the frequency range of the first noise source, are plotted as a function of the maximum pressure peak of the pressure distribution along the aerofoil suction side, C_{p_s}, on the abscissa. Specifically, the abscissa has been "normalised" by considering the maximum difference between C_{p_p} and C_{p_s}, to account for the effect of the TLV on the pressure distribution of aerofoil pressure side C_{p_p}, as suggested previously. The blue data points in figure 4.7 (a) correspond to the configurations with $e = 10$ mm, i.e. $\tau_{max}/e = 2$, for different angles of attack. The strength of the first noise source exhibits a sudden increase when passing from $\alpha = 7°$ to $10°$, followed by a rise that reaches its maximum at $\alpha = 20°$. Beyond this point, stall occurs at $\alpha = 30°$, as reported in figure 3.15 (a). The other cases shown in figure 4.7 (a) with $\tau_{max}/e = 1$ and 3 display the same trend, albeit with lower maximum intensity. On the contrary, the points for the cases with $4 \leq \tau_{max}/e \leq 6$ mainly cluster below the dotted line in figure 4.7 (b).

The clustering below the dotted line, along with the sudden drop in the noise strength at small angle of attack ($\alpha < 10°$), is associated with the absence of the first noise source. The dotted line is defined based on the observation that the case with $\tau_{max}/e = 4$ and

$\alpha = 15°$ was found to neither exhibit the first noise source nor extended separated flow, as seen in figure 3.19 (a) and 3.15 (b). Figure 4.7 (d) shows the tip leakage noise obtained for this case (–), along with those obtained for $1 \leq \tau_{max}/e \leq 6$. The spectral humps remain negligible, below 5 dB, for $\tau_{max}/e \geq 4$. Other data points are found along the dotted line for $\alpha = 10°$ in figure 4.7 (a) and (b), and their tip noise spectra are shown in (c). The case with $\tau_{max}/e = 2$ (–) is characterised by a shallow spectral peak and low-velocity region, as seen in figure 4.4 (a). This hump decreases as τ_{max}/e increases, approaching 5 dB for $\tau_{max}/e = 4$, and eventually becomes negligible, below 5 dB, for higher values. In summary, the first noise source does not develop for $\tau_{max}/e \geq 4$ and $\alpha < 10°$. The reason why the data for $\tau_{max}/e \geq 4$ collapse below the dotted line will be shown to be linked to the ratio between the aerofoil thickness and the gap size, despite these configurations having their tips immersed within the boundary layer. The absence of the first noise source for $\alpha < 10°$ is attributed to the lack of extended separated flow, which may result from the vortex detachment occurring even further downstream of 75% of the chord. Additionally, it should be considered that the tip flow changes as the angle of attack decreases, with a much weaker cross-stream flow forming even further downstream of 75%, as observed by Jacob et al. (2010) for the configuration with $\alpha = 5°$ and $\tau_{max}/e = 2$.

4.2.3 Second tip noise source

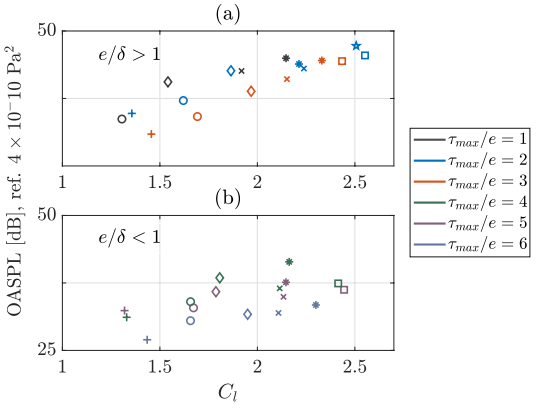

Figure 4.8: Overall Sound Pressure Levels evaluated in the frequency range of the second noise source against the lift coefficient C_l measured at the tip for different configurations characterised by $\tau_{max}/e = 1, 2$ and 3 (a), and $\tau_{max}/e = 4, 5$ and 6 (b). The markers refer to the angles of attack: + 5°, o 7°, ◇ 10°, x 12°, * 15°, □ 17°, ⋆ 20°.

The second tip noise source was associated with a shear layer roll-up, which develops within the gap due to the separation of the flow at the pressure side tip edge. Figure 4.6 identifies the noise increase due to this fluid dynamic instability within $St_c = 5.5 - 13$. As the angle of attack increases, the levels rise reaching the greatest values for the configuration with $\alpha = 20°$. The integration of the curves in figure 4.6 over the corresponding frequency range of the second noise source results in the scatter plot of figure 4.8

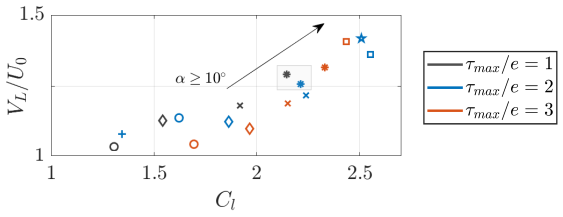

Figure 4.9: Tip flow velocity V_L plotted against the lift coefficient C_l, obtained for $\tau_{max}/e = 1, 2$ and 3. The markers refer to the angles of attack: + 5°, o 7°, ♢ 10°, x 12°, * 15°, □ 17°, ⋆ 20°.

(a) and (b), where the abscissa represents lift coefficient C_l, obtained by integrating the pressure distributions along the chord. These figures have been enhanced with additional data points obtained by varying the angle of attack, between 5° and 20°, and gap size, between $1 \leq \tau_{max}/e \leq 6$. Specifically, the cases with $\tau_{max}/e \leq 3$, also characterised by the aerofoil tip outside the boundary layer $e/\delta > 1$, are shown in (a), while the others are presented in (b). Figure 4.8 (a) shows a proportionality between the strength of the second tip noise source and the lift coefficient. In figure (b), for $e/\delta < 1$, the data appear slightly more dispersed but still show an increase of the noise source with the lift coefficient. A detailed analysis of this data, including the effects of the casing boundary layer, will be conducted in the next sections.

The proportionality, shown in figure 4.8 (a), between the overall loading acting on the aerofoil tip and the strength of the second tip noise source, is not straightforward. This noise source was linked to the shear layer roll-up, which develops from the separation of the flow entering the gap at the pressure side edge. The roll-up is due to the Kelvin-Helmholtz instability, which arises from a velocity difference across the interface of two parallel fluid streams (Kundu et al., 2016). In the tip flow scenario, these streams are represented by the separated flow near the aerofoil tip and a high-speed jet flow close to the bottom wall, as observed in figure 3.12 and also by Storer and Cumpsty (1991). Since the separated flow near the aerofoil has negligible velocity, the roll-up mechanism is primarily influenced by the flow velocity near the wall, V_L. A way to estimate of this velocity, normal to the chamber line, was provided by Rains (1954), using the following expression: $V_L/U_0 = \sqrt{C_{p_{p,m}} - C_{p_s}}$, where $C_{p_{p,m}}$ is the pressure coefficient measured at midspan on the aerofoil pressure side and C_{p_s} is that measured at the tip on the suction side. This formula was derived from the ideal model, proposed by Rains (1954), which applies the Bernoulli equation under the assumption of an ideal, unattached flow entering the gap normal to the chamber line. Consequently, as noted by Storer and Cumpsty (1991), this expression provides a good estimate of the flow velocity when applied to sections downstream of the minimum pressure on the suction side, where the flow tends to be unattached.

In this study, the flow velocity V_L is evaluated by considering the pressure coefficients measured at the location of the minimum pressure peak and at the aerofoil tip of both

sides, using this formula $V_L/U_0 = \sqrt{C_{p_p} - C_{p_s}}$, where C_{p_p} is the pressure coefficient measured at the pressure side tip. The scatter plot of figure 4.9 displays V_L plotted against the lift coefficient C_l, obtained by varying the angle of attack for all the configurations with the aerofoil tip outside the boundary layer to satisfy the assumption of ideal flow, i.e. $e/\delta > 1$ corresponding to $1 \leq \tau_{max}/e \leq 3$. The data show a linear relationship between V_L and C_l, which is evident for $\alpha \geq 10°$, but not for lower angles of attack, $\alpha < 10°$. This discrepancy may be due to the method of evaluating V_L, which relies on pressure coefficients measured at the same chord-wise location on both aerofoil sides, potentially causing inaccuracies in the velocity estimation at low angles of attack. At low angles of attack, the pressure tap locations almost align with the cross-stream direction, providing an estimate of the cross-stream flow, while the actual tip flow has both stream and cross-stream components. Additionally, at low angle of attack, the cross-stream flow is weaker, as observed by Jacob et al. (2010). As the angle of attack increases, the tip flow changes with a higher cross-stream component and the alignment of the pressure taps with the actual tip flow direction improves, leading to a more accurate estimation of V_L.

This section illustrates a linear relationship between the lift coefficient and the tip flow velocity, without claiming an exact value of V_L, due to the several assumptions inherent in Rains' model. This relationship helps to explain the connection between the lift coefficient and the strength of the second noise source observed in figure 4.8. As the lift coefficient increases, the greater pressure difference between the suction and pressure side results in a faster flow close to the bottom wall, forming stronger shear layer vortices and, consequently, a more intense tip noise source. In section 4.3.2, a power relationship between lift coefficient and strength of the second noise source will be presented.

4.3 Influence of the thickness-to-gap ratio τ/e

Denton (1993) suggested the behaviour of the tip leakage flow is a function of the ratio between the local aerofoil thickness τ and gap size e. When $\tau/e > 4$, the tip flow typically reattaches before leaving the gap, while for lower values, the flow is unlikely to reattach to the blade. In the previous section, a 5510 NACA aerofoil with $\tau_{max} = 20$ mm localised at 30% of the chord was considered. For the cases with non-dimensional gap sizes $\tau_{max}/e = 2$ shown in figure 4.3, this results in $\tau/e < 2$ along the entire chord, with the tip flow remaining separated unless the vortex is close to the airfoil surface, which encourages the reattachment. This separation leads to the first tip noise source, which tends to disappear for non-dimensional gap sizes $\tau_{max}/e \geq 4$, as seen in figure 4.7 (a) and (b). Given that the first tip noise source is intrinsically linked to the behaviour of the tip flow, this section investigates the influence of the thickness-to-gap ratio, by varying also the aerofoil thickness, on both first and second tip noise sources.

4.3.1 First tip noise source

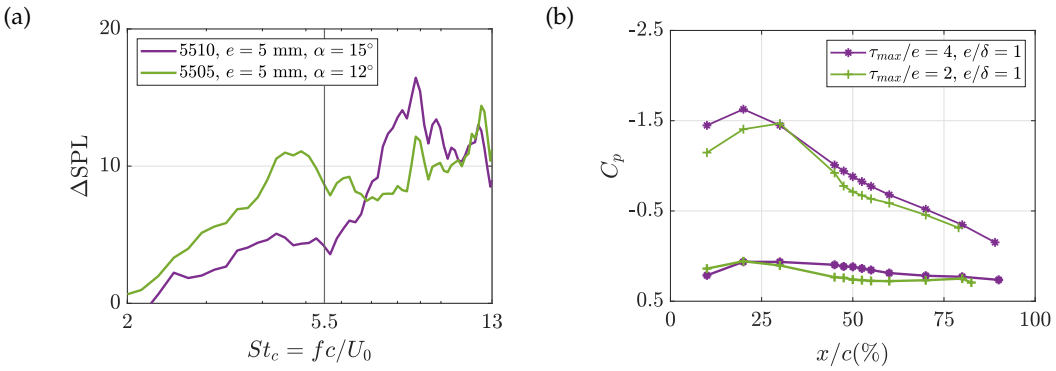

Figure 4.10: (a) Tip leakage noise and (b) pressure distributions C_p along the aerofoil measured at the tip for the two configurations with $\tau_{max}/e = 2, 4$ and angle of attack set to $\alpha = 12°, 15°$ respectively.

Two different NACA aerofoils, 5505 and 5510 with $\tau_{max} = 10$ mm and 20 mm, at different angles of attack, $\alpha = 12°$ and $15°$, were analysed in detail. Both featured a gap size of $e = 5$ mm, corresponding to $e/\delta = 1$. Figure 4.10 displays the tip leakage noise (a) and the pressure distribution C_p along the chord (b) obtained for these two configurations with $\tau_{max}/e = 2$ and 4. Although the pressure distributions are nearly identical, only the configuration with $\tau_{max}/e = 2$ exhibits a distinct spectral hump in the frequency range of the first noise source, $St_c = 2 - 5.5$, with a peak of 11 dB. This noise source suggests the development of a low-velocity region, expected to form at the location where the vortex detaches. According to the pressure distributions in figure 4.10 (b), the vortex detaches from the aerofoil surface around 25% of the chord, corresponding to the location of the maximum aerofoil thickness. This detachment is confirmed in figure 4.11, which displays the resultant velocity in the $x-z$ plane measured at the midchord and 75% of the chord. In both configurations, the trajectory of the vortex core,

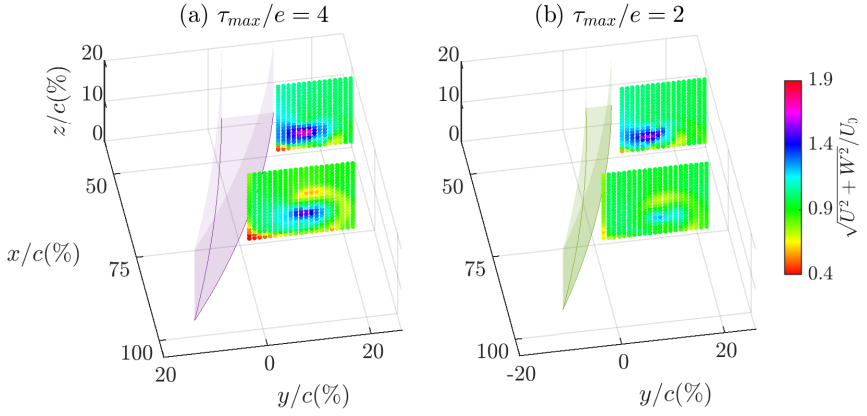

Figure 4.11: Mean velocity fields of the resultant velocity in the $x - z$ plane measured for two configurations with $\tau_{max}/e = 4$, $\alpha = 15°$ (a), and $\tau_{max}/e = 2$, $\alpha = 12°$ (b) in different chord-wise sections, midchord and 75% of the chord. Different aerofoils characterise these configurations, NACA 5510 and 5505.

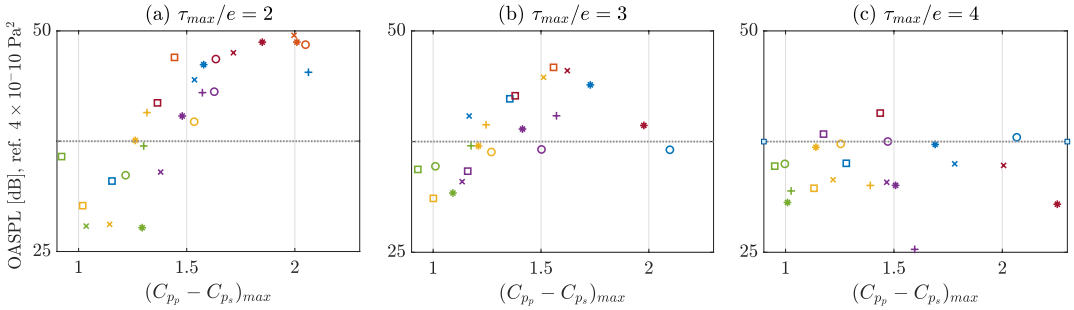

Figure 4.12: Overall Sound Pressure Levels evaluated in the frequency range of the first tip noise source against the maximum difference between C_{p_p} and C_{p_s}, for different configurations characterised by $\tau_{max}/e = 2$ (a), 3 (b) and 4 (c). The markers refer to the aerofoils: + 5505, o 5507, * 5510, x 5512, □ 5515. The colours refer to the angles of attack: 7° (–), 10° (–), 12° (–), 15° (–), 17° (–), 20° (–).

identified by maximum velocity values, is located further from the aerofoil surface in these sections downstream of 25% of the chord. At 25% of the chord, the difference between the two configurations is the thickness-to-gap ratio: 2 for the 5505 aerofoil, and 4 for the 5510 profile. The thickness-to-gap ratio determines whether the tip flow remains separated or reattaches to the aerofoil: for $\tau_{max}/e = 2$ the flow remains separated leading to the formation of the first noise source, for $\tau_{max}/e = 4$, the flow reattaches preventing the formation of the low-velocity region. This aligns with figure 3.19 (a), which shows the absence of the low-velocity region within the gap for the case with $\tau_{max}/e = 4$.

The two cases analysed in this section were selected to show the influence of the thickness-to-gap ratio on the development of the first tip noise source, as they are characterised by similar pressure distribution along the chord, resulting in the same vortex detachment position. Figure 4.7 (a) - (b) have been expanded by considering different aerofoils, obtaining the three plots shown in figure 4.12. In figure (a), the data characterised by $\tau_{max}/e = 2$ follow a proportional trend above the dotted line, but appear sparse below it, as expected, since the first noise source tends to disappear for small angles of attack ($\alpha < 10°$). A similar trend is observed for the cases with $\tau_{max}/e = 3$, shown in (b), with lower values of the maximum strength of the noise source. Almost all data points are found below the dotted line for the cases with $\tau_{max}/e = 4$ in figure (c). Therefore, we can conclude that the first tip noise source can develop when $\tau_{max}/e < 4$ and depending on the location of the vortex, a function of the angle of attack. Unfortunately, $\tau_{max}/e \geq 4$ cannot be considered as a condition that prevents the formation of the first noise source. Furthermore, the tip flow behaviour appears independent of the boundary layer as figures 4.12 (b) and (c) contain cases with and without the tip immersed within the boundary layer. However, a more detailed analysis of the boundary layer will be presented in section 4.4.

Figure 4.13 (a) displays the tip leakage noise obtained for three different configurations with NACA 5512 and 5515, where the gap size was chosen to maintain $\tau_{max}/e = 4$, the

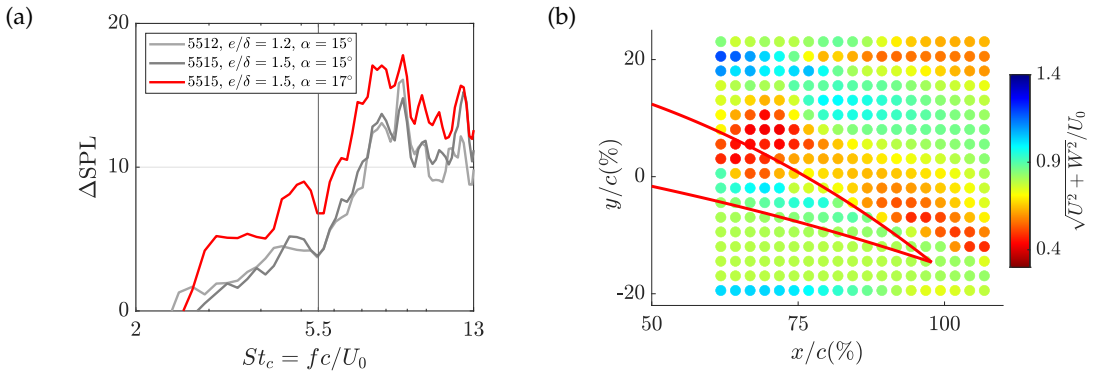

Figure 4.13: (a) Tip leakage noise measured for configurations with $\tau_{max}/e = 4$. (b) Mean velocity field of the resultant velocity in the $x - z$ plane measured within the gap for the configuration with $\tau_{max}/e = 4$, a NACA 5515 aerofoil and $\alpha = 17°$.

identified threshold for the development of the first noise source. At an angle of attack of $\alpha = 15°$, the gray spectral humps nearly collapse within $St_c = 2 - 5.5$, reaching a negligible peak of about 5 dB. However, a slight increase in the angle of attack to 17°, results in the characteristic spectral hump (–). For this configuration with $\tau_{max}/e = 4$ and $\alpha = 17°$, the low-velocity region is found around the 60% of the chord, as shown in figure 4.13 (b), which illustrates the velocity field within the gap. At this position, far from the location with maximum thickness localised at 30% of the chord, the ratio between the local thickness and the gap size assumes values less than 4, for which the tip flow remains separated until the gap exit. In summary, it is not possible to determine in advance whether the first noise source will develop solely based on the ratio $\tau_{max}/e \geq 4$. It is necessary to evaluate the local thickness-to-gap ratio at the location where the tip vortex detaches.

4.3.2 Second tip noise source

The scatter plots of figure 4.8 (a) and (b) suggested a proportionality between the lift coefficient and the strength of the second tip noise source. Specifically, these data points were obtained using the 5510 aerofoil, where the gap size was changed. Figure 4.13 (a) also illustrates the noise increase due to this noise source, within $St_c = 5.5 - 13$, for the configurations with two different aerofoils and two angles of attack, 5512 - 5515 and $\alpha = 15°$ - 17°. Notably, for a fixed τ_{max}/e, the noise source strength is primarily governed by the angle of attack: for the same angle of attack, the two grey lines, corresponding to cases with different aerofoils, collapse well, while as the angle of attack increases the noise levels increase.

This dependency is further explored in figure 4.14, where the strength of the second tip noise source is plotted against the lift coefficient for a variety of aerofoils, ranging from the thinnest 5505 to the thickest 5520. Each scatter plot corresponds to a specific τ_{max}/e ratio, with the gap size adjusted accordingly. For each plot, the data points are

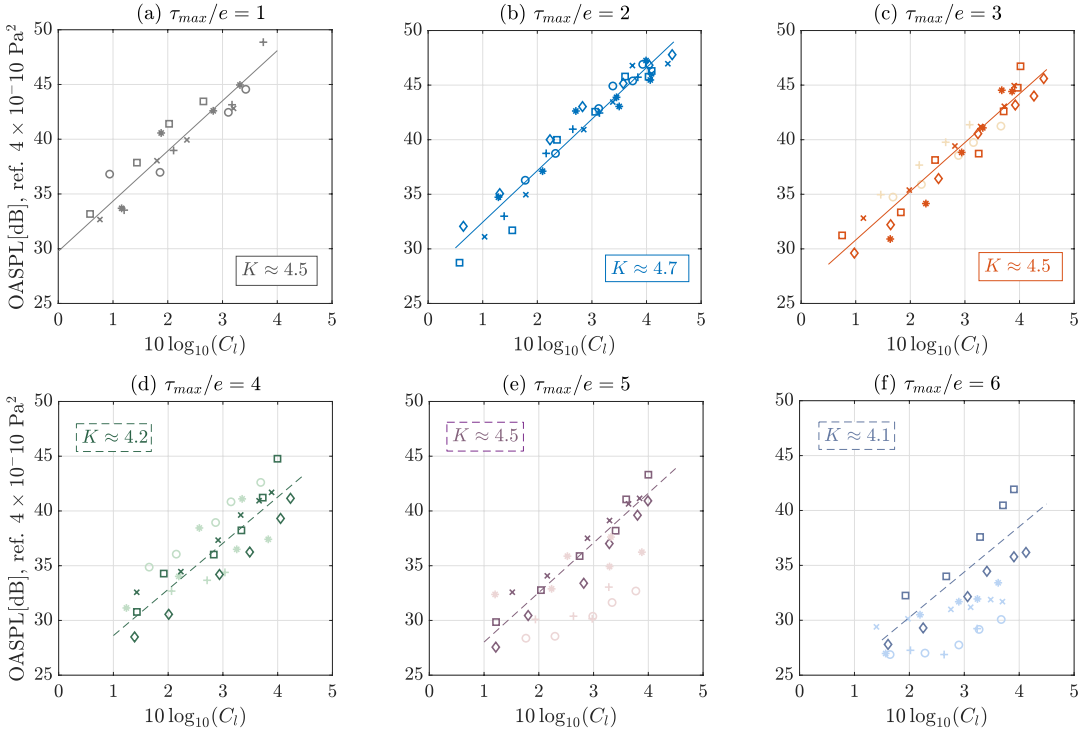

Figure 4.14: Overall Sound Pressure Levels evaluated in the frequency range of the second noise source against the lift coefficient C_l measured for different configurations with $\tau_{max}/e = [1, 6]$. The markers refer to the NACA aerofoils: + 5505, o 5507, * 5510, x 5512, □ 5515, ♢ 5520. Muted colours refer to the configurations with the aerofoil tip immersed in the wall boundary layer, with $e/\delta < 1$.

distributed linearly, increasing with the lift coefficient. An empirical power relationship can be defined as $\overline{p'^2} \propto {C_l}^K$, where $\overline{p'^2}$ is the mean square of the fluctuating pressure linked to the second tip noise source, C_l is the lift coefficient measured at the tip, and K is the slope of the least-squares line superimposed on the scatter plots. The slope K remains almost constant for $\tau_{max}/e = 1$, 2 and 3. For $\tau_{max}/e \geq 4$, the dispersion of the data increases with a consequent decrease in the slope. This effect can be due to the immersion of the aerofoil tip within the boundary layer, rather than a change in the tip flow behaviour associated with the τ/e ratio. By removing all the configurations characterised by $e/\delta < 1$ (muted colours in the figure), the dashed least-square lines present a slope K that aligns closely with that obtained for $\tau_{max}/e < 4$, suggesting a significant role of the boundary layer. Due to the linear relationship between the C_l and the V_L shown in figure 4.9, the power law can be expressed as $\overline{p'^2} \propto {V_L}^{4.5}$, which is close to the V_∞^5 scaling law characteristic of a dipole source close to a sharp edge (Howe, 2002). This suggests that the observed slope may be a consequence of the dipole nature of the second tip noise source. The power relationship is then finalised as $\overline{p'^2} = a{C_l}^{4.5}$, where the coefficient a depends on the thickness-to-gap ratio, decreasing as the τ_{max}/e increase. Ideally, when the thickness-to-gap ratio tends to infinity (with the gap size approaching zero), the tip flow does not enter the gap, thereby preventing

the development of the second noise source.

The second tip noise source develops whenever the tip flow separates at the pressure side edge singularity, regardless of whether the tip flow reattaches to the aerofoil or remains separated until exiting the gap. This behaviour is reflected in the power relationship between the strength of the noise source and the lift coefficient, where the slope remains independent of the thickness-to-gap ratio. The dipole nature of the source dictates the slope value. However, as the thickness-to-gap ratio increases and the aerofoil tip is more immersed in the boundary layer, the noise strength decreases.

The power relationship between the strength of the second tip noise source and the lift coefficient is useful during the design process, as it allows for a qualitative prior estimation of the noise based on the τ_{max}/e ratio and the lift coefficient C_l. The lift coefficient can be obtained by integrating the pressure coefficient C_p at either the midspan or the aerofoil tip. In particular, knowing C_p at the tip enables the prediction of tip leakage vortex detachment location, which, together with the τ_{max}/e ratio provides insight into the development of the first tip noise source. Future studies with different chamber lines are needed to extend the correlations established in this work.

4.4 Effect of the boundary layer e/δ

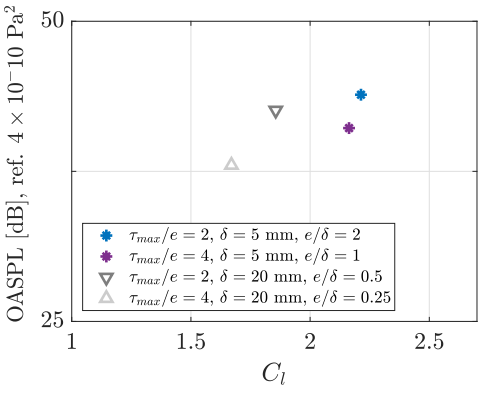

Figure 4.15: Overall Sound Pressure Levels evaluated in the frequency range of the second noise source against the lift coefficient C_l for four configurations with $\tau_{max}/e = 2$, 4 and boundary layer thickness $\delta = 5$ and 20 mm. These configurations are characterised by the same aerofoil 5510 and angle of attack $\alpha = 15°$.

In the previous section, the boundary layer was observed to influence the strength of the second tip noise source. The slope of the least-squares lines in figure 4.14 decreases due to the wider spread of the data for the cases with aerofoil tips immersed within the boundary layer. This effect of the boundary layer was significant for $\tau_{max}/e \geq 4$, as figure 4.14 (c) with $\tau_{max}/e = 3$ includes data obtained with the aerofoil tip immersed

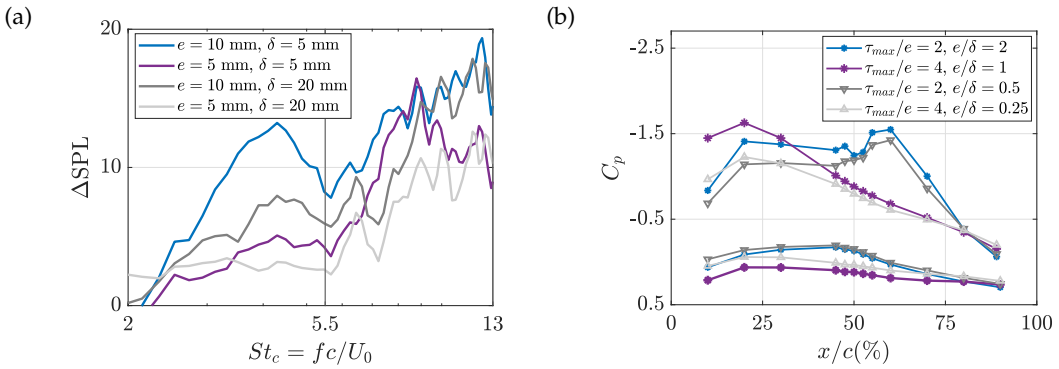

Figure 4.16: (a) Tip leakage noise and (b) pressure distributions C_p along the aerofoil measured for four configurations with $\tau_{max}/e = 2$, 4 and boundary layer thickness $\delta = 5$ and 20 mm. These configurations are characterised by the same aerofoil 5510 and angle of attack $\alpha = 15°$.

in the boundary layer[1] that align well with the overall linear trend. However, for these cases, the boundary layer thickness was set to $\delta = 5$ mm. The two cases previously analysed in detail, with 5510 aerofoil, $\alpha = 15°$, $\tau_{max}/e = 2$ and 4, have been immersed in a thicker boundary layer of $\delta = 20$ mm, both resulting in $e/\delta < 1$. Figure 4.15 shows that the reduction in the strength of the second noise source, when τ_{max}/e increases from 2 to 4, is more pronounced in a thicker boundary layer, i.e. $e/\delta < 1$. This greater reduction can be attributed to the significantly lower tip flow velocity that can be achieved in a thicker boundary layer.

Figure 4.15 also shows a decrease in the lift coefficient as the boundary layer thickness increases, for the configurations with the same τ_{max}/e. This is due to a reduction in the loading on the aerofoil suction side, especially upstream of the midchord, while the pressure coefficient on the pressure side remains almost constant, as illustrated in figure 4.16 (b). Both cases with $\tau_{max}/e = 2$ are characterised by a pressure peak in the pressure distribution at $x/c = 60\%$, with its magnitude slightly reduced for the case with a thicker boundary layer. Due to the link between the magnitude of the pressure peak and the intensity of the first tip noise source, a shallower peak of almost 8 dB is measured, as shown within $St_c = 2 - 5.5$ in figure 4.16 (a) for the case $e/\delta = 0.5$ (–). The other cases, with $\tau_{max}/e = 4$, remain characterised by the absence of the first tip noise source.

4.5 Conclusions

The current investigation has identified three key non-dimensional parameters influencing the tip leakage noise sources, building on the previous chapter that detailed the

[1] NACA 5505 and 5507 with $e/\delta = 0.66$ and 0.92.

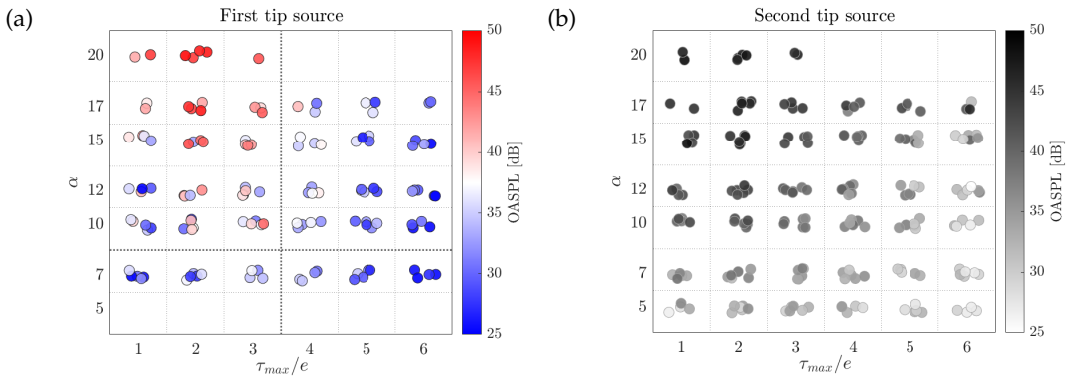

Figure 4.17: Correlation maps illustrating the relationship between the strength of the first (a) and second (b) tip leakage noise sources and the non-dimensional parameters α and τ_{max}/e. The effect of e/δ is less evident. The diverging colormap in figure (a) highlights the conditions under which the first noise source disappears, with blue indicating its absence. The gradient colormap in figure (b) shows how the strength of the second noise source varies, increasing from white to black.

mechanisms involved in the generation of these sources. Specifically, the angle of attack α, the ratio between the maximum aerofoil thickness and the gap size τ_{max}/e, and the ratio between the gap size and the boundary layer thickness e/δ are the parameters that control the two fluid-dynamic instabilities, vortex-shedding and shear layer roll-up, responsible for the two tip leakage noise sources. A wide range of configurations, obtained by varying α, τ_{max} and e have been experimentally analysed through steady and unsteady pressure measurements, as well as hot-wire velocity measurements in a midgap plane and along the aerofoil suction side region. The effect of the boundary layer has been investigated by considering two distinct boundary layer thicknesses.

The correlation map in figure 4.17 (a) illustrates the relationship between the strength of the first noise source and the two non-dimensional parameters, τ_{max}/e and α, highlighting the conditions under which this source disappears. The effect of e/δ on this source is less evident. To ensure an intuitive interpretation, a diverging colormap was used in this map, with blue representing the absence of the noise source and red indicating its presence and increasing strength. This study established that the first tip noise source emerges when the conditions $\tau_{max}/e < 4$ and $\alpha \geq 10°$ are met. In this regime, the tip flow separates at the aerofoil pressure side edge and does not reattach. Specifically, this extended separated flow develops when the tip leakage vortex detaches from the aerofoil surface. The location of this vortex detachment can be identified by the minimum pressure peak observed in the C_p pressure distribution along the aerofoil suction side tip, which varies with α and e. Additionally, the magnitude of this peak, function also of e/δ, is directly related to the strength of the first noise source. Overall, this source tends to disappear for $\alpha < 10°$ and $\tau_{max}/e \geq 4$; however, to confirm this, it is necessary to analyse the local ratio τ/e at the position of the vortex detachment.

The correlation plot, in figure 4.17 (b) with gradient colormap, provides a clear visualisation of how the strength of the second noise source increases with α and its attenuation as τ_{max}/e increases. The second tip noise source is associated with shear layer roll-up, which occurs whenever the tip flow separates at the pressure side edge. This characteristic is reflected in the following scaling law, where slope is independent of the τ_{max}/e: $\overline{p'^2} \propto {C_l}^{4.5}$, with $\overline{p'^2}$ representing the pressure fluctuations associated with the second tip noise source, C_l is the lift coefficient function of the angle of attack, and the exponent 4.5 reflecting the dipole nature of the source. However, the noise strength decreases as the aerofoil tip becomes more immersed in the boundary layer and the thickness-to-gap ratio increases, ideally approaching zero as τ_{max}/e tends to infinity. This study also highlights that, while the lift coefficient C_l remains consistent whether evaluated at midspan or at the tip, the C_p pressure distribution at the tip provides valuable information about the tip flow topology and vortex, and, consequently, about the first tip noise source.

Chapter 5

Tip leakage noise reduction treatments

This chapter investigates treatments to reduce tip leakage noise, focusing on porous material and rounded pressure side tip edges. Both treatments reduce the noise, with porous material slightly outperforming. Reductions for the vortex-shedding noise source are attributed to flow field changes, while for roll-up source, they result from a combination of flow changes and damping properties of porosity. Rounding the pressure side edge reduces both noise sources by altering the flow field.

5.1 Background

Different technologies have been proposed in the literature to reduce the tip leakage noise, focusing either on treating the duct casing over the tip rotor, with Over-Tip-Rotor liners, or on modifying the blade tip itself, using porous treatments. OTR liners have shown substantial noise reduction by attenuating sound and decreasing source strength (Sutliff et al., 2021). Specifically, Palleja-Cabre et al. (2024) investigated the reductions of the tip leakage noise by using OTL, showing that the noise reduction arises from both acoustic back-reaction effects and hydrodynamic modifications of the noise source.

Porous material applied to the leading edge of OGVs has proven effective in reducing broadband interaction noise. Geyer et al. (2011) studied fully porous aerofoils in turbulent flow, showing that the noise reductions generally increase with higher permeability. However, applying porosity across the entire chord resulted in significant

aerodynamic performance penalties. Later, Geyer et al. (2019) suggested three mechanisms of noise reduction: viscous dissipation in the pores, an increased effective aerofoil thickness due to ticker boundary layers and hydrodynamic absorption of the impinging turbulence by the porous surface. The reduction of velocity fluctuations was also suggested to contribute to the trailing edge noise abatement by Carpio et al. (2019). Nonetheless, at very high frequencies, the porous aerofoil generally generated more noise than non-porous material (Geyer et al., 2010).

The use of porous tips to reduce tip leakage noise, including both tip-vortex/stator interaction and fan-tip self noise, was tested computationally using RANS simulations by Khorrami et al. (2002). The investigation showed that the porosity weakened the tip vortex and pushed it away from the edge, suggesting that these changes would reduce the tip noise while having a negligible effect on the aerodynamic performance. Choudhari and Khorrami (2003) performed RANS to investigate porous side-edge treatments for flap noise reduction, identifying two mechanisms behind the effectiveness of porous treatments: changes of the local mean flow due to flow leakage across permeable skin and damping of the pressure fluctuations near the flap. However, as near-field unsteady components were not modeled in either works, the connection between flow modifications and reductions in sound pressure levels could not be confirmed. Angland et al. (2009) experimentally observed the reduction of the near-field pressure fluctuations and flow field changes when applying a porous treatment to a flap side edge. The investigation also assessed the aerodynamic efficiency, which was reduced by 1.1% due to a slight increase in drag.

The concept of drag as a measure of lost performance has been applied to turbomachinery flows from external aerodynamics, as discussed by Denton (1993), who reviewed the loss mechanisms in turbomachines, defying "loss" as any flow features that reduce the efficiency of a turbomachine. Specifically, focusing on tip leakage losses, lift losses always occur at the blade tip, both due to the reduction in blade length and the drop in blade loading towards the tip. Bindon (1989) first found that most of the losses occur when the separation bubble, localised around the pressure side edge, leaves the gap. Successively, Bindon and Morphis (1992) found a way to reduce the losses by rounding the pressure side corner, i.e. removing the separation bubble. However, Heyes et al. (1992) affirmed that the radius of the pressure side tip is vitally important for forming the vena contract and should be kept to a minimum to minimise the tip leakage mass flow, which, in principle, should be the primary attempt of a designer of turbines. Significant reduction of the tip leakage loss could also be achieved by simple changes to the aerofoil design using squealers and winglets (Schabowski and Hodson, 2007).

Rounding the pressure side tip edge was also proposed by Laborde et al. (1997) to avoid the clearance cavitation, which appears within the gap of an axial flow pump due to the low pressure of the separated flow. Guo et al. (2016) numerically compared the flow field and the performance of two hydrofoils, one with a square tip edge and the

other with a rounded tip edge, finding that rounding weakens cavitation within the gap without fully eliminating the separated flow. This reduction is accompanied by a slight lift loss, with the square tip configuration providing a marginally higher lift coefficient than the rounded case. Recently, Bi et al. (2024) numerically investigated the effect on clearance cavitation of a 2 mm thick porous treatment installed at the hydrofoil tip, observing a weakening of both the tip leakage flow velocity and the vortex strength.

5.1.1 Novel contributions of the current chapter

The previous chapters identified two tip leakage noise sources for a single-stationary aerofoil, attributed to two fluid-dynamic instabilties occurring within the tip gap: vortex shedding and shear layer roll-up. These instabilities are connected to the behaviour of the tip flow after it separates at the pressure side tip. Both instabilities occur when the flow remains separated until the gap exit, whereas only roll-up occurs when the flow reattaches to the aerofoil. Flow reattachment does not occur, resulting in the first noise source, when $\tau_{max}/e < 4$ and with the tip vortex far from the aerofoil surface.

This chapter focuses on treatments to reduce tip leakage noise on a NACA 5510 aerofoil with $\tau_{max} = 20$ mm. An experimental investigation is conducted to evaluate the performances of configurations with aerofoil tips treated using porous material or by rounding the pressure side edge, focusing on noise reduction and aerodynamic losses. Both treatments are effective, with the porous treatment showing slightly better performance, in terms of noise reduction and lift losses.

For the first noise source, this study reveals that the achieved noise reduction is independent of the thickness of the porous tip, suggesting that the reduction mechanisms are mainly linked to changes in the flow field. For the second noise source, the reduction is a consequence of both flow changes and the inherent properties of porosity in damping pressure fluctuations, with the reduction being dependent on the thickness of the porous treatment. Notably, significant reductions are achieved even with a 1.6 mm thick treatment. A rounded pressure side edge, which has not been previously explored in the literature as a noise reduction treatment, leads to a reduction of both noise sources by modifying the flow field. However, both treatments result in worse aerodynamic performance compared to the baseline case, with drag loss influenced by τ_{max}/e and α, the same parameters affecting the first tip noise source.

This chapter is organised as follows: noise measurements are used to select the optimal porous and rounded treatment, whose flow fields are then analyzed through hot-wire measurements. Finally, the forces acting on the baseline and modified configurations are measured.

5.2 Porous tip treatment

5.2.1 Noise measurements

In the previous chapters, the tip leakage noise was determined by directly subtracting in decibels the power spectral density obtained from the same configuration, with and without the gap. Here, the noise reduction due to the porous tip, defined as Insertion Loss (IL), is obtained by subtracting the power spectral density for the porous or rounded case from that of the baseline hard wall configuration, for a given gap size:

$$\Delta SPL = 10\log_{10}(S_{pp,baseline}) - 10\log_{10}(S_{pp,porous}) \tag{5.1}$$

Optimum treatment

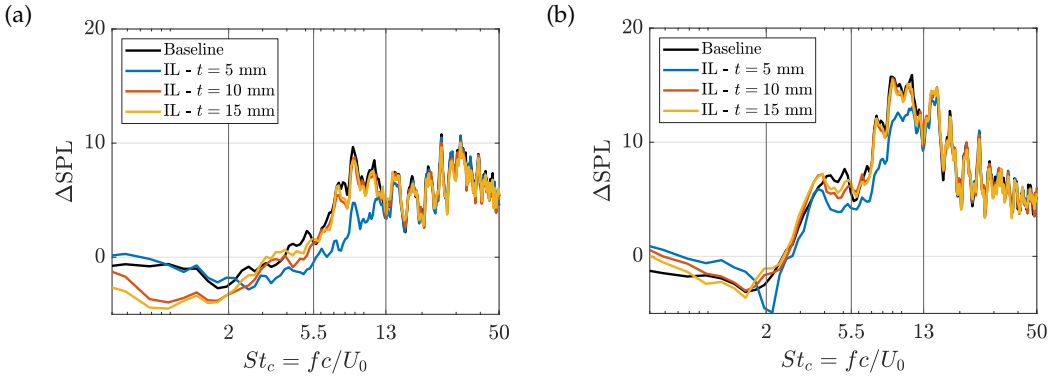

Figure 5.1: Noise reduction spectra obtained for the configurations with porous tips of different spanwise thickness t, compared with the tip leakage noise of the hard wall case. The configurations are characterised by $e = 5$ mm (a) and 10 mm (b), and $\alpha = 15°$.

The effect of the thickness of the porous treatment is analysed by comparing three cases with porous tips of different spanwise thicknesses: $t = 5, 10$ and 15 mm. The noise reductions achieved with these treatments are shown in figure 5.1 (a) and (b), together with the tip leakage noise for the hard wall configurations with gap sizes $e = 5$ and 10 mm, and at angle of attack $\alpha = 15°$. In the non-dimensional frequency range of interest of the two noise sources, $St_c = 2 - 5.5$ and $5.5 - 13$, the tip leakage noise is fully suppressed by applying a treatment of $t \geq 10$ mm, for both tip gap cases. Notably, although the 5 mm thin porous layer shows slightly reduced effectiveness in noise reduction, of less than 3 dB, within the same frequency ranges, its curve collapses with the others in the high-frequency range, i.e. $St_c > 13$. Additionally, it also does not cause additional noise at low frequencies $St_c < 2$, unlike the other two cases.

These promising results for a 5 mm thin porous tip are further investigated by analysing its effectiveness for different angles of attack. Figure 5.2 displays the noise reductions

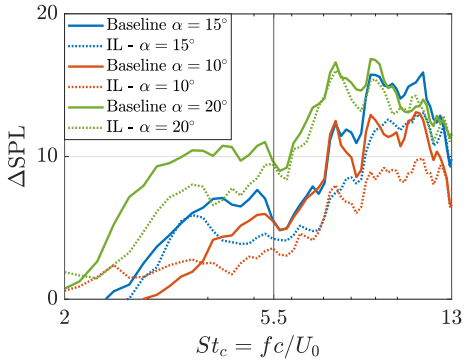

Figure 5.2: Noise reduction spectra obtained for the configurations with porous tip of spanwise thickness $t = 5$ mm, compared with the tip leakage noise of the hard wall case, obtained for three angles of attack and $e = 10$ mm.

obtained for the configuration with three angles of attack $\alpha = 10°$, $15°$ and $20°$, along with the tip noise increases. The noise reductions increase with the angle of attack in the frequency range of the second noise source, reaching near-complete suppression at $\alpha = 20°$. In contrast, reductions in the frequency range of the first source remain incomplete, with a maximum difference of nearly 3 dB. At this stage, we cannot confirm whether the reduction is due to noise attenuation from the porous treatments or the absence of the two fluid-dynamic instabilities responsible for the noise sources.

Location of the treatment

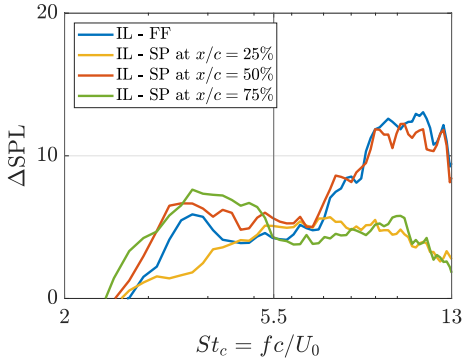

Figure 5.3: Noise reduction spectra measured by the far field microphone and three wall Surface Pressure (SP) probes located on the bottom wall. The configuration with porous tip of spanwise thickness $t = 5$ mm, $e = 10$ mm and $\alpha = 15°$ is analysed.

This section examines the effects of porous treatments in the near field of the aerofoil to identify locations of maximum noise reduction. Figure 5.3 presents the noise reduction measured by the far field microphone, alongside reductions measured by remote probes positioned on the bottom wall at three chordwise locations: $x = 25, 50$ and 75% of the chord. These spectral curves indicate that the strongest reductions occur at the midchord, within both frequency ranges of interest, while the remote probe

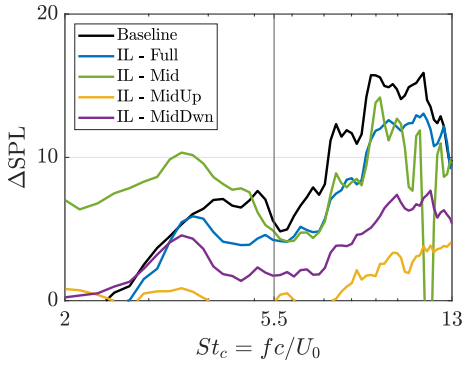

Figure 5.4: Noise reduction spectra obtained for the configuration with porous tip treatment of thickness $t = 5$ mm applied along the entire chord (FULL), between 25 and 75% of the chord (Mid), between 50 and 75% (MidDwn) and between 25% and 50% (MidUp), sketched in figure 5.5. All configurations are characterised by $e = 10$ mm and $\alpha = 15°$.

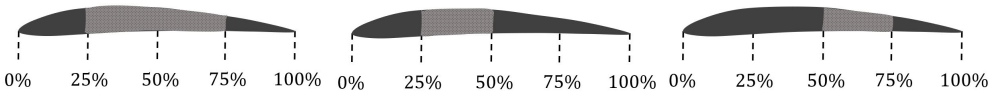

(a) Mid (b) MidUp (c) MidDwn

Figure 5.5: Porous cases tested refined around the midchord.

at 75% of the chord mainly detects the reduction of the first source. The coherence between the pressure signals acquired in the far and near fields, shown in figure 3.3 (b), clarifies these findings. Indeed, this figure indicated that the second noise source is mainly located around the mid-chord, explaining why the greatest noise reductions are measured at this location. The first tip noise source was localised downstream of the midchord, between the 50% and 90% of the chord, which accounts for the reductions observed at both 50% and 75% of the chord.

Based on the previous results, applying porosity specifically in the mid-chord region is expected to reduce the tip noise sources effectively. This approach aims to suppress them while minimizing the treated area, mitigating the potential negative impact on aerodynamic performance. The first configuration tested consists of a porous section extending from the 25% to the 75% of the chord, labelled 'Mid' in figure 5.4 and sketched in figure 5.5 (a). The corresponding noise reduction almost collapses with that achieved with the full porous tip along the aerofoil 'Full', confirming the expectations, except for the higher reduction obtained at low frequencies and the spikes at the end of the range, which may be attributed more to human factors. This configuration was obtained by applying a thin metallic tape to the fully porous tip to render the desired section non-porous. The investigation was extended to include two additional cases, focusing on only the upstream and downstream halves of the midchord section, referred to as 'MidUp' and 'MidDwn', sketched in figure 5.5 (b) and (c). Figure 5.4 shows that the downstream section is slightly more effective than the upstream one, which

may be related to the occurrence of both fluid dynamic instabilities in the hard wall case between the 50% and 75% of the chord.

Further measurements

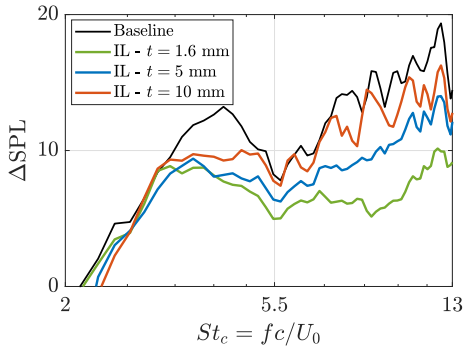

Figure 5.6: Noise reduction spectra obtained for the configurations with porous tips of different spanwise thickness t, compared with the tip leakage noise of the hard wall case analysed in Chapter 3 and 4 with $e = 10$ mm and $\alpha = 15°$.

The measurements presented in this chapter for the hard wall configurations, in terms of tip noise increase, differ slightly from those reported in the previous chapters. The maximum noise associated with the first noise source was measured to be approximately 13 dB in figure 3.1, while in figure 5.1 (b) it is about 8 dB. This discrepancy could be due to the different hard wall configuration, here obtained by covering the entire porous tip with metallic tape, which may influence its impedance, causing it to behave differently than a solid wall.

Figure 5.6 shows the tip noise increase and the reduction obtained by applying different porous treatments on the same aerofoil considered in the previous chapters. Both maximum noise reductions observed with the largest porous treatment, and lower effectiveness of around 3 dB for the $t = 5$ mm modification, confirm the reliability of the previous measurements in figure 5.1 (b). Furthermore, an even thinner treatment of $t = 1.6$ mm has been investigated, leading to the following considerations. Unlike the first noise source, the second one is influenced by the thickness of the porous treatment.

5.2.2 Effect on the tip leakage flow and vortex

To understand the reasons for noise reduction using a porous tip, it is essential to evaluate the flow field in the tip region. Building on the previous considerations about the influence of porous treatment thickness on the second noise source and dependency of this noise source on the tip leakage velocity close to the wall (Chapter 4), the flow field has been evaluated along the aerofoil suction side at the exit of the gap for the configuration with a thickness of $t = 5$ mm to assess the change in the tip velocity. As

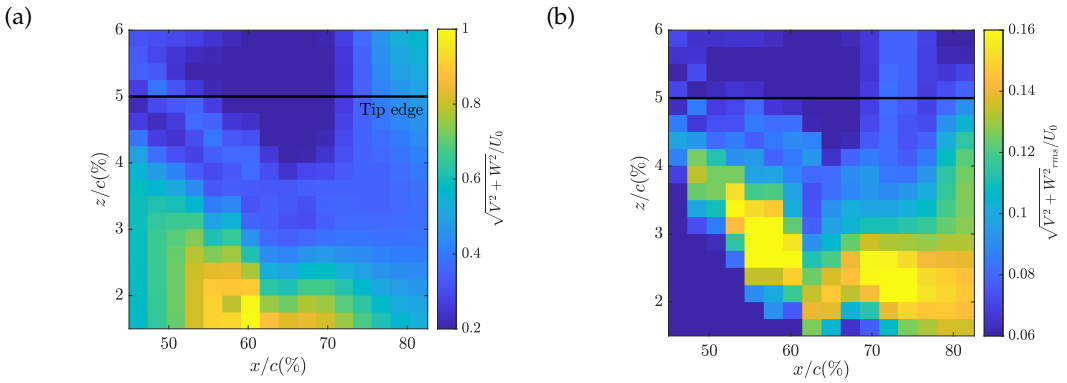

Figure 5.7: Mean (a) and rms (b) velocity field of the resultant velocity in the $y-z$ plane measured along the aerofoil suction side with HWA for the hard wall configuration with $e = 10$ mm and $\alpha = 15°$.

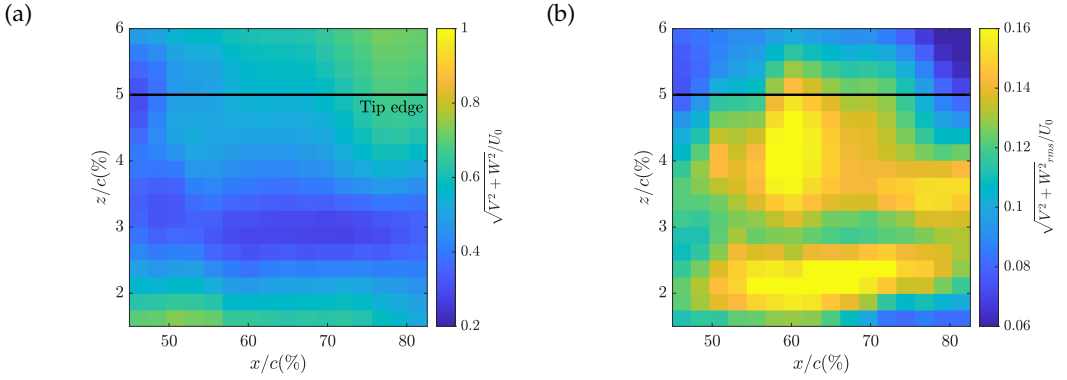

Figure 5.8: Mean (a) and rms (b) velocity fields of the resultant velocity in the $y - z$ plane measured along the aerofoil suction side with HWA for the configuration with porous tip of $t = 5$ mm thickness, $e = 10$ mm and $\alpha = 15°$.

the reduction of the first noise source does not depend on the porous thickness, the flow field within the gap and around the suction side has been investigated for the configuration with $t = 1.6$ mm.

Figure 5.7 (a) shows the mean velocity field obtained with the hot wire for the hard wall configuration along the suction side, similar to that shown in figure 3.12. The separated flow region is identified by low velocity between the 50% and 75% of the chord near the aerofoil tip, along with the resulting high-speed tip leakage flow observed close to the bottom wall. In the region with this velocity gradient, the highest rms values are found, as shown in figure 5.7 (b). The other region of high turbulence observed downstream of the 75% of the chord can be linked to the fluctuations observed in the instantaneous flow field in figure 3.11 (b).

The porous tip has a strong impact on the characteristic features of the flow field. Figure 5.8 show a less intense high-speed jet close to the wall, consistent with observations by Bi et al. (2024). This effect may be due to a reduced pressure difference between both sides of the aerofoil caused by a flow penetration through the porous material (Choudhari and Khorrami, 2003), which can explain the lift losses discussed in section

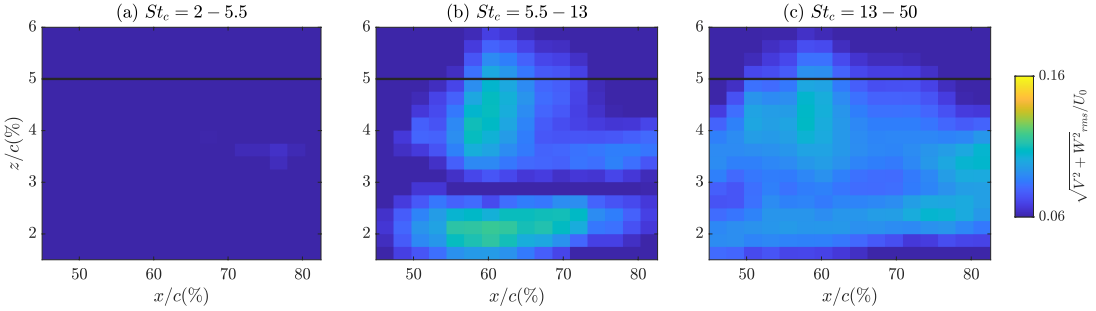

Figure 5.9: Rms velocity fields of the resultant velocity in the $y - z$ plane measured along the aerofoil suction side with HWA bandpass filtered in three frequency ranges, $St_c = 2 - 5.5$ (a), $St_c = 5.5 - 13$ (b) and $St_c = 13 - 50$ (c).

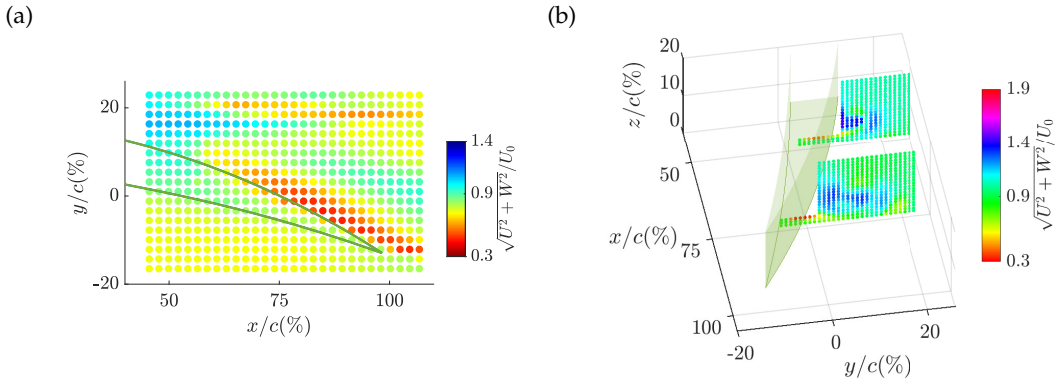

Figure 5.10: Mean velocity fields of the resultant velocity in the $x - z$ plane measured within the gap (a) and in different chord-wise section (b), for the configuration with $t = 1.6$ mm, $e = 10$ mm and $\alpha = 15°$.

5.4. Additionally, the porous material ability to dampen the leakage flow, as suggested by Bi et al. (2024), could contribute to this weaker flow. High turbulence values are still found in the velocity gradient region close to the wall, which contributes to the second noise sources, as shown in figure 5.9 (b). This contour is obtained by filtering the rms of the resultant velocity in the $y - z$ plane of figure 5.8 (b) within the frequency range of the second noise source $St_c = 5.5 - 13$, while figures 5.9 (a) and (c) are obtained by filtering within $St_c = 2 - 5.5$ and $St_c = 13 - 50$, respectively. High turbulence values are also observed near the aerofoil tip, which may result from the porosity itself, contributing to frequencies above $St_c > 5.5$, as shown in (b) and (c). The reduction of the second tip source achieved by using a porous tip can be attributed to the weakening of the tip flow, combined with the noise attenuation properties of the porosity, which dampen pressure fluctuations. Indeed, the reduction increases with the thickness of the treatment.

The independence of the noise reduction of the first noise source from the thickness of the porous treatments suggests that this reduction could be mainly due to changes in the tip flow. Figure 5.10 (a) shows the low-velocity region localised downstream of

the 75% of the chord, associated with the detachment of the vortex that starts downstream of the midchord, as shown in figure (b). The low-velocity region is characterised by higher values compared to that of the hard wall configuration shown in figure 4.4 (b). This 'weaker' separation may lead to a less intense vortex-shedding phenomenon, similarly to the observation made when decreasing the angle of attack in section 4.2.2. Notably, the vortex core is well-identified by the highest velocity values at the midchord near the aerofoil surface, while at 75% of the chord, it appears more spread out and weaker, exhibiting lower velocity values, as also observed by Khorrami et al. (2002) and Bi et al. (2024).

5.3 Rounded tip

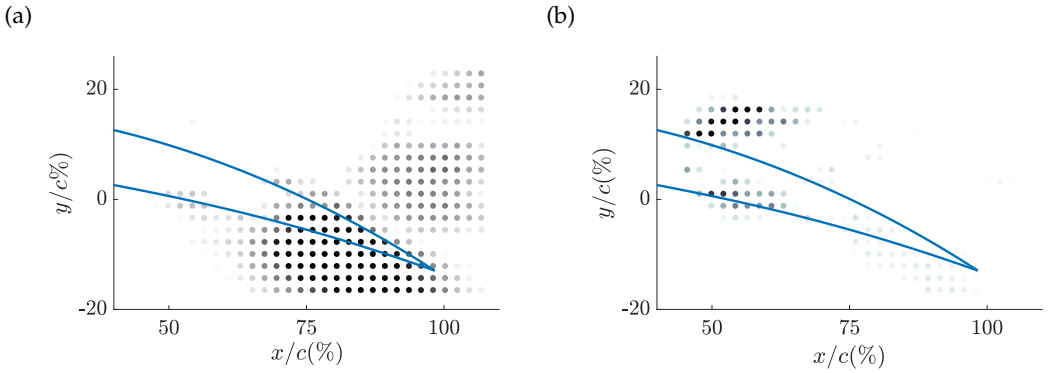

Figure 5.11: Integrated coherence plot between the hot-wire and far field signals over the non-dimensional frequency of the first (a) and second (b) tip noise source. The hot-wire signals are recorded in a midgap plane for the configuration with $e = 10$ mm and $\alpha = 15°$.

In Chapter 3, it was suggested that the two tip leakage noise sources are generated by the scattering at the aerofoil tip of the pressure fluctuations caused by the two fluid-dynamic instabilities, shear layer roll-up and vortex shedding, which arise from the tip flow separation occurring at the pressure side tip edge. Figure 5.11 (a) qualitatively supports this hypothesis, showing high coherence values along the aerofoil pressure side. These values are obtained by integrating the coherence between the hotwire and far-field signals over the frequency range of the first noise source for the hard wall baseline configuration. Figure (b) shows the coherence values obtained for the second tip source, which are mainly distributed along the pressure side edge, although the highest values are found at the midchord in the suction side region. These findings align with the coherence plot presented in figure 3.3 (b), obtained by considering near and far field pressure signals, which locate the first noise source mainly around the 75% of the chord and the second around the midchord. Modifying the pressure side edge will impact the two noise sources by altering the flow field, as shown in the literature, but without affecting the efficiency of the scattering mechanism. The acoustic wavelengths of both

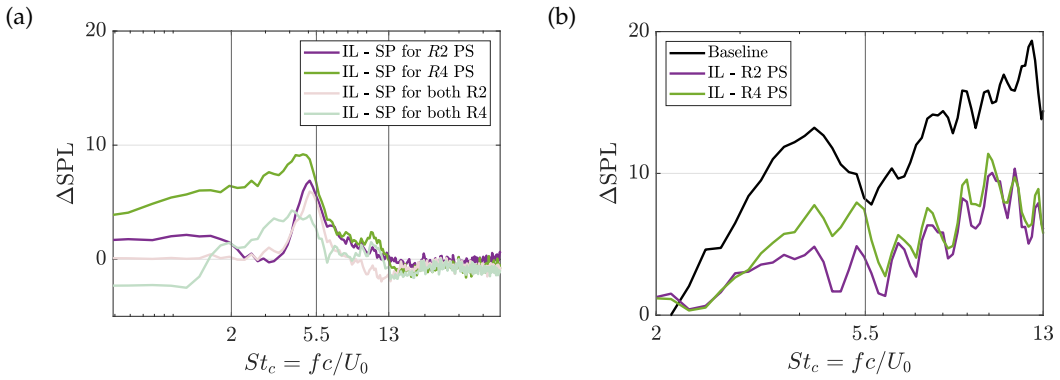

Figure 5.12: Noise reduction spectra, measured by the wall surface pressure probe located on the bottom wall at $x/c = 75\%$ of the chord (a) and by the far field microphone (b), achieved rounding the pressure side 'PS' and/or 'both' sides of the baseline configuration, with $e = 10$ mm and $\alpha = 15°$, for different values of the radius fillet R.

noise sources are significantly larger compared to the modifications investigated, being approximately three orders of magnitude greater for both noise sources.

Figure 5.12 (a) displays the noise reductions measured by the remote probe located on the bottom wall at $x/c = 75\%$ of the chord, achieved by rounding the pressure side tip alone or both pressure and suction side tips of the baseline configuration with different radii. As expected, modifying the pressure side results in a reduction of the first noise source, with greater reductions observed as the fillet radius increases. In contrast, modifying both pressure and suction side edges slightly worsens the performance. The remote microphone does not detect the reduction of the second tip noise source, which is clearly identified by the far field microphone, as shown in figure 5.12 (b). Specifically, this figure shows the reductions of the second noise source, which are similar for the configurations with radii of 2 and 4 mm, while the reduction of the first hump is less pronounced for the smaller radius. These results have guided our subsequent flow field investigations. The configuration with a radius of 4 was experimentally analysed using hot wire, while the other with a smaller modification, was investigated in Chapter 6 using LES simulations, which offer higher resolution than hot wire measurements.

The effect of rounding the aerofoil pressure side on the flow field is shown in figures 5.13 and 5.14. A uniform flow extends along the entire aerofoil suction side, as indicated by the low rms values in figure 5.13 (b), while the low-velocity region, characteristic of a separated flow, is confined near the aerofoil tip, as shown in (a). The velocity of this uniform flow is lower than that of the high-speed jet observed in the baseline configuration, which could explain the reduction of the second tip noise source. The reduction of the first noise source could be attributed to the weaker separation observed in figure 5.14 beyond the aerofoil suction side tip, downstream of the 75% of the chord. In Chapter 6, a detailed analysis of the flow field for the configuration with a rounded pressure

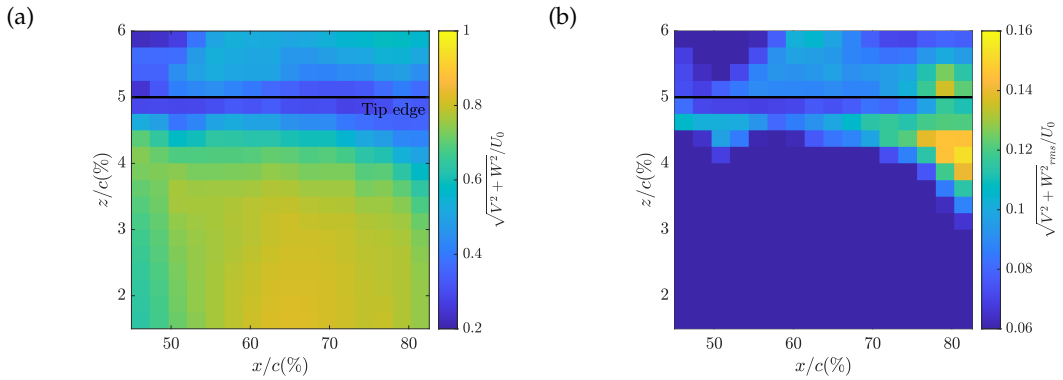

Figure 5.13: Mean (a) and rms (b) velocity field of the resultant velocity in the $y-z$ plane measured along the aerofoil suction side with HWA for the configuration with rounded pressure side tip $R4$, gap size $e = 10$ mm and angle of attack $\alpha = 15°$.

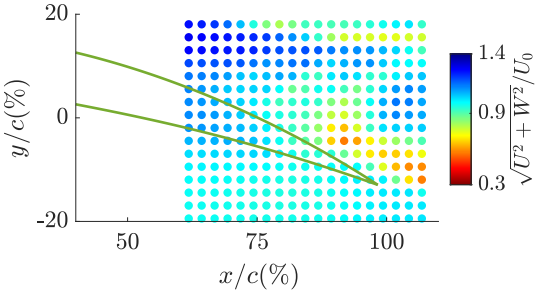

Figure 5.14: Mean velocity fields of the resultant velocity in the $x-z$ plane measured within the gap for the configuration with rounded pressure side tip $R4$, $e = 10$ mm and $\alpha = 15°$.

side edge will be conducted using LES to determine changes in the fluid dynamic instabilities responsible for the two noise sources. This numerical analysis aims to shed new light on the mechanisms behind noise reduction.

5.4 Aerodynamic implications

Modifying the aerofoil tip with porous treatments or rounding the pressure side edge will impact the aerodynamic performance. Before evaluating these modifications, measurements of forces acting on the baseline configuration are acquired. Figure 5.15 displays the lift and drag coefficients, C_L and C_D, as a function of the gap size e for the baseline configuration with a geometric angle of attack $\alpha = 15°$. In these force calculations, the effective angle of attack α_{eff} was considered to account for wind tunnel deflection (details in Appendix A.5). It can be seen that C_L decreases as the gap increases, i.e. τ_{max}/e decreases, consistent with the findings of Higgens et al. (2019) and the considerations of Denton (1993) regarding the drop in lift due to the reduction in the aerofoil span-wise extent. Indeed, as the gap between the aerofoil tip and the casing wall increases, the effective span of the aerofoil decreases. The gap also causes a rise in

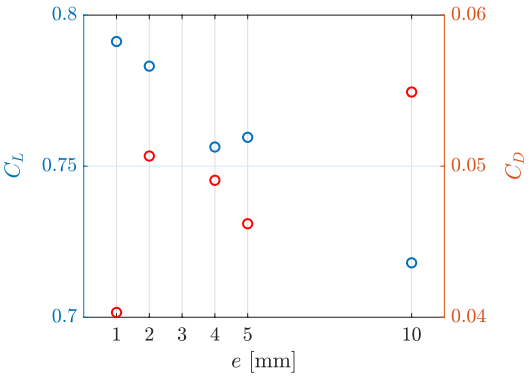

Figure 5.15: Variation of the lift and drag coefficients, C_L and C_D, with the gap size e, considering the hard wall configuration with a geometric angle of attack $\alpha = 15°$.

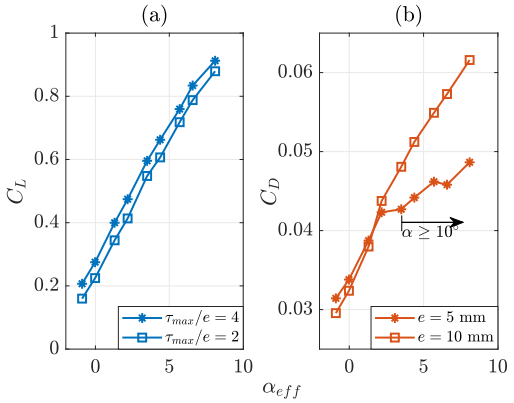

Figure 5.16: Variation of the lift and drag coefficients, C_L in (a) and C_D in (b), with the effective angle of attack α_{eff}, considering the hard wall configurations with $e = 5$ and 10 mm.

drag, with a significant increase when e increases from $e = 5$ to 10 mm, i.e. $\tau_{max}/e = 4$ to 2. As observed in Chapter 4, the first noise source develops when $\tau_{max}/e < 4$, corresponding to a tip flow that does not reattach to the aerofoil surface and remains separated until exiting the gap. Bindon (1989) found that most of the performance loss occurs when the separation bubble is ejected into the gap, corresponding to the tip flow remaining separated. Therefore, this extended separation may contribute to both increased drag and the generation of the first tip noise source.

The development of the first noise source was found to depend on the thickness-to-gap ratio and the geometric angle of attack, as shown in figure 4.7 (a) and (b). This noise source was not observed when $\tau_{max}/e < 4$ and $\alpha < 10°$, or when $\tau_{max}/e \geq 4$ regardless of α. This behaviour helps explain the trend of the drag coefficients plotted against α_{eff} in figure 5.16 (b), measured for two gap sizes $e = 5$ and 10 mm, i.e. $\tau_{max}/e = 4$ to 2. The drag coefficients remain similar at small angles of attack but begin to diverge at a certain α_{eff}, which corresponds to $\alpha = 10°$, the point at which the first noise source develops for $\tau_{max}/e = 2$. At higher angles of attack, the drag produced in the case with

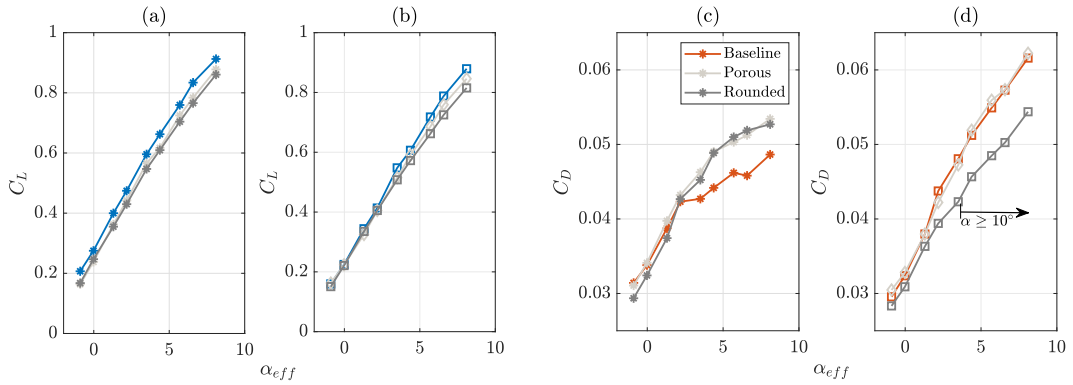

Figure 5.17: Variation of the lift and drag coefficients, C_L and C_D, with the effective angle of attack α_{eff}, considering the hard wall, porous and rounded tip with $R4$ PS, for $e = 5$ mm (*) and 10 mm (□).

$\tau_{max}/e = 2$ is higher than that of the small gap. The lift forces, shown in figure 5.16 (a), follow a linear trend with the effective angle of attack, with slightly higher values for the smaller gap, as expected from figure 5.15.

The link between the presence of the first tip noise source and increased drag may help to interpret the drag curves obtained for the porous and rounded cases, shown in figure 5.17 (d) for $e = 10$ mm. The drag coefficient for both cases follows that of the baseline until the point where the first noise source develops, identified with $\alpha = 10°$. Beyond this angle, the curve for the rounded case diverges, with drag values lower than those of the other two cases. This result can be explained by considering that for the rounded tip the first noise source is reduced. The porous treatment also leads to similar noise reduction, which would result in a lower drag. However, this drag reduction could be offset by increased skin friction caused by the porosity, as observed in the literature (Geyer et al., 2011), leading to drag values similar to those of the baseline case. For the cases with $e = 5$ mm shown in figure (c), there is no drag increase due to the absence of extended separated flow. Therefore, the increase in drag of the porous case can be attributed solely to skin friction. The drag increase of the rounded case remains not fully understood.

The lift curves for the porous and rounded case also follow a linear trend with the effective angle of attack, as shown in figure 5.17 (a) and (b). Specifically, for $\alpha = 15°$, the reduction of C_L is 4.5% for the porous case, which remains constant for the two gap sizes. On the contrary, the C_L reduction for the rounded case, also observed by Guo et al. (2016), changes from 7.3% to 7.8% passing from $e = 5$ to $e = 10$ mm. Both lift losses could be explained by a reduction of the effective blade length: for the porous case, this is due to the flow penetration through the porous material, while for the rounded case, it results from the surface reduction due to the rounding itself.

5.5 Conclusions

The current chapter has examined the reduction of the tip leakage noise by using porous and rounded aerofoil tips, as well as the associated aerodynamic performance losses with these treatments. Although both treatments are effective, the porous tip shows greater noise reduction and less lift loss compared to the rounded tip. Near and far-field pressure measurements were initially used to select the optimal treatment. Subsequently, hot-wire measurements were conducted to investigate the changes in the corresponding flow field, aiding in the understanding of the mechanisms behind the noise reduction. Finally, a load cell was used to measure the forces acting on the configurations.

The porous treatments have different effects on the two tip leakage noise sources. The reduction for the first noise source is mainly due to flow changes, as it is not dependent on the thickness of the porous treatments. For the second noise source, the reduction is a consequence of both flow changes and the properties of porous material in damping the pressure fluctuations. The second noise source is almost suppressed for a $t = 10$ mm, while a reduction of almost 10 dB is achieved with the smallest treatment of 1.6 mm. Additionally, the flow penetration through the porous treatment reduces the pressure difference between both sides, weakening the extended separation and the flow near the wall responsible for both noise sources, while increasing the turbulence within the gap. To minimize the impact on aerodynamic performance, it has been shown that a small porous treatment localised in the mid-chord region can achieve the same noise reduction as a treatment applied across the full chord.

Noise reductions similar to those achieved by the porous treatment are also obtained when rounding the pressure side tip edge of the aerofoil. Modifying this geometric singularity leads to reductions in both noise sources by modifying the flow field. Specifically, the configuration with a radius of 4 mm generates a higher reduction of the first noise source compared to that with 2 mm radius, while reductions in the second noise source are similar, with a maximum reduction of 10 dB. The flow field of the configuration with the best performances was investigated with hotwire, revealing a reduction in the extent of the separated flow at the exit of the gap and detecting a uniform-slower flow near the bottom wall. However, the experiments alone were not sufficient to fully identify the mechanisms behind this noise reduction, which will be investigated in detail in Chapter 6 using LES to analyse the configuration with 2 mm radius tip.

The aerodynamic forces acting on the aerofoil were evaluated for the different configurations by varying the angle of attack and the gap size. The lift curve exhibits a linear trend with the angle of attack, unlike the drag, which is influenced by the behaviour of the tip flow, depending not only on the angle of attack but also on the thickness-to-gap ratio, as discussed in Chapter 4. In the presence of the extended separated flow, which is responsible for the first tip noise source, higher drag losses are measured for

the baseline configuration. The reduction of the first noise source for both treatments would also result in a reduction of drag losses, which is observed only for the rounded case. The porous treatment, on the other hand, is characterised by higher skin friction, leading to drag losses similar to those of the baseline configuration.

Chapter 6

Tip leakage noise source mechanisms: numerical investigation

This chapter numerically investigates the generating mechanisms of the tip leakage noise sources and their changes when the aerofoil pressure side tip is rounded. LES simulations confirm that vortex shedding and shear layer roll-up are responsible for the tip noise sources in the baseline configuration. For the rounded tip, both instabilities persist but with reduced intensity.

6.1 Background

One of the earliest schematics of the flow topology within the tip gap area was developed by Kang and Hirsch (1993) using ink-trace flow visualizations on a linear compressor cascade. This study identified three main vortex structures: tip leakage vortex, which originates downstream of the aerofoil leading edge and increases in size along the chord; tip separation vortex, aligned along the pressure side tip and converging towards the suction side around the trailing edge; and a secondary vortex, with an opposite rotation sense to the TLV but whose generation mechanism was unclear.

The position of the TLV matched with a trough of pressure measured on the bottom wall in the aerofoil suction side region by Storer and Cumpsty (1991). They also conducted numerical studies on the same set-up using the Reynolds-Averaged Navier-Stokes (RANS) approach, which showed satisfactory predictions of the tip flow in terms of static pressure field. Subsequently, Inoue et al. (1998) observed changes in the flow topology with a moving wall. The relative motion of the endwall intensified the tip leakage vortex but reduced the tip leakage losses. Although RANS simulations are

currently employed to predict the flow path within turbomachinery, their applicability remains limited due to the unsteady nature of the tip leakage flow.

You et al. (2007) used LES to investigate a linear cascade with a moving end-wall, analysed experimentally by Wang and Devenport (2004). They observed the dominant TLV, in the suction side region, and the TSV underneath the blade tip, which originates at the pressure side tip edge and becomes dominant after the mid-chord. Small induced vortices, defined as Tip Counter-Rotating Vortex (TCRV), were found close to the TLV but decay continuously. More recently, Koch et al. (2022) and Becherucci et al. (2022) performed LES on a linear cascade with a stationary and moving wall, respectively. The wall motion affects the two vortical structures responsible for the tip-leakage noise, TLV and TSV. The TLV is flattened and entrained towards the adjacent blade pressure side. Dynamic Mode Decomposition (DMD) showed that the noise source linked to the TSV moves from the 75% of the chord to the 50% in the case of the moving wall.

To focus on the tip leakage noise, Grilliat et al. (2007) developed an experimental set-up based on an isolated non-rotating aerofoil, highlighting the two tip noise sources at the non-dimensional frequency $St_c = fc/U_0 = 4$ and 10. The first noise source was probably due to the TSV, while the second source was linked to small turbulent eddies generated by the flow separation at the suction side tip and convected by the tip gap flow (Jacob et al., 2010).

Several numerical simulations were performed on the same set-up using different methodologies: zonal approach with LES in the tip region by Boudet et al. (2016), Lattice Boltzmann Method (LBM) by Mann et al. (2016) and LES by Koch et al. (2021). The results of these simulations were in good agreement with the experiments of Jacob et al. (2010), especially in terms of flow topology and pressure fluctuations. Boudet et al. (2016) computed the far-field spectra, achieving a good agreement in the non-dimensional range of frequency $St_c = 2$ - 20. This range corresponds to the tip noise, as background noise and trailing edge noise were not included in the simulation. Indeed, LES were performed only in the tip region. Mann et al. (2016) localised the major part of the noise sources downstream of the aerofoil. It was found that the tip leakage flow generates "coherent vortices that break-up interacting with the aerofoil wake". This break-up was considered the noise-generating mechanism. Koch et al. (2021) obtained the far-field noise spectra through the Ffowcs Williams and Hawkings (FW-H) analogy that radiates the pressure fluctuations from the aerofoil surface to the far field. The aerofoil tip was decomposed into three zones: leading edge from $x/c = 0$ to 25%, mid-chord from $x/c = 25\%$ to 75%, and trailing edge between $x/c = 75\%$ to 100%. In the non-dimensional frequency range $St_c = 8 - 20$, the maximum noise levels were reached at the mid-chord, suggesting that this noise results from the interaction between turbulent structures generated around the mid-chord and the suction side tip edge.

RANS and LES were performed by Decaix et al. (2015) to analyse the tip flow topology around a symmetrical NACA foil. Two tip clearance sizes were investigated. For the smallest gap size, the TSV barely develops under the blade, while for the large gap size, the Q-criterion showed the TSV wrapping around the TLV until the two vortex structures merged near the trailing edge.

6.1.1 Novel contributions of the current chapter

In the previous chapters, the two tip leakage noise sources detected in the far field pressure spectra, at the non-dimensional frequency $St_c = fc/U_0 = 4$ and 10, were attributed to fluid dynamic instabilities occurring within the gap: vortex-shedding and shear layer roll-up. Both instabilities were linked to the behaviour of the tip flow after it separates at the pressure side tip entering the gap. When the flow does not reattach to the aerofoil, both instabilities occur; if reattachment takes place, only roll-up is observed. The flow behaviour depends on the position of the TLV, with reattachment unlikely when the TLV is positioned far from the aerofoil surface. In the baseline configuration, this vortex detachment was observed downstream of the midchord. Additionally, rounding the pressure side corner with a radius of 2 mm results in a noise reduction of nearly 5 dB at both frequencies of the two tip noise sources. However, the mechanisms behind the noise reduction were unclear.

This chapter investigates numerically the flow within the tip gap in the cross sections, at midchord and 75% of the chord. The primary aim is to provide a novel and definitive overview of the flow topology in two sections where the tip flow behavior changes, by clearly identifying the two fluid dynamic instabilities responsible for the tip noise sources through LES, which overcomes the resolution limitations of experimental techniques in this confined region. The same analysis is successively applied to the configuration with a round pressure side tip, revealing that the reduction of the first noise source is attributed to a lower intensity of the vortex shedding, whereas the reduction of the second source is also linked to modifications in the flow field. Specifically, the shear layer roll-up does not occur at midchord and appears with reduced intensity at 75% of the chord.

The current chapter is organized as follows: it begins with details about the numerical set-up and schemes employed to achieve converged solutions. Then, the flow field is investigated in detail, first for the square tip configuration and subsequently for the round tip case.

6.2 Numerical Set-up

The numerical set-up mimics the experiment set-up described in Section 2.1, with a single-stationary aerofoil located in the potential core of an open jet wind tunnel between two walls. A substantial difference between the experimental and numerical set-up is the distance between these two plates, which in the numerical configuration is set to 110 mm, compared to 150 mm in the experimental set-up, to reduce the computational cost. Yet, Koch (2021) showed that this change had a negligible effect on both the loading at the aerofoil midspan[1] and the tip flow. The inflow velocity in the numerical simulation was set to $U_0 = 70$ m/s, slightly higher if compared to 40 m/s of the experimental analysis. However, as shown in Chapter 3, tip leakage noise is a Strohual-dependent phenomenon. All other settings were kept the same, with the angle of attack $\alpha = 15°$, gas size $e = 10$ mm and NACA 5510 aerofoil with a chord length $c = 200$ mm.

6.2.1 Numerical procedure

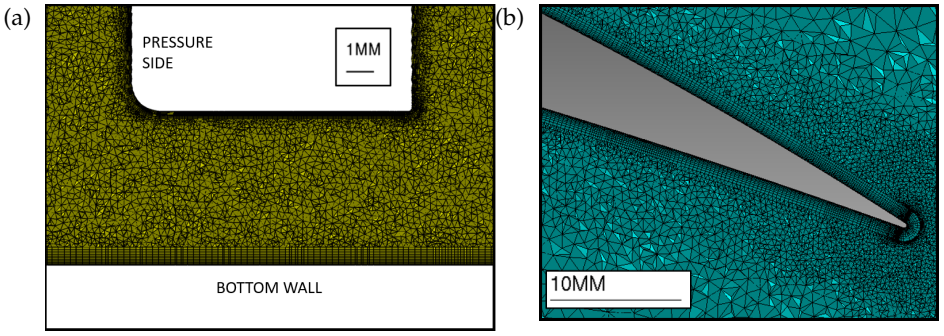

Figure 6.1: Detail of the mesh at the mid-chord cross-section (a) and at midspan near the trailing edge (b) of aerofoil with round tip.

In this chapter, two aerofoils were analysed: one with a square tip and the other with a round pressure side, obtained by modifying the tip with a fillet radius of 2 mm, both experimentally investigated in the previous chapters. The numerical settings used to analyse the aerofoil with a round tip are similar to those used for the square tip configuration, as detailed in Koch (2021). The computational domain measures $17.5c \times 20c \times 10.5c$. It includes the wind tunnel nozzle and the side plates described above. The unstructured mesh consists of 151×10^6 cells, with refinements around the aerofoil and in the tip gap zone, the jet-mixing layers, the potential core, and the wake. Details of the mesh at the mid-chord cross-section and midspan are shown in figure 6.1 (a) and (b). Both aerofoil and bottom plate are meshed with 10 and 11 prismatic layers, respectively, with a stretching ratio of 1.2 and 1.1. The dimensionless wall distance y^+

[1] Figure A.8 compares the pressure distributions obtained at the midspan with this experimental investigation and LES investigation.

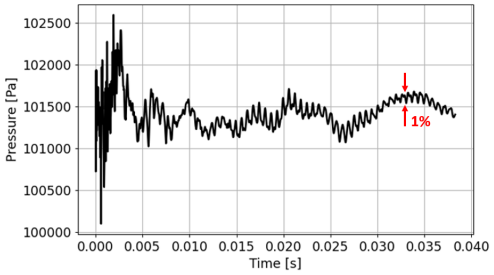

Figure 6.2: Pressure signal recorded on the pressure side tip at the mid-chord.

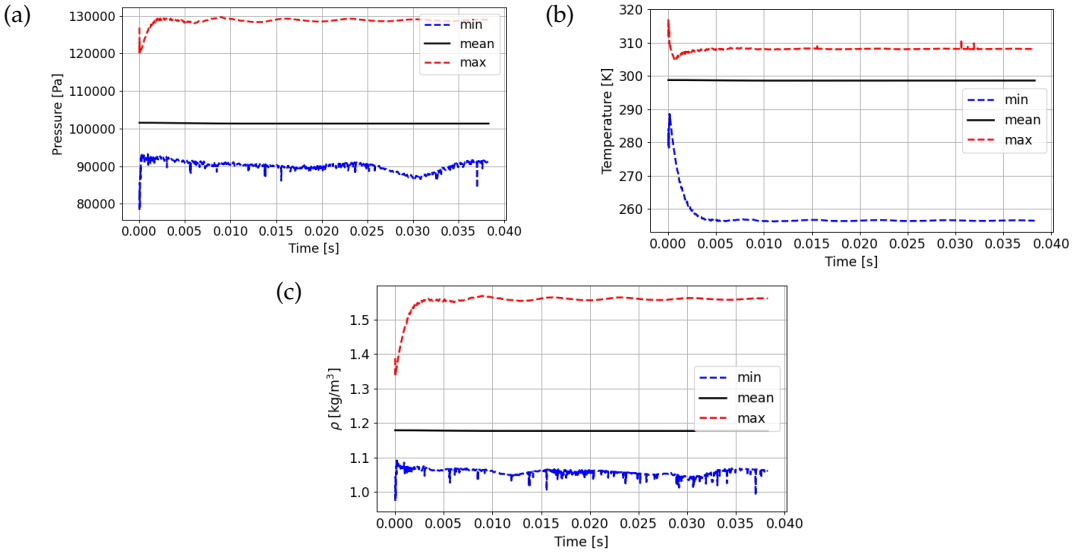

Figure 6.3: Minimum (–), mean (–), and max (–) of static pressure (a), temperature (b) and density (c) signals over the entire domain.

is less than 1 for most cells on the bottom plate in the proximity of the aerofoil, while on the airfoil itself, the wall resolution is within the range of $x^+ < 40$, $y^+ < 3$ and $z^+ < 40$. The y^+ values meets the criterion for a wall-resolved LES (Sagaut, 2006). The walls are modelled as no-slip adiabatic walls, while Navier-Stokes characteristic non-reflective boundary conditions are applied at the inlet and the outlet, combined with sponge layers to prevent potential acoustic wave reflections (Odier et al., 2019).

A compressible RANS calculation, using the $k-\omega$ shear-stress transport to model the turbulence, was performed with ANSYS CFX solver on a coarser version of the mesh to initialise the LES. Compressible LES are performed using the solver AVBP (Schønfeld and Rudgyard, 1999). This solver solves the unsteady Navier-Stokes equations, modelling only the smallest scales of turbulence. For a given quantity f, the filter quantity $\tilde{f}$ is solved, while $f' = f - \tilde{f}$ represents the subgrid-scale quantity, which is modelled using wall-adapting local eddy-viscosity model (Nicoud and Ducros, 1999), ensuring a proper turbulence decay at the walls.

The time step is fixed at 1.0×10^{-8} s to ensure a Courant-Friedrichs-Lewy (CFL) number of 0.7 across the entire domain for stability. Artificial viscosity is added to ensure

the stability of the scheme, using the model of Colin (2000), which only acts in regions where a certain level of error is detected. The flow was established for 12 flowthrough times based on the chord, which corresponds to 0.035 sec, using the explicit single-step Lax-Wendroff (LW) numerical scheme (Lax and Wendroff, 1960). The end of the transient period was determined using a method based on local quantities (Mockett et al., 2010). Probes located in the jet mixing layer, in the wake and on the aerofoil were used to assess the local convergence. Figure 6.2 shows the pressure signal recorded on the aerofoil pressure side at mid-chord, with variations on the order of 1% relative to the mean value. Figure 6.3 displays the evolution of the mean, maximum and minimum values of static pressure (a), temperature (b) and density (c). The minimum and maximum values are calculated at each time step in the entire numerical domain, while the mean value is computed by taking a volume-weighted average across the entire computational domain. At the end of the transient period, LESs were performed with the higher-order explicit two-step Taylor-Galerkin (TT4GA) scheme (Donea, 1984) to obtain mean quantities. However, to collect a significant number of LES snapshots, the LW numerical scheme was used for both square and rounded tips, which is faster being second-order accurate in both space and time compared to the TT4GA scheme, which is third-order accurate in space and fourth-order accurate in time.

6.2.2 Pressure-velocity correlations

A procedure similar to the one proposed in Section 2.2.4 is applied to identify the flow structures involved in noise generation. Here, the covariance between velocity and pressure is calculated as specified in the following expression:

$$\mathrm{Cov}_{(u,p)}(\mathbf{x},\mathbf{P}) = \frac{1}{N-1}\sum_{n=1}^{N} u'(\mathbf{x},t_n)p'(\mathbf{P},t_n+\tau_n) \tag{6.1}$$

where u' are the velocity fluctuations measured at each point of the $2D$-section $\mathbf{x}$ at discrete snapshot t_n, whereas p' are the pressure fluctuations measured in a specific point P, as well as N is the total number of LES snapshots. This point P is localised near the tip of the aerofoil suction side, with its y-coordinate varying as it moves downstream, precisely at $(y/c, z/c) = (-2.9\%, 0)$ for the mid-chord section and at $(y/c, z/c) = (-12.4\%, 0)$ for the $x/c = 75\%$ section.

6.3 Square tip

6.3.1 Noise source identification

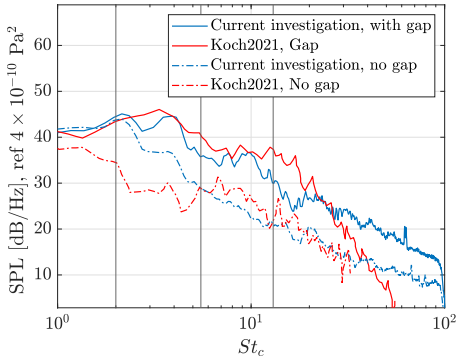

Figure 6.4: Comparison of the sound pressure levels spectra between the current experimental investigation and LESs (Koch et al., 2021), with and without the gap.

This section analyses the far-field and wall-pressure fluctuations. In figure 6.4, the far-field noise spectra measured experimentally are compared with those obtained with the LES (Koch et al., 2021). In both analyses, the observer is located at $\theta = 90°$ in the suction side area of the aerofoil. These noise measurements are obtained by considering the cases with and without the gap to highlight the effect of the tip gap on the far-field. The abscissa is the chord-based Strouhal number $St_c = fc/U_0$, as the experiments were conducted at $U_0 = 40$ m/s, whereas the LES at $U_0 = 70$ m/s. The spectra with tip gap show good agreement, confirming the tip leakage noise as a Strouhal-dependent phenomenon, especially within the two non-dimensional frequencies of the two noise sources, i.e. $St_c = 2 - 5.5$ and $5.5 - 13$. However, the numerical spectrum for the case without the gap is lower than the experimental one, likely due to the absence of side plates in the simulation without the gap. This suggests that additional spurious noise sources, such as jet noise contamination (Koch et al., 2021), were present in the experiment.

The location of the two noise sources was highlighted in Chapter 3 by correlating the far-field signals, acquired by a microphone located at $\theta = -90°$, with the surface pressure spectra measured along the pressure side of the aerofoil. The high coherence values localised the first tip noise source around 75% of the chord and the second around the midchord. These locations were later confirmed by applying a porosity treatment between the 25% and 75% of the chord, which provided the same noise reduction as a porous treatment applied along the entire chord. A similar decomposition was used in the numerical simulations by Koch et al. (2021) to highlight the acoustic results obtained by each zone, with the highest noise levels achieved in the midchord region within $St_c = 8 - 20$. The leading edge and trailing edge regions showed lower noise

levels. The strong agreement between experimental and numerical pressure measurements provides confidence in the reliability of the subsequent results.

6.3.2 Tip flow topology

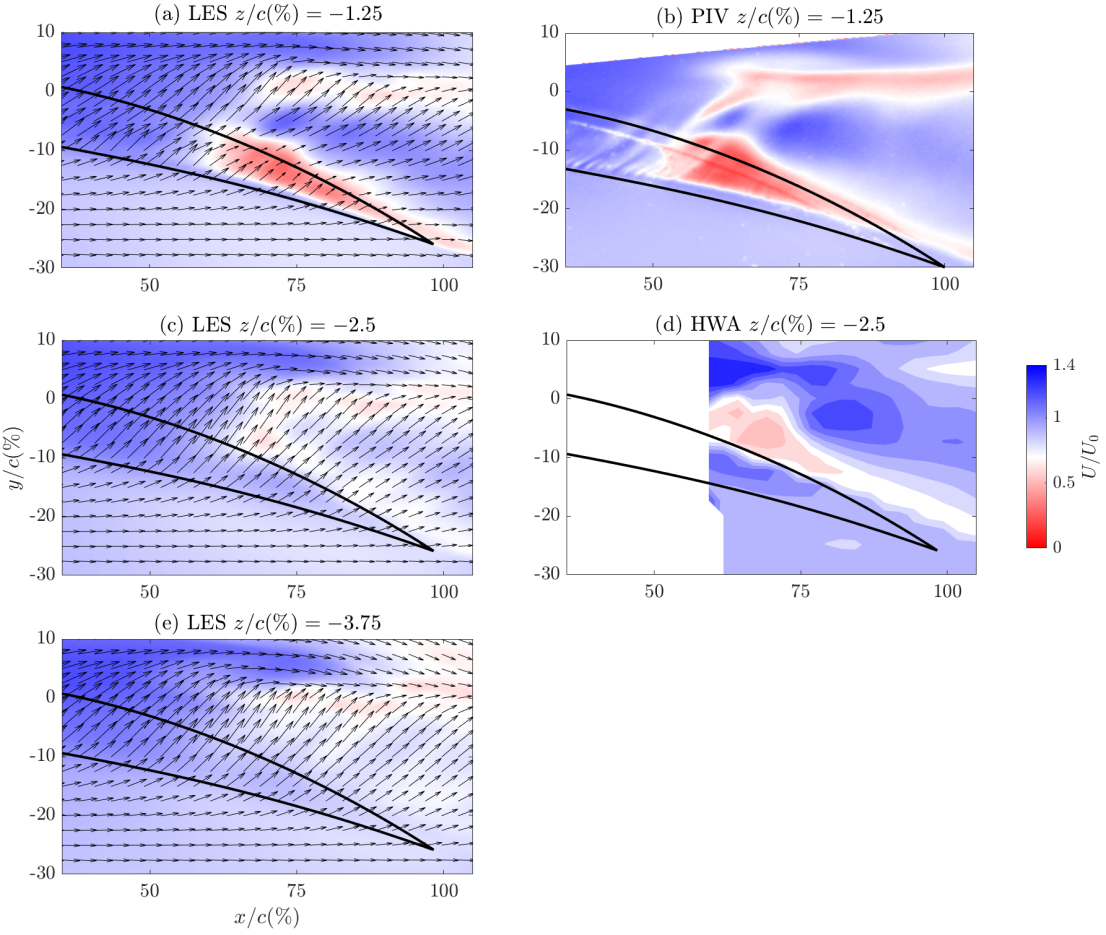

Figure 6.5: Mean fields of the stream-wise velocity component U/U_0 obtained in different planes within the gap with LES (with velocity vectors in the x and y direction), PIV and HWA, for the square tip configuration.

In the previous chapters, the tip flow topology was hypothesised by combining planar measurements within the gap, parallel to the bottom wall, with span-wise measurements outside the gap along the aerofoil suction side and in the suction side region. The flow separates all along the pressure side of the aerofoil, reattaching to the aerofoil tip upstream of the mid-chord but remaining separated downstream of that station, with this behaviour depending on the relative position of the tip leakage vortex and the aerofoil surface. The extended separated flow, identified with an axial velocity U/U_0 deficit, was linked to the first noise source. The second noise source is attributed to a shear layer roll-up that develops along the aerofoil. Using LES, a clearer picture of the tip flow topology within the gap can be provided.

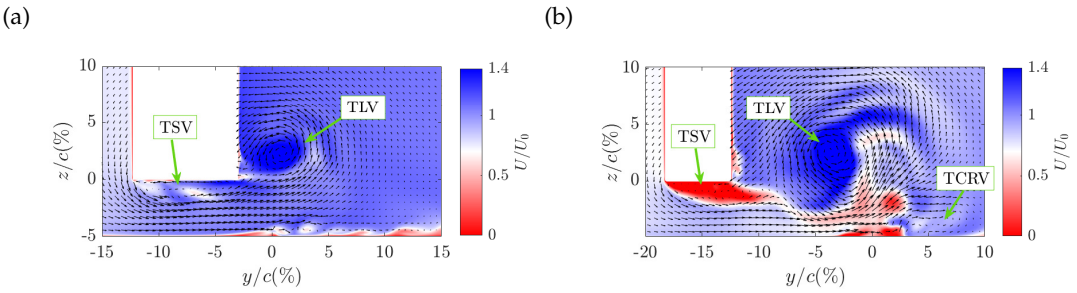

Figure 6.6: Instantaneous contours of the axial velocity component U/U_0 obtained with LES for the aerofoil with the square tip at two different cross-sections: $x/c = 50\%$ (a) and $x/c = 75\%$ (b), with velocity vectors in the y and z direction.

Mean stream-wise velocity contours U/U_0 in different z-planes obtained with LES, PIV and HWA are shown in figure 6.5. Two regions of axial velocity deficit are observed in the plane at $z/c(\%) = -1.5$ close to the aerofoil tip, downstream of the midchord, as shown in figure (a). Specifically, the low-velocity region along the aerofoil suction side is linked to the extended separated flow responsible for the first noise source, while the second one in the suction side region was not investigated in previous chapters. Moving from a midgap plane to one closer to the wall, figures (c) and (e), the low-velocity region along the aerofoil gradually disappears, while the other region maintains constant velocity values. It is evident from the comparison of figures (a) and (b) the good agreement between LES and PIV, and similarly, figures (c) and (d) show good agreement between LES and HWA. However, the hot wire do not capture the additional velocity deficit far from the aerofoil suction side, likely due to its intrusive nature, in contrast to the non-intrusive PIV technique.

The interpretation of the tip flow is completed by analysing two sections of the aerofoil at $x/c = 50\%$ and 75%. Figure 6.6 (a) and (b) show the instantaneous contours of the U/U_0 component at these two locations, respectively. The superimposed velocity vectors help to identify the vortical structures described in the literature (Kang and Hirsch, 1993; You et al., 2007). The TLV is observed in the suction side region, slightly above the aerofoil tip, close to the aerofoil surface at midchord and away from it at $x/c = 75\%$. The TSV is localised below the tip and is formed due to the separation of the flow at the aerofoil pressure side. This separation has not been well documented due to the limited resolution of the experimental techniques in such small gaps. Finally, the TCRV rotates opposite to the TLV and may be induced by the same TLV, which drags the wall boundary layer. This likely explains why the TCRV is more pronounced at the 75% of the chord, where the TLV is stronger.

A variation in the axial velocity is observed below the aerofoil tip when moving from the midchord to 75% of the chord. In both stations, the velocity vectors indicate the presence of a separated flow. However, this flow reattaches before leaving the gap at the midchord, while it remains separated downstream at $x/c = 75\%$. The axial velocity

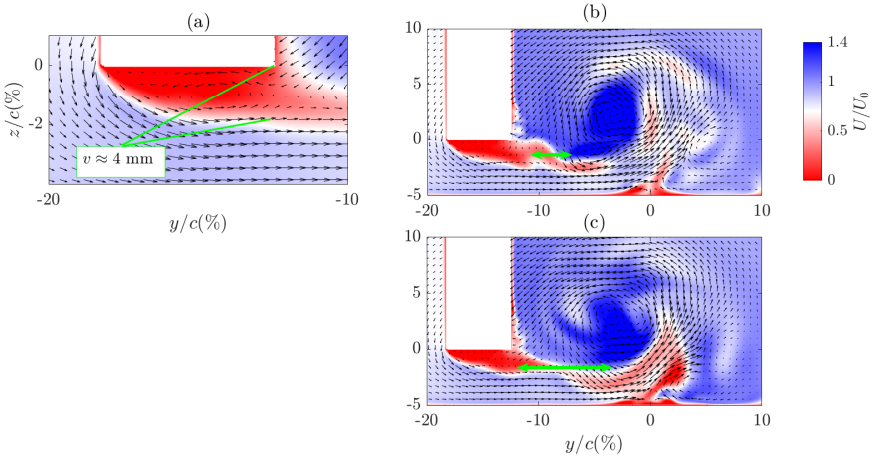

Figure 6.7: Mean field of the axial velocity component U/U_0 obtained with LES at $x/c = 75\%$ cross-section (a). Consecutive instantaneous flow fields (b), (c) and (d), obtained every 5000 time steps.

changes from a non-zero value to zero between the two locations. Upstream of the midchord, the flow enters the clearance in a quasi-normal direction to the aerofoil pressure side, as shown in figure 6.5 (a), (c) and (e), and it separates maintaining its direction. This means that an axial velocity is measured in the localised separated region, when considering a cross-section in the $y - z$ plane as in figure 6.7 (a). Downstream of the midchord, figure 6.7 (b), the separated flow does not reattach to the aerofoil, and no axial velocity is measured. This phenomenon coincides with the merging of the TSV and the TLV into one vortex close to the trailing edge (Decaix et al., 2015) once the TSV exits the tip gap (Koch et al., 2021).

The axial velocity deficit observed along the aerofoil suction side, in figure 6.5 (a), corresponds to the extended separated flow identified below the aerofoil tip in figure 6.6 (b). As the height of cutting z-planes within the gap decreases, this low-velocity region is no longer detected. Specifically, it reaches its maximum extension at the gap exit, qualitatively estimated to be 4 mm, as shown in the mean flow in figure 6.7 (a), confirming our experimental hot-wire measurements in figure 3.12. Notably, the non-dimensional frequency of the first noise source is dependent on this length v, i.e. $St_v = fv/U_0 \approx 0.07$. This relationship remains valid in this case, with the first noise source observed at a frequency of $f = 1.4$ kHz and an inflow velocity of $U_0 = 70$ m/s.

The other axial velocity deficit observed in the suction side region coincides with the red spot observed in figure 6.6 (b), around $y/c(\%) = 0$. This spot likely corresponds to the TSV shed in the suction side region, which successively wraps around the TLV, as evidenced by the consecutive LES snapshots in figure 6.7 (b) and (c). This shedding phenomenon and the subsequent wrapping of the TSV around the TLV, clearly visualised in the following section 6.3.3, can be interpreted as evidence of the aforementioned merging process observed by Koch et al. (2021).

6.3.3 SPOD, DMD and Covariance analysis

Focus midchord section with SPOD

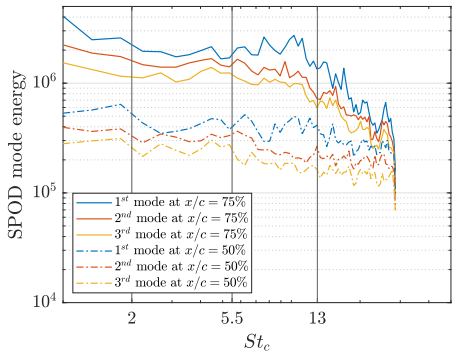

Figure 6.8: SPOD mode energy spectra of the first three modes obtained for the two sections of the square case: $x/c = 50\%$ (continuous lines) and $x/c = 75\%$ (dashed lines).

Spectral Proper Orthogonal Decomposition was conducted on the two sections at midchord and 75% of the chord. The key distinction between SPOD and "standard" POD is that SPOD describes modal shape in both space and time at a specific frequency (Towne et al., 2018). Therefore, SPOD seems more appropriate as our goal is to extract the coherent structures at the frequencies of interest of the two noise sources, i.e. $St_c = 4$ and 10. Key aspects of the flow field can already be derived by analysing the SPOD energy spectra, which are shown in figure 6.8 for the first three modes of the two sections, $x/c = 50\%$ and 75%. The spectra estimation parameters are listed in table 6.1. A database of $N_s = 2046$ consecutive LES snapshots was considered for both sections, obtained by saving every 5000 time step. A number of $N_{ftt} = 128$ snapshots per block with a 50% overlap $N_{ovlp} = 64$ has been chosen, resulting in $N_{blk} = 30$ blocks. These settings lead to smoother spectra, from which it is possible to more clearly distinguish the spectral peaks of interest compared to those obtained with an increased N_{ftt}, as shown in Appendix B.1.

The SPOD energy spectra of the midchord section exhibit lower energy levels compared to those of the other section at $x/c = 75\%$. This discrepancy is likely attributed to the more chaotic flow field at $x/c = 75\%$, marked by a larger TLV, which dominates the flow field. However, the largest separation between the eigenvalues associated with

Database				SPOD parameters		
Case	Variables	N_s	F_s	N_{ftt}	N_{ovlp}	N_{blk}
$x/c = 50\%$ - 75%	u, v, w	2046	20 kHz	128	64	30

Table 6.1: Parameters of the two databases and spectral estimation parameters of the SPOD analysis.

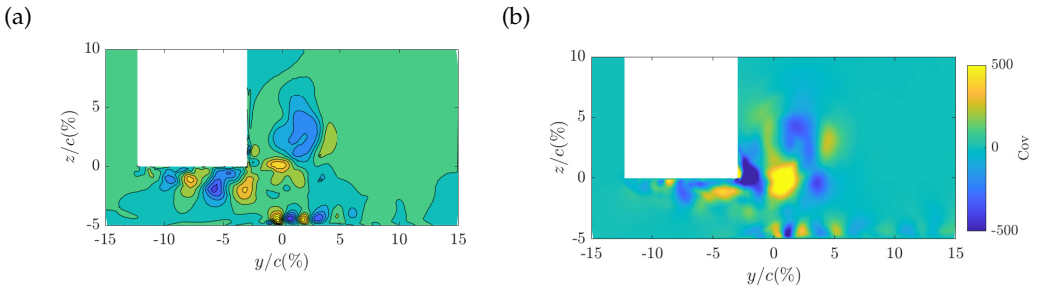

Figure 6.9: Square tip: (a) First SPOD mode of the $x/c = 50\%$ case at the frequency of the second noise source, $St_c = 10$. (b) Covariance plot obtained by relating the velocity fluctuations in the z-direction with the pressure signal filtered in the frequency range of the second noise source, $St_c = 5.5 - 13$.

the first and the second modes is found for the midchord section within the frequency of the second noise source, $St_c = 5.5 - 13$. This means a dominant flow mechanism associated with the leading mode is likely to be observed in that section. The leading mode is shown in figure 6.9 (a) for the non-dimensional frequency $St_c = 10$. The flow field is characterised by a pattern of coherent structures that increase in size from the pressure side to the suction side, resembling the shear layer roll-up. This observation validates the hypothesis presented in Chapter 3 that the roll-up is responsible for the second tip noise source. These coherent structures are localised below the aerofoil tip, aligning with the localised separated flow observed in the instantaneous field in figure 6.6 (a).

The SPOD of the midchord section reveals a shear layer roll-up. To qualitatively prove that this roll-up phenomenon contributes to the second noise source, the covariance procedure outlined in section 2.2.4 is applied. In this case, the procedure consists of correlating the pressure fluctuations measured at the specific point near the aerofoil suction side tip with velocity fluctuations evaluated at every point of the $2D$ section. The covariance contour, shown in figure 6.9 (b), presents a similar pattern to that observed in the leading mode of figure (a). This similarity suggests that the leading mode, which is solely associated with the flow field and not directly linked to pressure fluctuations, is responsible for the second noise source. This inference is supported by the band-pass filtering applied to the pressure fluctuations within the frequency range of this noise source. Without applying any band-pass filtering on the pressure fluctuations, the covariance plot shows large structures near the aerofoil suction side, corresponding to the TLV. Appendix B.2 contains the covariance plots obtained by relating the velocity fluctuations evaluated in three directions, x, y and z, with the unfiltered and filtered pressure signals in the frequency range of the second noise source.

Focus $x/c = 75\%$ section with SPOD and DMD

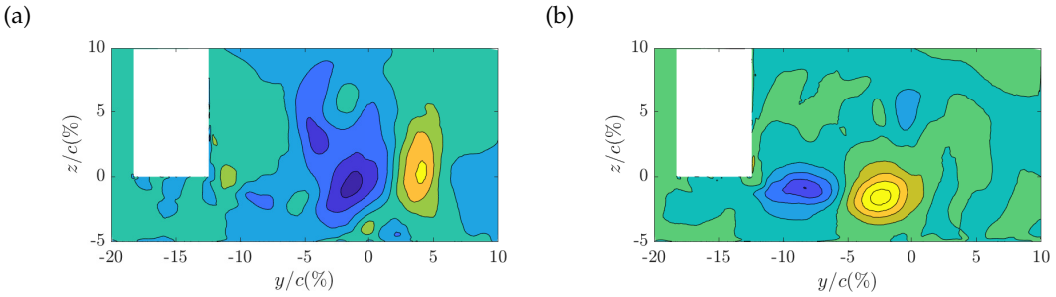

Figure 6.10: Square tip: First SPOD mode of the $x/c = 75\%$ case at the frequencies of the first and second noise sources, $St_c = 4$ (a) and $St_c = 10$ (b).

Focusing on the SPOD energy spectra of the section at $x/c = 75\%$ in figure 6.8, a significant distance between the leading and second modes is also observed within the frequency range of the second noise source, particularly at $St_c = 10$. However, this gap tends to diminish at the frequency of the first noise source, at $St_c = 4$. The leading mode at these two frequencies is shown in figure 6.10 (a) and (b), respectively:

- At $St_c = 10$, the mode in figure 6.10 (b) is characterised by two coherent structures extending into the suction side region, unlike the mode in figure 6.9 (a) at midchord, where the pattern of structures is localised below the aerofoil tip increasing from the pressure to the suction side. The covariance plots shown in Chapter 3 help interpret these modes. The vortical structures are generated between the 50% and 60% of the chord, figure 3.10, and spread out in the aerofoil suction side, figure 3.9 (a). As a result, the mode in figure 6.10 (b) reflects the downstream evolution of the pattern of structures initially observed in figure 6.9 (a).

- At $St_c = 4$, the mode in figure 6.10 (a) exhibits two coherent structures localised between $y/c(\%) = -5$ and 5, coinciding with the region where the TLV appears in the instantaneous flow field. The TLV may mask the vortex-shedding mechanism associated with $St_c = 4$, as shown in the following section. Indeed, the TLV dominates the suction side region with high vorticity and pressure trough (Storer and Cumpsty, 1991). This is consistent with the small separation between the leading and second modes observed in the energy spectra.

Dynamic Mode Decomposition (Schmid, 2010) was performed on the section at 75% of the chord to isolate the vortex-shedding phenomenon associated with $St_c = 4$. DMD is well suited to extract dynamic structures related to a particular frequency (Taira et al., 2017), as each DMD mode represents one of the possible ways in which the coherent structures of the SPOD modes behave at that frequency (Towne et al., 2018). Applying

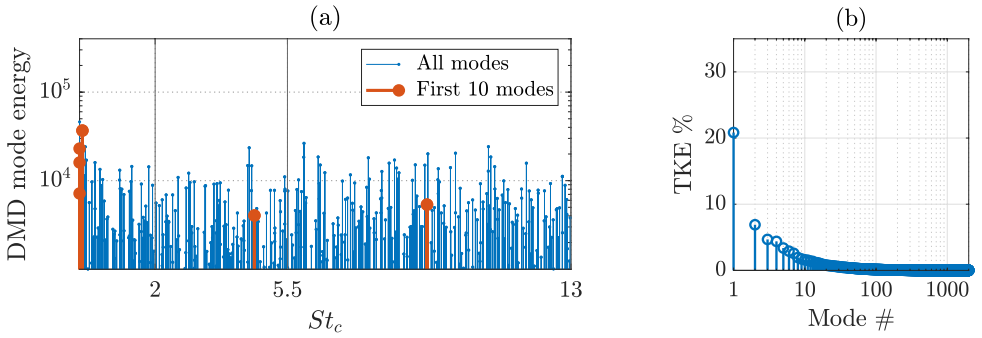

Figure 6.11: Square tip: (a) Amplitude spectra of all DMD modes (–) and of the first 10 modes (–). (b) Total Kinetic Energy from each mode.

DMD to the same database of $N_s = 2046$ consecutive snapshots, recorded with a $F_s = 20$ kHz, yields the spectrum shown in figure 6.11 (a), which reports the frequency and amplitude of all modes. Several modes with the highest amplitude are found around the frequency of the first noise source, $St_c = 4$, while in the range of the second noise source, between $St_c = 5.5$ and 13, no dominant mode clearly stands out from the others. If we truncate by considering only the first 10 modes, which account for approximately 50% of the total energy of the system as shown in figure 6.11 (b), two modes (–) fall within the frequency range of the first and second noise source in figure 6.11 (a).

These two DMD modes, detected in figure 6.11 (a), are animated in figure 6.12 (a) and (b) by showing five different time instants spaced over one period of the corresponding non-dimensional frequencies $St_c = 4$ and 10, respectively. Figure 6.12 (b) shows the movement of the coherent structures in the suction side region, which were also identified with SPOD in figure 6.10 (b). This similarity between the DMD and SPOD modes supports the reliability of the other DMD mode of figure 6.12 (a), which clearly shows a vortex-shedding mechanism not directly observable through SPOD alone. From the aerofoil tip, the coherent structures are successively shed and wrap around the TLV, confirming the earlier observations made from the instantaneous flow field in figure 6.7.

The covariance plots in figure 6.13 (a) and (b) are obtained by band-pass filtering the pressure fluctuations, measured at a point close to the tip, in the frequency ranges of the first and second noise source, $St_c = 2 - 5.5$ and $5.5 - 13$. Although these plots appear quite similar, the highest values are found close to the aerofoil tip where the coherent structures identified in figure 6.12 at $St_c = 4$ (a) and 10 (b) are also located. When no filtering is applied to the pressure signals, the covariance becomes dominated by large structures in the TLV region, as shown in Appendix B.3. This section aims to quantify the covariance levels for comparison with those obtained in the rounded case. Additionally, the Appendix B contains covariance plots obtained by considering the pressure fluctuations measured at different points in the suction side region, near and far from the tip. These plots illustrate why a point near the blade tip was chosen for

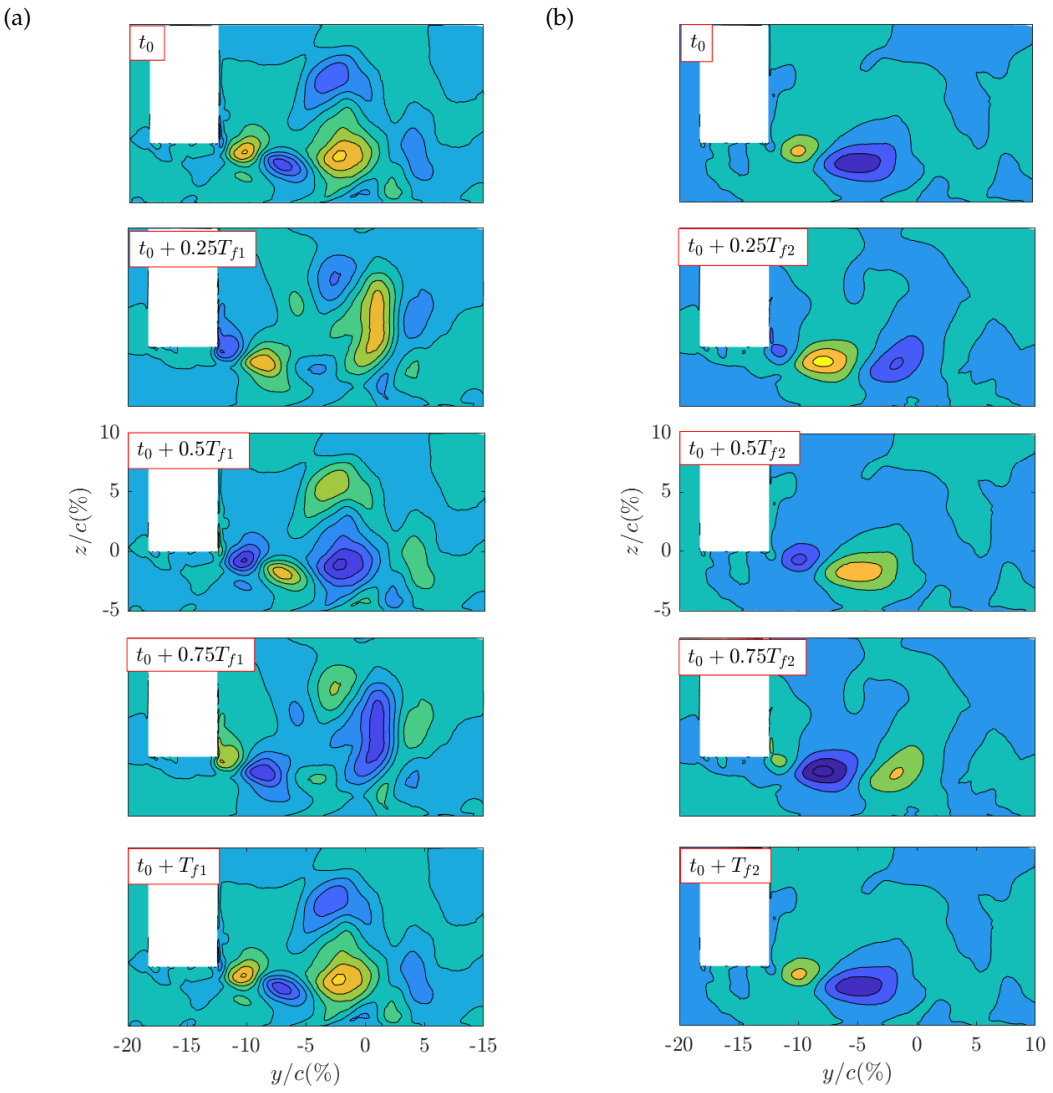

Figure 6.12: Square tip: Animation of the two DMD modes of the $x/c = 75\%$ section at the frequencies of the first and second noise source, $St_c = 4$ (a) and $St_c = 10$ (b). T_{f1} defines the period corresponding to the frequency of the first noise source, while T_{f2} refers to the second.

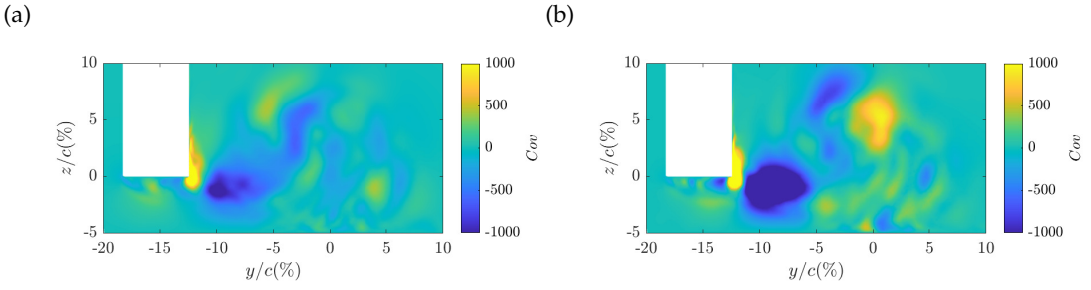

Figure 6.13: Square tip: Covariance plot obtained by relating the velocity fluctuations in the z-direction with the pressure signal filtered in the frequency range of the first noise source, $St_c = 2 - 5.5$ (a), and second noise source, $St_c = 5.5 - 13$ (b).

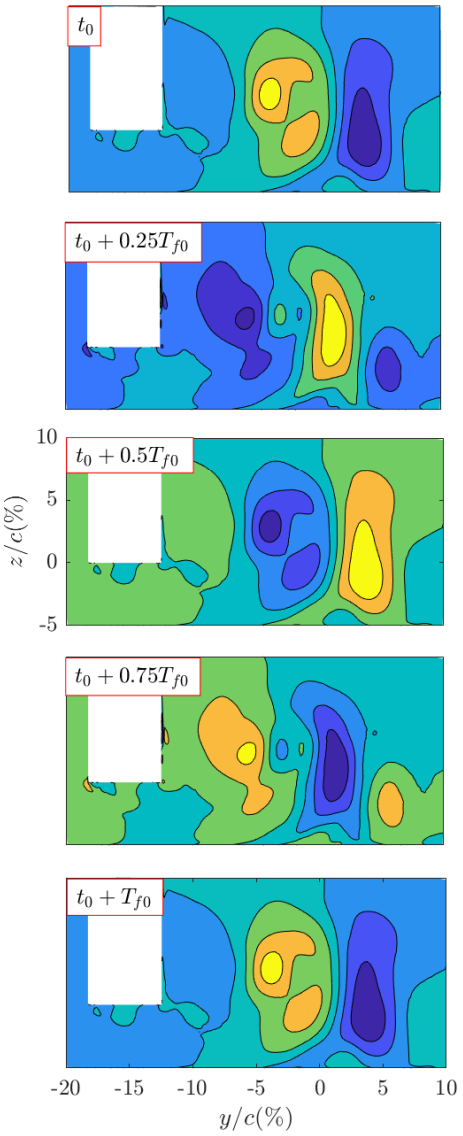

Figure 6.14: Square tip: Animation of the fundamental DMD mode of the $x/c = 75\%$ section at the non-dimensional frequency $St_c = 0.07$, with T_{f0} defining the period corresponding to this frequency.

covariance analysis, as it exhibits significantly higher values due to its proximity to the tip, where scattering is likely to occur.

Among the first 10 DMD modes, the fundamental mode with the largest amplitude appears at approximately $St_c = 0.07$ in figure 6.11, and its animation is displayed in figure 6.14. The animation reveals an oscillation of the TLV, whose core was located between $y/c(\%) = -5$ and 5 in the instantaneous flow field in figure 6.6 (b). This confirms the suggestion by Jacob et al. (2016a) that such motion may be responsible for a broad peak in the velocity spectra detected between $St_c = 0.08 - 0.28$ in the vortex core downstream of the aerofoil trailing edge. Furthermore, the similarity between this

DMD mode and the SPOD mode shown in figure 6.10 (a) suggests that the vortex-shedding mechanism is not visible in the SPOD mode because it is likely masked by the dominant TLV oscillation.

6.4 Round Tip

The two tip noise sources have been linked to the tip flow separation occurring at the pressure side tip. Rounding this corner with a radius of 2 mm results in a reduction of almost 5 dB at both frequencies of the noise sources. As suggested in Chapter 5, this noise reduction can be attributed to changes in the flow field. The flow field investigated experimentally for a case with a radius of 4 was found to be uniform, with an axial velocity deficit observed beyond the aerofoil suction side tip, as shown in figure 5.13 (a) and 5.14 respectively. A similar analysis to the one conducted for the configuration with square tip is performed on the configuration with a 2 mm radius to investigate how the flow instabilities, responsible for the tip noise sources and linked to the tip flow, change.

6.4.1 Tip flow topology

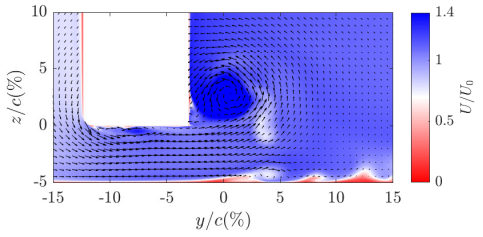

Figure 6.15: Instantaneous contours of the axial velocity component U/U_0 obtained with LES for the aerofoil with the round tip at the midchord section.

Figures 6.15 show the instantaneous contour of the axial velocity component U/U_0 at midchord. The superimposed velocity vectors show that the flow still separates at the entrance of the aerofoil tip, but its extent is significantly limited, which could result in the absence of the shear layer roll-up. At the gap exit, a uniform flow is observed, consistent with experimental findings.

The flow field at $x/c = 75\%$ section is also characterised by a slightly smaller separated flow, with a size of approximately 3 mm at the gap exit, as seen in the mean flow in figure 6.16 (a). However, the other vortical structures, such as TCRV and TLV, appear unaffected by the rounding modification, as shown in the instantaneous field in (b) and (c). The TCRV, observed close to the bottom wall, appears even stronger. The

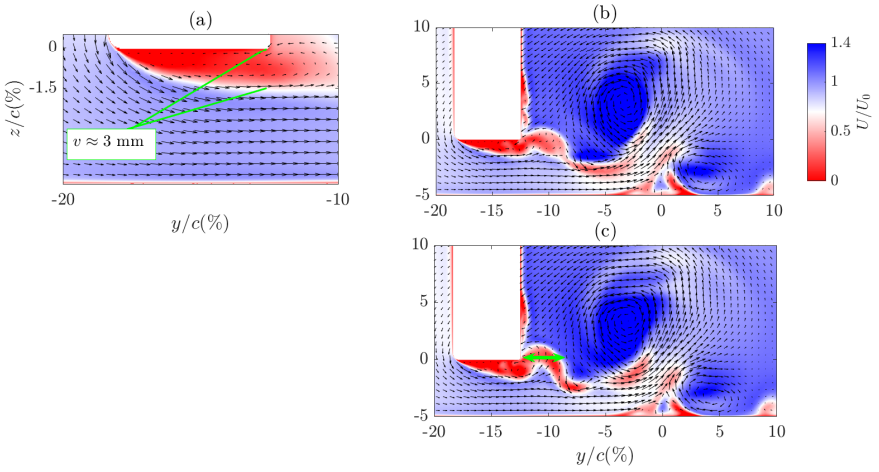

Figure 6.16: (a) Mean field of the axial velocity component U/U_0 obtained with LES for the aerofoil with the round tip at $x/c = 75\%$ section. Consecutive instantaneous flow fields, (b) and (c), obtained every 5000 time steps.

TLV still dominates the suction side region, with its moving away from the aerofoil surface corresponding to the development of the extended separated flow, identified by the axial velocity deficit below the tip. A localised spot of axial-velocity deficit is also observed in the suction side region between $y/c(\%) = -5$ and 0, resulting from the shedding of the separated flow itself, as seen for the square tip case. Specifically, this spot corresponds to that observed beyond the suction side in the experimental measurement in figure 5.14. The TSV below the aerofoil tip was not detected, as the hot-wire measurements were performed in a midgap plane.

6.4.2 SPOD, DMD and Covariance analysis

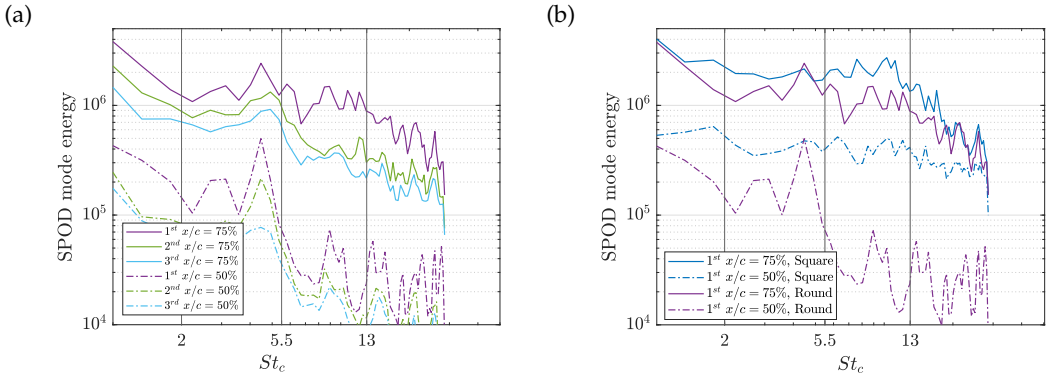

Figure 6.17: (a) SPOD mode energy spectra of the first three modes obtained for the two sections of the round case: $x/c = 50\%$ (continuous lines) and $x/c = 75\%$ (dashed lines). (b) Comparison of the energy spectra of the leading modes for the square and round tip at the two sections.

Figure 6.17 (a) displays the energy spectra of the first three SPOD modes for the two sections, at $x/c = 50\%$ and 75%, of the configuration with round tip. The shear layer

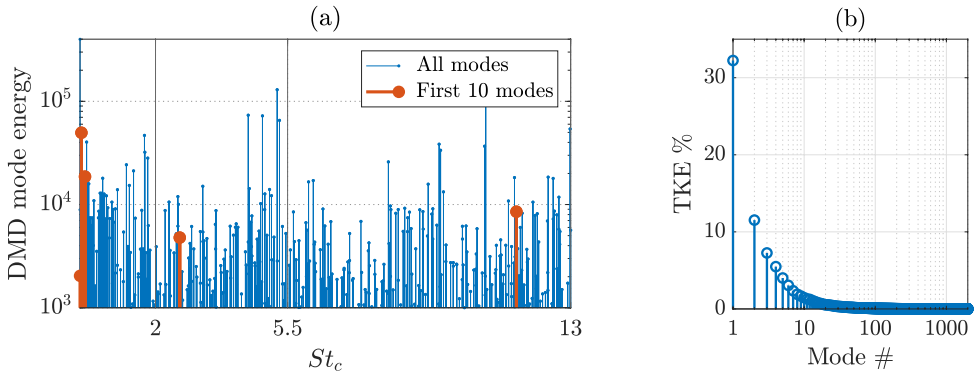

Figure 6.18: Round tip: (a) Amplitude spectra of all DMD modes (–) and of the first 10 modes (–). (b) Total Kinetic Energy from each mode.

roll-up is expected to occur at $x/c = 75\%$, due to the large distance between the leading and the second mode within the range $St_c = 5.5-13$. Figure 6.17 (b) compares the leading modes of these sections for both round and square tip configurations, highlighting differences in energy content. Overall, the leading modes in the round tip configuration are less energetic, with a slight reduction for the section at $x/c = 75\%$ and a significant drop for the midchord section. This huge reduction aligns with the flow topology observed at midchord in figure 6.15. The spectra estimation parameters have not been changed between the two configurations and can be found in table 6.1.

Figure 6.18 (a) displays the amplitude of all modes of the section at 75% of the chord for the round tip configuration. When compared to the square tip spectra in figure 6.11 (a), significantly higher amplitudes are observed within the frequency range of the first noise source, $St_c = 2$–5.5, particularly near the upper limit. This increase in frequency, together with the reduced length of the separated flow observed in figure 6.16 (a), keep the non-dimensional frequency associated with the first noise source, i.e. $St_v = fv/U_0 \approx 0.07$, approximately constant. However, when the decomposition is truncated to the first 10 modes, one DMD mode is found within this range at much lower frequency, $St_c = 2.6$. In this configuration, the first 10 modes account for almost 70% of the total energy of the system, as shown in figure 6.18 (b).

Focus on roll-up with SPOD

Figure 6.19 (a) displays the leading mode of the midchord section at $St_c = 10$, which is characterised by the absence of any flow mechanisms below the aerofoil tip, as also suggested by the drop in the energy spectra and the small distance between the spectra of the leading and second SPOD mode in figure 6.17 (a. No shear layer roll-up is observed, and no noise is generated at this station, as shown in the covariance plot in figure 6.19 (b). The plot reveals maximum covariance values that are significantly lower than those observed in figure 6.9 (b) for the square tip.

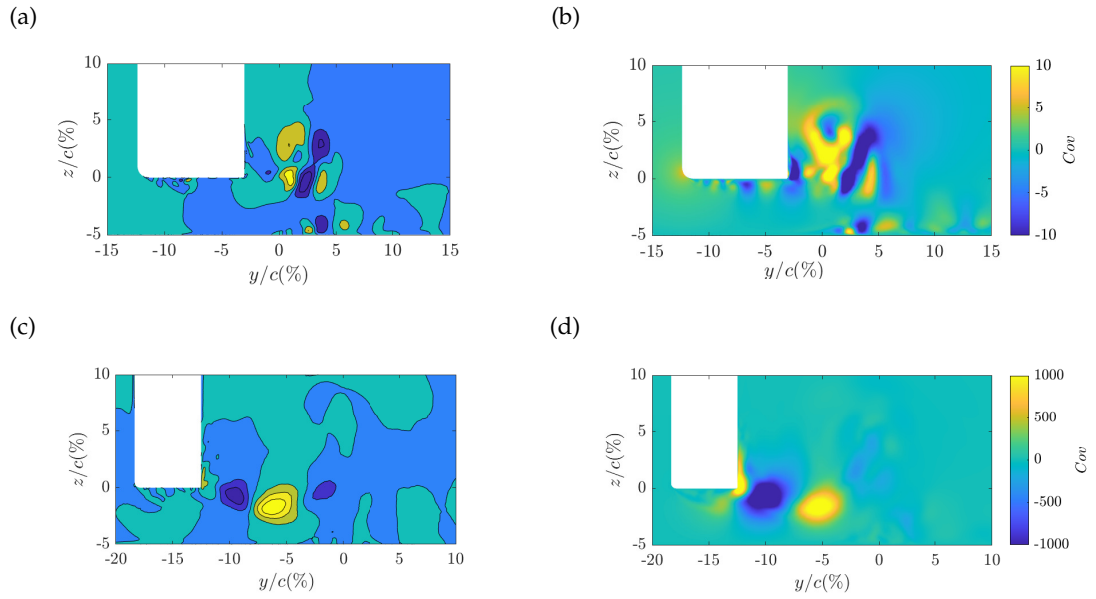

Figure 6.19: Round tip: (a) - (c) First SPOD mode of the $x/c = 50\%$ and 75% sections at the frequency of the second noise source, $St_c = 10$. (b) - (d) Covariance plot obtained for $x/c = 50\%$ and 75% sections by relating the velocity fluctuations in the z-direction with the pressure signal filtered in the frequency range of the second noise source $St_c = 5.5 - 13$.

The leading mode of the section at 75% of the chord is characterised by the two coherent structures in the suction side area, similar to what was observed for the square tip case in figure 6.10 (b). In the square configuration, these structures were interpreted as the downstream evolution of the pattern seen below the tip at midchord, figure 6.9 (a). In the round tip case, this pattern is not visible at midchord, but this does not necessarily mean it never forms. It may develop downstream of the 50% chord, with the coherent structures becoming visible at 75%. However, the key point is that the leading mode may still contribute to the second noise source, as suggested by its similarity with the covariance plot in figure 6.19 (d), but with slightly lower levels than those observed for the square tip case in figure 6.13 (b). The leading mode for the round tip is indeed less energetic.

In conclusion, the far-field noise reduction observed for the rounded case within the frequency of the second noise source can be attributed to two factors: the shear layer roll-up may develop further downstream and with less intensity compared to the square tip configuration.

Focus on vortex shedding with DMD

The dominant DMD mode of the section at 75% of the chord at $St_c = 2.6$ does not change significantly compared to that of the square tip, as shown respectively in figure 6.20 (a) and 6.12 (a). This was expected, as the instantaneous flow fields were also

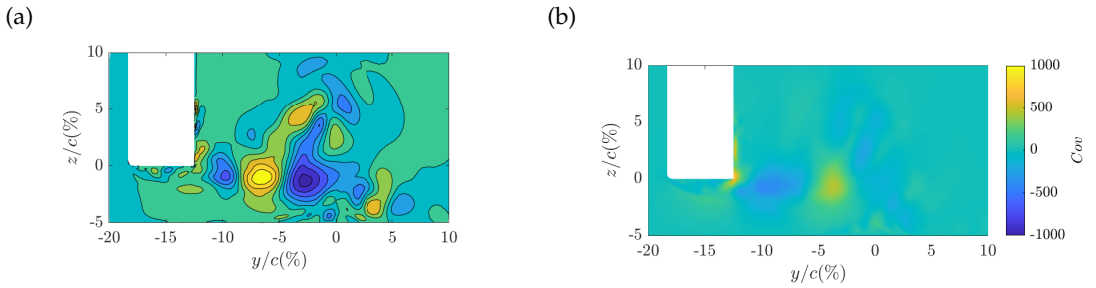

Figure 6.20: Round tip: (a) DMD mode of the $x/c = 75\%$ case at the frequency of the first noise source, $St_c = 2.6$. (b) Covariance plot obtained by relating the velocity fluctuations in the z-direction with the pressure signal filtered in the frequency range of the first noise source $St_c = 2 - 5.5$.

similar. Specifically, the DMD mode for the round case exhibits large coherent structures, which develop at the pressure side tip, are subsequently shed. However, the vortex shedding appears to be less intense, as evidenced by the lower covariance values shown in figure 6.20 (b) compared to those in figure 6.13 (a). This finally explains the noise reduction of the first noise source for the rounded configuration.

6.5 Conclusions

This chapter has numerically investigated the fluid dynamic instabilities, vortex shedding and shear layer roll-up, responsible for the two tip leakage noise sources of a stationary aerofoil and their change when the pressure side tip of the aerofoil is rounded.

In previous chapters, these instabilities were detected within the non-dimensional frequency ranges, $St_c = 2 - 5.5$ and $5.5 - 10$, and attributed to the behaviour of the tip flow after it separates at the aerofoil pressure side tip. Both instabilities occur when the flow does not reattach to the aerofoil, whereas only roll-up is observed if reattachment occurs. The tip leakage vortex influences the flow behaviour, not promoting the reattachment when it is far from the surface, downstream of the midchord. Rounding the pressure side corner led to changes in the mean flow field and reductions in both noise sources, although the underlying mechanisms behind these reductions were not yet fully understood.

Using LES, a novel and definitive overview of the tip flow within the gap in two cross-sections of the aerofoil is provided, overcoming the limitations of experimental flow measurements in such a confined area. SPOD and DMD decompositions highlight the two fluid dynamic instabilities in the flow field, while the covariance analysis, which correlates velocity and pressure fluctuations, confirms their role in the generation of the noise sources. Specifically, at the midchord section of the configuration with square tip, where the tip flow was found to reattach to the aerofoil surface, the leading SPOD

mode identifies a shear layer roll-up contributing to the second noise source, which instead disappears in the round tip section. Vortex shedding and roll-up are observed in the SPOD and DMD modes of both configurations with square and round tip at 75% chord section. Although the modes and the instantaneous flow fields are quite similar in the two configurations, both instabilities are less intense in the round case, which explains the reduction of the two noise sources measured in the experiments.

Chapter 7

Conclusions & Future works

Conclusions

This thesis investigates the physical mechanisms involved in the generation and reduction of the tip leakage noise for a single-stationary aerofoil, addressing the limited understanding in the literature. Through a combination of experimental, parametric, and numerical investigations, this research focuses on the fluid dynamic instabilities responsible for tip leakage noise sources, the parameters influencing these sources, and the effects of noise-reducing treatments.

Initially, the focus was on identifying the generating mechanisms of the tip leakage noise. Two dipole-type noise sources are identified in the pressure measurements as tip leakage noise sources, within two non-dimensional frequency ranges, $St_c = fc/U_0 = 2 - 5.5$ and $5.5 - 13$, where f is the frequency, c is the aerofoil chord length and U_0 is the inflow velocity. These noise sources are attributed to fluid-dynamic instabilities occurring within the gap: vortex shedding and shear layer roll-up. Both instabilities are linked to the behaviour of the tip flow after it separates at the aerofoil pressure side tip, once it enters the gap driven by the pressure difference across the aerofoil. The shear layer rolls up into discrete structures of size equivalent to the shear layer thickness b at the frequency of the second noise source. The associated non-dimensional frequency is $St_b = fb/U_{SL} = 0.2$, with U_{SL} representing the shear layer velocity. Subsequently, the separated flow can either reattach to the aerofoil or remain separated until the exit of the gap. In the case of extended separation, the vortical structures, after achieving a certain size, are shed at the non-dimensional frequency $St_v = fv/U_0 = 0.07$, where f is centred in the frequency range of the first noise source and v represents the size of the separated flow measured at the gap exit.

Once the mechanisms behind the tip leakage noise were identified, attention was then focused on the parameters influencing these noise sources. Three key non-dimensional

parameters are identified: the geometric angle of attack α, the ratio between maximum aerofoil thickness and gap size τ_{max}/e and the ratio between gap size and boundary layer thickness of the bottom wall e/δ. The first noise source develops when the tip flow does not reattach to the aerofoil, a condition that occurs when $\tau_{max}/e < 4$ and the tip leakage vortex is positioned far from the aerofoil surface for $\alpha \geq 10°$. The location of this vortex detachment is associated with the minimum pressure peak on the pressure distribution measured along the aerofoil suction side tip, which varies with α and τ_{max}/e. Also, the magnitude of this pressure peak, influenced by α, τ_{max}/e and e/δ, is linked to the noise source strength. The presence of this noise source is associated with high drag losses. The second tip noise source occurs whenever the tip flow separates at the pressure side. Its strength is mainly proportional to the lift coefficient C_l, depending on α, and it decreases as e/δ decreases and τ_{max}/e increases.

Following the identification of the mechanisms and parameters influencing the tip leakage noise, the focus shifted to evaluating noise-reducing treatments. Two treatments were examined, both obtained by modifying the aerofoil tip with porous material or by rounding the pressure side tip edge. The reduction of the first noise source with porous treatment is primarily due to changes in the flow field. On the contrary, the reduction achieved by the second noise source is attributed not only to changes in the flow field but also to the inherent damping properties of the porous material, with the reduction being function of the treatment thickness. However, significant reductions are achieved even with a 1.6 mm thick treatment.

Rounding the pressure side tip led to reductions in both tip sources by altering the flow field. Nevertheless, the experiments alone were not sufficient to fully identify the mechanisms behind this noise reduction. Numerical simulations provided a novel and definitive overview of the tip flow within the gap, highlighting the fluid dynamic instabilities responsible for the tip noise sources and their changes with a round pressure side tip. With round tip, both vortex shedding and roll-up persist but with lower intensity. Additionally, the reduction of the first noise source for the rounded case results in a reduction of drag losses, which is not observed for the porous tip due to the increased skin friction.

Future works

The recommendations for future work are listed as follows.

- To investigate the effect of the aerofoil curvature or winglets on the tip leakage flow and associated noise sources.
- To improve the semi-empirical law proposed by Decaix et al. (2015) for predicting the trajectory of the tip leakage vortex by using RANS simulations and incorporating the complete dataset of pressure distributions collected during this PhD.
- To further investigate the tip leakage noise for non-dimensional frequencies $St_c > 13$, a frequency range characterised by the absence of coherence patterns, as seen in Chapter 3.
- To compute the far-field noise spectra for the round tip case analysed with LES simulations using the FW-H analogy, and to numerically model and investigate the configuration with porous tip.
- To extend the exact Green's function for a rigid corner in a medium at rest to account for the tip flow within the gap, following an approach similar to that reported by Roger et al. (2016).
- To study the influence of the relative motion between the aerofoil and casing wall on the tip leakage noise sources, as occurs in a real fan. Previous experiments involving a moving wall demonstrated that wall motion influences the mean flow structures (Wang and Devenport, 2004). However, as these measurements were conducted downstream of the aerofoil trailing edge, they could not provide insight into the flow within the gap, where the fluid dynamic instabilities responsible for the noise sources occur for the steady aerofoil. Future research could address this "research gap" by examining the flow within the gap under moving wall conditions and assessing the performance of the noise reduction treatments assessed during this PhD.

Appendix A

Set-up and measurements techniques

This appendix provides additional details related to Chapter 2. It begins by describing the ISVR open jet wind tunnel used for aeroacoustic measurements, followed by details of the calibration procedure for the remote microphones and flow velocity measurement techniques, including PIV and HWA, with the latter employed to characterize the incoming boundary layer. Finally, it includes details about the quantification of the forces acting on the aerofoil.

A.1 Open jet-wind tunnel

The experiments were conducted at the Institute of Sound and Vibration Research's (ISVR) open-jet wind tunnel facility within an anechoic chamber measuring 8 m $\times$ 8 m $\times$ 8 m. The chamber's walls are acoustically treated with glass wool wedges, whose cut-off frequency is about 80 Hz. The nozzle has dimensions of 150 mm $\times$ 450 mm and a contraction ratio of $25:1$, providing a maximum flow speed of 100 m/s. The background noise is at least 10 dB below the aerofoil noise, and the free stream turbulence is less than 0.4% in the potential core of the nozzle. A detailed description of the wind tunnel, including its characteristics, is presented in Chong et al. (2009).

A.2 Remote probes calibration procedure

Remote microphone probes can be used to obtain accurate surface pressure measurements (Perennes and Roger, 1998). These probes are connected to surface pinholes via capillary tubes and flexible tubes, allowing pressure fluctuations to propagate from the

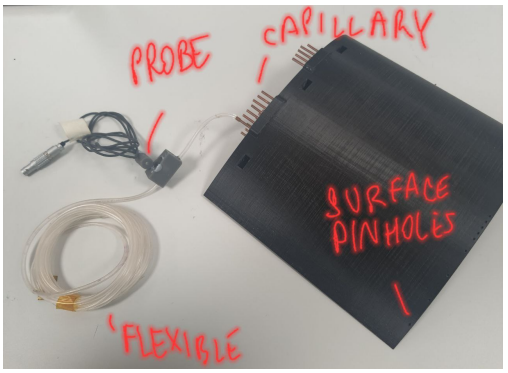

Figure A.1: Remote microphone probes connected to the aerofoil surface pinholes via capillary and flexible tubes.

aerofoil surface to the tube exits. The microphone diaphragm is connected to the flexible tubes via a 3D-printed block, as shown in detail in figure A.1. Long plastic tubes are also connected to the other end of this block to prevent acoustic reflections.

A calibration procedure is required for each probe to account for the time delay and amplitude attenuation caused by the propagation of acoustic waves in the tubes, as the pressure signals are acquired outside the aerofoil rather than directly on its surface. The broadband calibration procedure, similar to that proposed in Gruber (2012), is performed using an in-duct loudspeaker fed with white noise. First, the loudspeaker, with a reference microphone mounted flush to it, is sealed over the aerofoil pinholes. A $1/4$" GRAS microphone is used as a reference sensor, with a known sensitivity s_{ref}. The system's transfer function $H(s)$ in the frequency domain is evaluated using the following equation:

$$H(s) = \frac{V_p^{WN}(s)}{V_s^{WN}(s)} \tag{A.1}$$

where $V_p^{WN}(s)$ is the white noise signal recorded by the remote probe, while $V_s^{WN}(s)$ is that acquired by the reference microphone on the surface pinhole. The pressure acquired by the reference microphone is defined as $P_s(t) = V_s(t)/s_{ref}$. The transfer function $H(s)$ can then be used to evaluate the signal on the aerofoil surface in the presence of tip noise as follows:

$$V_s^{tip}(s) = \frac{V_p^{tip}(s)}{H(s)} \tag{A.2}$$

where V_p^{tip} is the tip noise signal recorded by the remote probe.

Note that the remote FG-23329-P07 sensors along the aerofoil suction side saturated for inflow velocity $U_0 > 20$ m/s, unlike those on the pressure side. This issue was solved by replacing them with a B&K type 4189 free-field microphone.

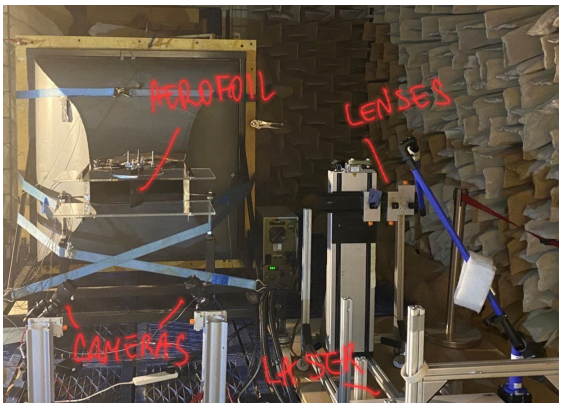

Figure A.2: Photo of the PIV set.

A.3 Flow velocity measurements

PIV pre-processing

PIV data are processed using DaVis 8.4 software. The images are first preprocessed to enhance the visibility of the seed particles by using several filters, including:

- correction of the intensity level of one of the two image pairs, due to the different intensities of two laser pulses;
- elimination of the background noise subtracting the minimum intensity from the source;
- dividing a constant value from each pixel of an image;
- filtering out the local mean background intensity leaving only the local fluctuations by using the subtract sliding minimum filter over a scale length of 64 pixels;
- applying 3×3 smoothing filter.

The vector field is calculated using a multi-grid cross-correlation scheme with a final window size of 16×16 pixels and 75% overlap. Each window contains approximately 7 particles. An elliptical weighting window, with a ratio $2 : 1$, is used to improve the signal-to-ratio of the cross-correlations. The maximum displacement of the particles is maintained above 15 pixels, which aligns with the guidelines reported in Adriann and Westerweel (2011), as this maximum displacement is nearly one-quarter of the size of the first pass interrogation window, which is 64×64 pixels.

PIV uncertainty analysis

Averaging is commonly used in aeroacoustics to focus on the expected values of the flow field. Therefore, it is essential to determine the number of averages required to

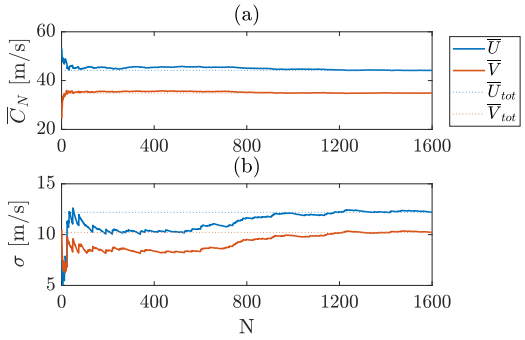

Figure A.3: Convergence history of the mean $\overline{C}$ (a) and of the standard deviation σ (b) of the absolute velocity U and V.

achieve reliable results and assess their accuracy. A convergence analysis is performed at a point of the flow field, similar to that conducted by Cavazzini et al. (2012) to validate PIV measurements in a centrifugal pump. On the contrary, an estimation of the confidence interval for the mean values is conducted across the entire flow field. The selected point is located in a high-turbulence region near the trailing edge for the baseline configuration. Figure A.3 (a) and (b) show the evolution of the average $\overline{C}_N$ and of the standard deviation σ_N of the absolute velocities U and V over the increasing number of samples:

$$\overline{C}_N = \frac{1}{N}\sum_{i=1}^{N} Ci \tag{A.3}$$

$$\sigma_N = \sqrt{\frac{1}{N}\sum_{i=1}^{N}(Ci - \overline{C}_{tot})} \tag{A.4}$$

where $\overline{C}_{tot}$ and σ_{tot} represent the average and standard deviation of the velocity over the total number of images, and N is the progressive number of snapshots with N_{tot} the total number of acquisitions. The mean velocities reach asymptotic values after approximately 1200 images, unlike the standard deviations, which exhibit a convergent trend. Convergence at other points in the flow field is achieved with fewer images, as this analysis is conducted at a point located in a high-turbulence region.

The validation of the PIV measurements includes estimating the confidence interval of the mean quantities to assess their reliability. Assuming a normal distribution for the mean error, the 95% confidence interval is determined as twice the standard deviation divided by the square root of the number of images, as shown in the following formula from Glegg and Devenport (2017).:

$$\delta[\overline{C}] = \frac{2 \times \sigma_{tot}}{\sqrt{N_{tot}}} \tag{A.5}$$

The uncertainty in the means of U and V are quantified and shown in Figure A.4 (a) and (b), respectively. The highest uncertainty values are concentrated around the midchord and in the suction-side region near the trailing edge, where high turbulence levels are

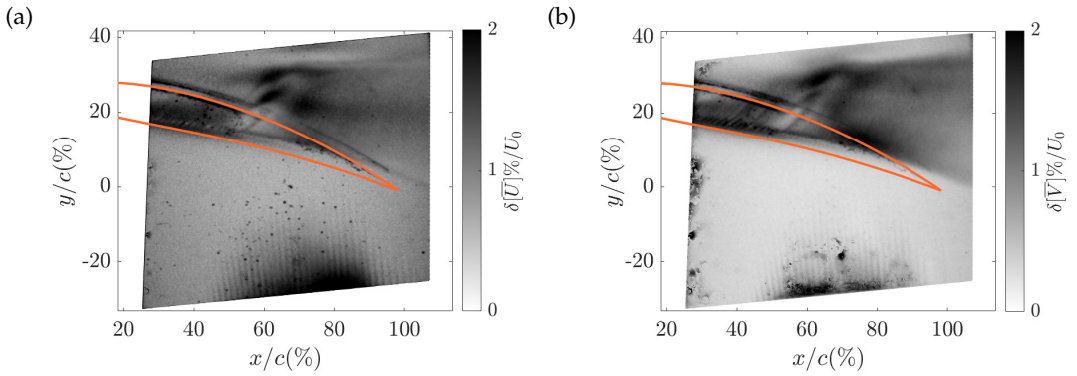

Figure A.4: PIV contours of the uncertainty in mean of U and V velocities for the baseline configuration.

found in Saraceno et al. (2022, p. 8) Additional high values are detected along the suction side, likely due to aerofoil reflections. The lowest uncertainties are associated to the V-velocity and are found in the pressure side region, where cross-stream flow is minimal.

Also, PIV algorithms have an inherent random error in determining particle displacement, independent of the number of samples, estimated at approximately 0.1 pixels according to Adriann and Westerweel (2011). The random error in velocity measurements is calculated to be 1.57% of the free stream velocity U_0, using the following formula:

$$\epsilon = \frac{0.1 \times M}{dt} \tag{A.6}$$

where $M = 0.176$ mm/pixel is the image magnification and $dt = 7$ μs is the time between two image pairs.

Hot-wire calibration and validation

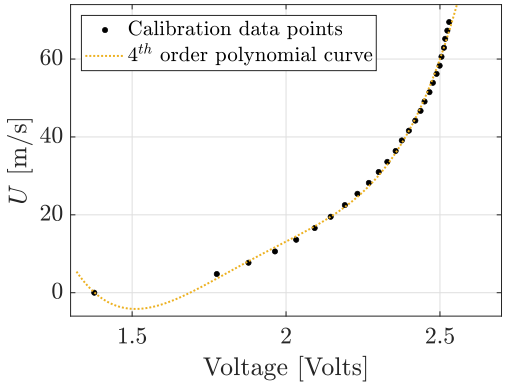

Figure A.5: Calibration of the hot-wire probe.

Calibration establishes a relationship between the voltage output from the hot-wire probe and the flow velocity. This process involves measuring the probe output at a series of know jet velocities, including the voltage at zero velocity, which are measured using a static Pitot tube. The goal is to find a fitting curve that enables the conversion of data records from voltages into velocities. An example of the calibration curve, used in Chapter 4, is plotted in figure A.5. An overheat ratio of 1.5 has been adjusted prior to the data acquisition.

The probe signals were acquired for 10 s at a sampling frequency of 10 kHz to ensure convergence of the mean statistics. For uncertainty estimation, Jorgensen (2005) provides guidelines to estimate the uncertainty of a velocity sample U, a combination of the uncertainty from multiple factors σ_i. The major contributions from calibration, curve fitting and temperature variations in the flow:

$$\delta[U] = 2 \times \sum_i \sigma_i \approx 2 \times (\sigma_{cal} + \sigma_{curve} + \sigma_{temp}) \tag{A.7}$$

where $\sigma_{cal} = \pm 2\%$ using a Pitot-static tube with a calibrated manometer for a velocity higher than 2 m/s; $\sigma_{curve} = 3.6\%$ is the standard deviation of the errors of the fitting curve in figure A.5; and $\sigma_{temp} \approx 0$ as the temperature varies less than $\pm 0.5\ ^{\circ}C$.

A.4 Inflow boundary layer

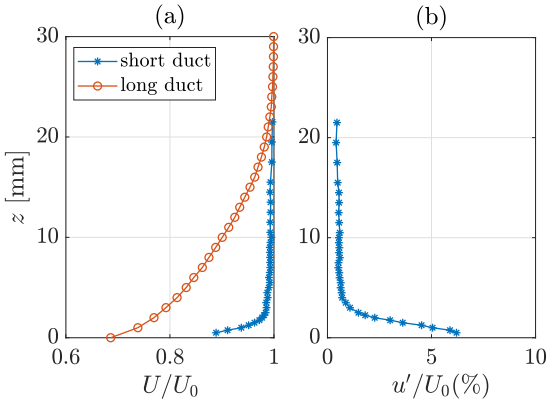

Figure A.6: (a) Stream-wise velocity profile and (b) rms velocity fluctuations measured at the leading edge of the aerofoil for inflow velocity $U_0 = 40$ m/s.

The flow characteristics of the incoming boundary layer were measured using HWA at the location of the aerofoil's leading edge, which had been removed. The stream-wise velocity profile (U/U_0) and the corresponding turbulence levels (u'/U_0) in the span-wise direction are plotted in figure A.6 (a) and (b). The boundary layer is fully turbulent with a thickness of $\delta \approx 5$ mm and an associated displacement thickness of $\delta* \approx 0.5$

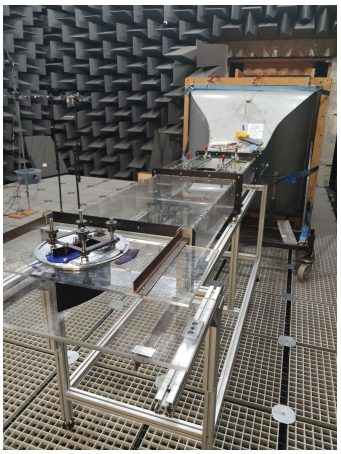

Figure A.7: Photo of the two meters duct attached at the nozzle exit of the open jet wind tunnel in ISVR.

mm. The maximum turbulence level (6.2%) occurs near the bottom wall, so the interaction noise between the boundary layer turbulence and the aerofoil leading edge can be considered small. The boundary layer thickness was increased to $\delta \approx 20$ mm, as shown in figure A.6 (a), by inserting a 2-meter-long duct between the nozzle exit and the aerofoil shown in figure A.7.

A.5 Aerodynamic forces

The load cell was calibrated before collecting any data by attaching a known weight to the aerofoil setup and verifying that the load cell returned the correct force. Additionally, the load cell was zeroed before each run, as changing the angle of attack during the tests could cause slight displacements between the mounting bracket and the load cell, potentially altering the reference value of the sensor and affecting the accuracy of the force measurements.

Calibration was performed along two axis, one perpendicular to the aerofoil chord and the other along it, as the load cell measures forces in these directions, F_1 and F_2 respectively. The lift and draft are then calculated from F_1 and F_2 as:

$$L = F_1 \cos(\alpha_{eff}) - F_2 \sin(\alpha_{eff}) \tag{A.8}$$

$$D = F_1 \sin(\alpha_{eff}) + F_2 \cos(\alpha_{eff}) \tag{A.9}$$

where α_{eff} is the effective angle of attack of the aerofoil. This angle is lower than the geometric angle of attack α, which is set using the rotating disk, due to the wind tunnel deflection (Glegg and Devenport, 2017).

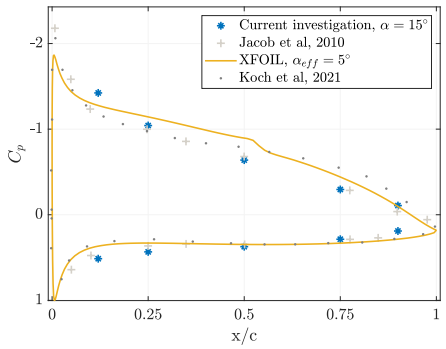

Figure A.8: Pressure distribution along the aerofoil measured at midspan and at $\alpha = 15°$ in the current investigation and in the others (Jacob et al., 2010; Koch et al., 2021), together with the numerical one obtained with XFOIL at $\alpha_{eff} = 5°$.

α	0	2.0	5.0	7.0	10	12	15	17	20
α_{eff}	-0.9	0	1.3	2.2	3.5	4.4	5.7	6.6	8.1

Table A.1: Geometric angle of attack α with the corresponding effective α_{eff}.

The effective angle of attack is determined by matching the experimental pressure distributions C_p measured along the midspan, where the influence of the tip flow is negligible, with the numerical ones computed using XFOIL (Drela, 1989). The simulations were run considering NACA 5510 aerofoil, at Reynolds number of $Re = 5.6 \times 10^5$ and Mach number of $M = 0.12$. Figure A.8 presents the experimental C_p distribution from the current investigation, along with the best-matching numerical distribution and additional measurements from the literature (Jacob et al., 2010; Koch et al., 2021). The effective angle of attack results approximately one-third of the geometric angle of attack. Table A.1 lists both the geometric and the corresponding effective angles of attack. Due to the limited number of experimental distributions available, several effective angles of attack were extrapolated.

Appendix B

Additional numerical results

This appendix provides additional plots resulting from the numerical simulations. Section B.1 contains the SPOD energy spectra of the two sections for different N_{fft}. Section B.2 contains the covariance plots obtained at the midchord section by correlating the velocity fluctuations in the three directions, with the filter and unfiltered pressure signals in the frequency range of the second noise source. Section B.3 provides additional covariance plots using filtered and unfiltered pressure signals, as well as evaluating pressure fluctuation in different points of the flow field. These plots pertain to the section located at 75% of the chord.

B.1 SPOD mode energy

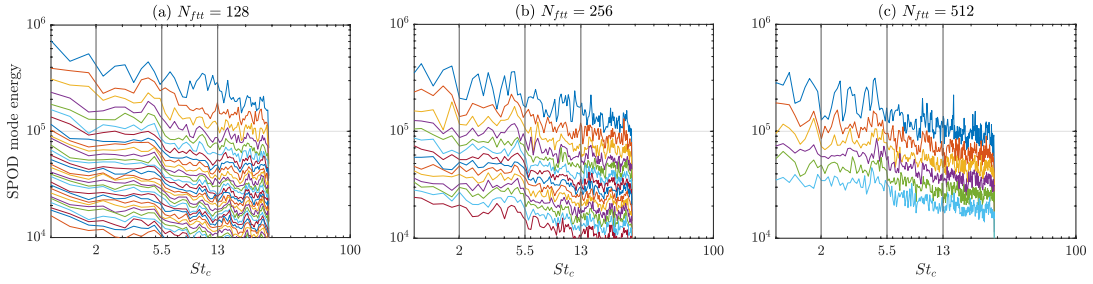

Figure B.1: SPOD mode energy spectra for the section at $x/c = 50\%$ with different N_{ftt}.

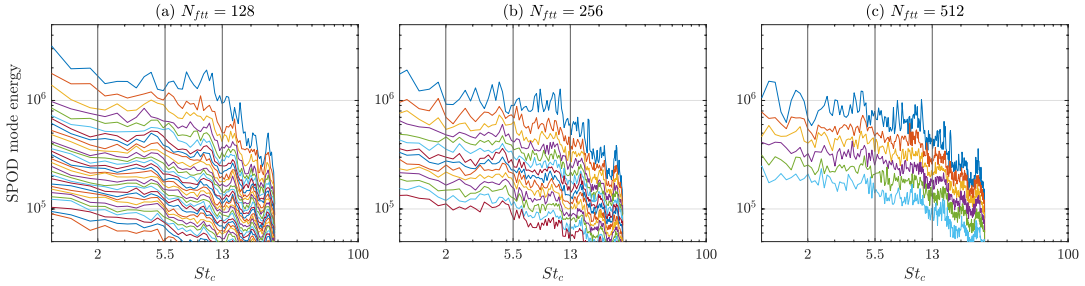

Figure B.2: SPOD mode energy spectra for the section at $x/c = 75\%$ with different N_{ftt}.

B.2 Covariance analysis on midchord section

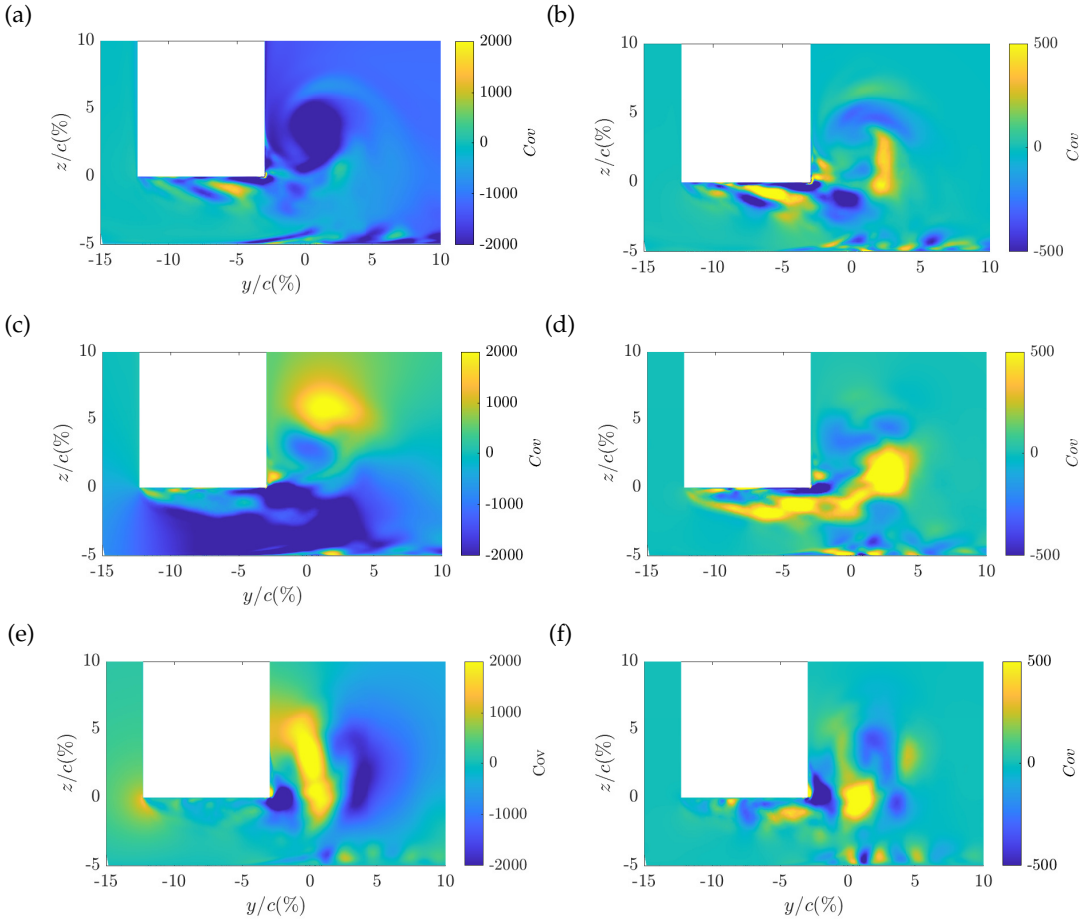

Figure B.3: Covariance plots obtained by relating the velocity fluctuations at $x/c = 50\%$ in the x-direction, (a) - (b), in y-direction, (c) - (d), and z-direction, (e) - (f) with the pressure signal recorded in the point P of $(y/c, z/c) = (-2.9\%, 0)$. On the left, the pressure signals are not bandpass filtered, on the right they are filtered in the frequency range of the second noise source, $St_c = 5.5 - 13$.

B.3 Covariance analysis on section at $x/c = 75\%$

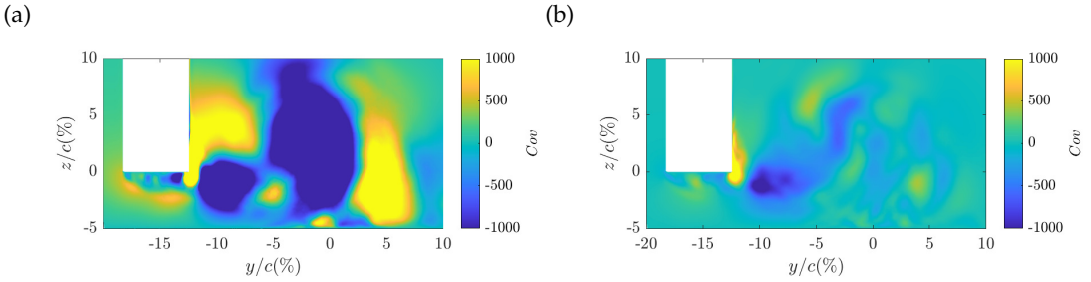

Figure B.4: Covariance plots obtained by relating the velocity fluctuations at $x/c = 75\%$ in the z-direction with the pressure signal recorded in the point P of $(y/c, z/c) = (-12.4\%, 0)$. On the left, the pressure signals are not bandpass filtered, on the right they are filtered in the frequency range of the first tip noise source, $St_c = 2 - 5.5$.

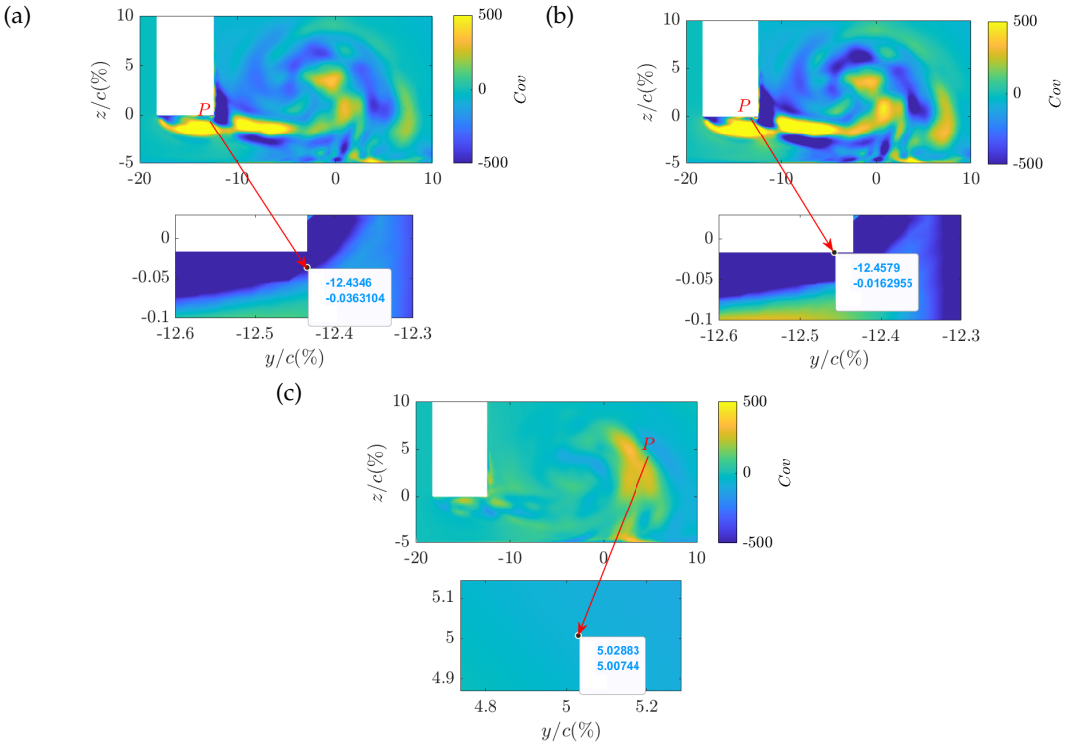

Figure B.5: Covariance plots obtained by relating the velocity fluctuations at $x/c = 75\%$ in the x-direction with the pressure signal recorded near the suction side tip, at $(y/c, z/c) = (-12.43\%, -0.036\%)$ (a) and in $(y/c, z/c) = (-12.46\%, -0.017\%)$ (b), and far from it, at $(y/c, z/c) = (-5.03\%, 5.01\%)$ (c). The pressure signals are bandpass filtered in the frequency range of the first tip noise source, $St_c = 2 - 5.5$.

References

Adriann, R. J. and Westerweel, J. (2011). *Particle Image Velocimetry*.

Amiet, R. K. (1975). Noise due to turbulent flow past a trailing edge. *J. Sound Vib.*, 47:387–393.

Angland, D., Zhang, X., and Molin, N. (2009). Measurements of flow around a flap side edge with porous edge treatment. *AIAA Journal*, 47:1660–1671.

Astley, R., Sugimoto, R., and Gabard, G. (2014). The effect of steady flow distortion on mode propagation in a turbofan intake. *AIAA Journal*.

Becherucci, L., Koch, R., and Moreau, S. (2022). Wall-resolved les of a linear compressor cascade with moving endwall. *28th AIAA/CEAS Aeroacoustics 2022 Conference*.

Bi, Z., Bao, F., Zhang, L., Shao, X., and Li, S. (2024). Numerical study of porous tip treatment in suppressing tip clearance vortices in cavitating flow. *Physics of Fluids*, 36:045117.

Bindon, J. P. (1989). The measurement and formation of tip-clearance loss. *J. Turbomach.*, 111:257–263.

Bindon, J. P. and Morphis, G. (1992). The development of axial turbine leakage loss for two profiled tip geometries using linear cascade data. *Journal of Turbomachinery*, 114:198–203.

Boudet, J., Cahuzac, A., Kausche, P., and Jacob, M. C. (2015). Zonal large-eddy simulation of a fan tip-clearance flow, with evidence of vortex wangering. *ASME*, 137:1–9.

Boudet, J., Caro, J., Li, B., Jondeau, E., and Jacob, M. C. (2016). Zonal large-eddy simulation of a tip leakage flow. *Intl J. Aeroacoustics*, 15:646–661.

Camussi, R., Grilliat, J., Caputi-Gennaro, G., and Jacob, M. C. (2010). Experimental study of a tip leakage flow: Wavelet analysis of pressure fluctuations. *J. Fluid Mech.*, 660:87–113.

Carpio, A. R., Martínez, R. M., Avallone, F., Ragni, D., Snellen, M., and van der Zwaag, S. (2019). Experimental characterization of the turbulent boundary layer over a porous trailing edge for noise abatement. *Journal of Sound and Vibration*, 443:537–558.

Cavazzini, G., Dazin, A., Pavesi, G., Dupont, P., and Bois, G. (2012). Post-Processing Methods of PIV Instantaneous Flow Fields for Unsteady Flows in Turbomachines. *The Particle Image Velocimetry - Characteristics, Limits and Possible Applications*.

Chong, T. P., Joseph, P., and Davies, P. O. A. L. (2009). Design and performance of an open jet wind tunnel for aero-acoustic measurements. *Applied Acoustics*, 70:605–614.

Choudhari, M. and Khorrami, M. R. (2003). Computational study of porous treatment for altering flap side-edge flowfield. In *9th AIAA/CEAS Aeroacoustics Conference*, Hilton Head, South Carolina.

Colin, R. (2000). *Simulations aux grandes échelles de la combustion turbulente prémé- langée dans les statoréacteurs.* PhD thesis, INPT, Toulouse, FRANCE.

Collin, D., Bauer, M., Bergmans, D., Brok, P., Brouwer, H., Dimitriu, D., Gely, D., Humphreys, N., Kors, E., Lemaire, S., Lempereur, P., Mueller, U., and Van OOsten, N. (2016). Overview of aviation noise research effort supported by the european union. Technical report, ICAO Environmental Report.

Dambach, R. and Hodson, H. P. (2001). Tip leakage flow in a radial inflow turbine with varying gap height. *Journal of Propulsion and Power*, 17:644–650.

Decaix, J., Balarac, G., Dreyer, M., Farhat, M., and Münch, C. (2015). Rans and les computations of the tip leakage vortex for different gap width. *J. Turbulence*, 16:309–341.

Denton, J. D. (1993). Loss mechanisms in turbomachines. *Journal of Turbomachinery*, 115(4):621–656.

Donea, J. (1984). A taylor–galerkin method for convective transport problems. *International Journal for Numerical Methods in Engineering*.

Drela, M. (1989). Xfoil: An analysis and design system for low reynolds number airfoils. In *Low Reynolds Number Aerodynamics*, pages 1–12. Springer Berlin Heidelberg.

Driver, D. M., Seegmiller, H. L., and Marvin, J. G. (1986). Time-dependent behaviour of a reattaching shear layer. *AIAA J.*, 25:914–919.

Ganz, U. W., Joppa, P. D., Patten, T. J., and Scharpf, D. F. (1998). Boeing 18-inch fan rig broadband noise test. Technical Report 208704, NASA.

Gerrard, J. H. (1955). Measurements of the sound from circular cylinders in an air stream. *Proc. Phys. Soc. B*, 68:453–461.

Geyer, T., Lucius, A., Schrödter, M., Schneider, M., and Sarradj, E. (2019). Reduction of turbulence interaction noise through airfoils with perforated leading edges. *Acta Acustica united with Acustica*, 105:109–122.

Geyer, T., Sarradj, E., and Fritzsche, C. (2010). Porous airfoils: Noise reduction and boundary layer effects. *International Journal of Aeroacoustics*, 9:787–820.

Geyer, T., Sarradj, E., Giesler, J., and Hobracht, M. (2011). Experimental assessment of the noise generated at the leading edge of porous airfoils using microphone array techniques. In *17th AIAA/CEAS Aeroacoustics Conference*, Portland, Oregon.

Glegg, S. and Devenport, W. (2017). *Aeroacoustics of Low Mach Number Flows*. Academic Press.

Graham, J. A. H. (1986). Investigation of a tip clearance cascade in a water analogy rig. *ASME*, 108:38–46.

Grilliat, J., Jacob, M. C., Camussi, R., and Caputi-Gennaro, G. (2007). Tip leakage experiment - part one: Aerodynamic and acoustic measurements. In *13th AIAA/CEAS Aeroacoustics Conference*, Rome, Italy.

Gruber, M. (2012). *Airfoil noise reduction by edge treatments*. PhD thesis, University of Southampton.

Guo, Q., Zhou, L., and Wang, Z. (2016). Numerical evaluation of the clearance geometries effect on the flow field and performance of a hydrofoil. *Renewable Energy*, 99:390–397.

Henning, A., Kaepernick, K., Ehrenfried, K., Koop, L., and Dillmann, A. (2008). Investigation of aeroacoustic noise generation by simultaneous particle image velocimetry and microphone measurements. *Experiments in Fluids*, 45:1073–1085.

Heyes, F. J. G., Hodson, H. P., and Dailey, G. M. (1992). The effect of blade tip geometry on the tip leakage flow in axial turbines cascades. *Journal of Turbomachinery*, 114:643–651.

Higgens, A., Joseph, P., Lidtke, A. K., and Turnock, S. R. (2019). Investigation into the tip-gap flow and its influence on ducted propeller tip- gap noise using acoustic analogies. *Journal of Ship Research*, 00:1–16.

Howe, M. S. (2002). *Theory of Vortex Sound*. Cambridge University Press.

Hubbard, H. H. (1991). Aeroacoustics of flight vehicles: Theory and practise. vol 1: Noise sources. Technical report, NASA Langley Research Center.

Hudy, L. M., Naguib, A., and Humphreys, W. M. (2007). Stochastic estimation of a separated-flow field using wall-pressure-array measurements. *Physics of fluids*, 19:024103.

Hughes, C. E., Woodward, R. P., and Podboy, G. G. (2005). Effect of tip clearance on fan noise and aerodynamic performance.

Inoue, M., Furukawa, M., Saiki, K., and Yamada, K. (1998). Physical explanations of tip leakage flow field in an axial compressor rotor. *ASME 1998 International Gas Turbine and Aeroengine Congress and Exhibition*.

Intaratep, N. (2006). *Formation and Development of the Tip Leakage Vortex in a Simulated Axial Compressor with Unsteady Inflow*. PhD thesis, Virginia Polytechnic Institute.

Jacob, M. C., Grilliat, J., Camussi, R., and Caputi-Gennaro, G. (2010). Aeroacoustic Investigation of a Single Airfoil Tip Leakage Flow. *Intl J. Aeroacoustics*, 9:253–272.

Jacob, M. C., Jondeau, E., and Li, B. (2016a). Time-resolved piv measurements of a tip leakage flow. *Intl J. Aeroacoustics*, 15:662–685.

Jacob, M. C., Jondeau, E., Li, B., and Boudet, J. (2016b). Tip leakage flow: Advanced measurements and analysis. In *17th AIAA/CEAS Aeroacoustics Conference*, Portland, Oregon.

Jorgensen, F. E. (2005). *How to measure turbulence with hot-wire anemometers - a practical guide*. Dantec Dynamics.

Kang, S. and Hirsch, C. (1993). Experimental study on the three-dimensional flow within a compressor cascade with tip clearance: Part i - velocity and pressure fields. *ASME*, 115:435–443.

Kang, S. and Hirsch, C. (1994). Tip leakage flow in linear compressor cascade. *ASME*, 116:657–664.

Khorrami, M. R., Li, F., and Choudhari, M. (2002). Novel approach for reducing rotor tip-clearance-induced noise in turbofan engines. *AIAA Journal*, 40:1518–1528.

Koch, R. (2021). *Identification des sources de bruit aérodynamique liées aux écoulements de jeu en tête de pale de soufflante de turboréacteur*. PhD thesis, Université de Sherbrooke, Sherbrooke, QC, CANADA.

Koch, R., Sanjosé, M., and Moreau, S. (2022). Numerical aeroacoustic analysis of a linear compressor cascade with tip gap. *AIAA Journal*.

Koch, R., Sanjosé, M., and Moreau, S. (2021). Large-eddy simulation of a single airfoil tip-leakage flow. *AIAA J.*, 59:2546–2557.

Kostas, J., Soria, J., and Chong, M. S. (2002). Particle image velocimetry measurements of a backward-facing step flow. *Experiments in Fluids*, 33:838–853.

Kundu, P. K., Cohen, I. M., and Dowling, D. R. (2016). *Fluid Mechanics (Sixth Edition)*. Academic Press.

Laborde, R., Chantrel, P., and Mory, M. (1997). Tip clearance and tip vortex cavitation in an axial flow pump. *Journal of Fluids Engineering*, 119:680–685.

Lax, P. and Wendroff, B. (1960). System of conservation laws. *Communications on Pure and Applied Mathematics*.

Lee, S., Ayton, L., Bertagnolio, F., Moreau, S., Chong, T. P., and Joseph, P. (2021). Turbulent boundary layer trailing-edge noise: Theory, computation, experiment, and application. *Progress in Aerospace Sciences*, 126:1–56.

Liu, Y., Wang, Z. N., Tan, L., Tucker, P. G., and Moller, F. M. (2024). Tip-leakage-flow unsteadiness and associated control. *Physics of fluids*, 36:055156.

Liu, Y. Z., Kang, W., and Sung, H. J. (2005). Assessment of the organization of a turbulent separated and reattaching flow by measuring wall pressure fluctuations. *Experiments in Fluids*, 38:485–493.

Lockard, D. and Lilley, G. (2004). The airfram noise reduction challenge. Technical report, NASA Technical report.

Ma, C. H., Awasthi, M., Moreau, D., and Doolan, C. (2023). Aeroacoustics of turbulent flow over a forward-backward facing step. *J. Sound Vib.*, 563:117840.

Mann, A., Kim, M. S., Wu, J., and Perot, F. (2016). Airfoil tip leakage aeroacoustics predictions using a lattice boltzmann based method. In *22nd AIAA/CEAS Aeroacoustics Conference*, Lyon, France.

Mockett, C., Knacke, T., and Thiele, F. (2010). Detection of initial transient and estimation of statistical error in time-resolved turbulent flow data. *Proceedings of the 8th International Symposium on Engineering Turbulence Modelling and Measurements*.

Moore, J. and Tilton, J. (1988). Tip leakage flow in a linear turbine cascade. *ASME*, 110:18–26.

Moreau, S. (2019). Turbomachinery noise predictions: Present and future. *Acoustics*.

Moreau, S. and Roger, M. (2018). Advanced noise modelling for future propulsion systems. *Intl J. Aeroacoustics*, 17:576–599.

Muthanna, C. and Devenport, W. J. (2004). Wake of a compressor cascade with tip gap. part 1: Mean flow and turbulence structure. *AIAA J.*, 42:2320–2331.

Nicoud, F. and Ducros, F. (1999). Subgrid-scale stress modelling based on the square of the velocity gradient tensor. *Flow, turbulence and Combustion*, 62:183–200.

Odier, N., Sanjose, M., Gicquel, L., Poinsot, T., Moreau, S., and Duchaine, F. (2019). A characteristic inlet boundary condition for compressible, turbulent, multispecies turbomachinery flows. *Computers and Fluids*, 178:41–55.

Palleja-Cabre, S., Saraceno, I., and Chaitanya, P. (2024). On the modification of tip leakage noise sources by over-tip liners. *Physics of Fluids*, 36:026114.

Palleja-Cabre, S., Saraceno, I., Chaitanya, P., and Joseph, P. (2022). Reduction of tip-leakage noise by using porosity. In *28th AIAA/CEAS Aeroacoustics 2022 Conference*, Southampton, Uk.

Peake, N. and Parry, A. B. (2012). Modern challenges facing turbomachinery aeroacoustics. *Annual Review of Fluid Mechanics*, 44:227–248.

Perennes, S. and Roger, M. (1998). Aerodynamic noise of a two-dimensional wing with high-lift devices. In *4th AIAA/CEAS Aeroacoustics Conference*.

Rains, D. (1954). *Tip Clearance Flow in Axial Compressors and Pumps*. PhD thesis, California Institute of Technology.

Roger, M., Moreau, S., and Kucukcoskun, K. (2016). On sound scattering by rigid edges and wedges in a flow, with applications to high-lift device aeroacoustics. *Journal of Sound and Vibration*, 362:252–275.

Sagaut, P. (2006). Large eddy simulation for imcompressible flows: An introduction. *Springer Science and Business Media*.

Saraceno, I., Palleja-Cabre, S., Chaitanya, P., Jaiswal, P., and Ganapathisubramani, B. (2022). On the tip leakage noise generating mechanisms of single-fixed aerofoil. In *28th AIAA/CEAS Aeroacoustics Conference*, Southampton, United Kingdom.

Scarano, F., Benocci, C., and Riethmuller, M. L. (1999). Pattern recognition analysis of the turbulent flow past a backward facing step. *Physics of fluids*, 11:3808–3818.

Schabowski, Z. and Hodson, H. (2007). the reduction of over tip leakage loss in unshrouded axial turbines using winglets and squealers. In *ASME Turbo Expo*, Montreal, Canada.

Schmid, P. (2010). Dynamic mode decomposition of numerical and experimental data. *Journal of Fluid Mechanics*, 656:5–28.

Schmidt, O. T. and Colonius, T. (2020). Guide to spectral proper orthogonal decomposition. *AIAA J.*, 58:1023–1033.

Schønfeld, T. and Rudgyard, M. (1999). Steady and unsteady flow simulations using the hybrid flow solver avbp. *AIAA Journal*.

Storer, J. A. and Cumpsty, N. A. (1991). Tip leakage flow in axial compressors. *ASME*, 113:252–259.

Sutliff, D. L., Bozak, R. F., Jones, M. G., and Nark, D. M. (2021). Investigations of three over-the-rotor liner concepts at various technology readiness levels. *International Journal of Aeroacoustics*, 20:826–866.

Taira, K., Brunton, S. L., Dawson, S. T. M., Rowley, C. W., Colonius, T., McKeon, B. J., Schmidt, O. T., Gordeyev, S., Theofilis, V., and Ukeiley, L. S. (2017). Modal analysis of fluid flows: An overview. *AIAA Journal*, 55(12):4013–4041.

Towne, A., Schmidt, O. T., and Colonius, T. (2018). Spectral proper orthogonal decomposition and its relationship to dynamic mode decomposition and resolvent analysis. *Journal of Fluid Mechanics*, 847:821–867.

Wang, Y. and Devenport, W. J. (2004). Wake of a compressor cascade with tip gap. part 2: Effects of endwall motion. *AIAA J.*, 42:2332–2340.

Wee, D., Yi, T., Annaswamy, A., and Ghoniem, A. F. (2004). Self-sustained oscillations and vortex shedding in backward-facing step flows: Simulation and linear instability analysis. *Physics of Fluids*, 16:3361–3373.

Weiss, J. (2019). A tutorial on the proper othogonal decomposition. In *AIAA Aviation Forum*, Dallas, Texas.

Winant, C. D. and Browand, F. K. (1974). Vortex pairing: the mechanism of turbulent mixing-layer growth at moderate reynolds number. *J. Fluid Mech.*, 63:237–255.

You, D., Wang, M., Moin, P., and Mittal, R. (2007). Vortex dynamics and low-pressure fluctuations in the tip-clearance flow. *ASME*, 129:1002–1014.

Zhang, B., Liu, B., Mao, X., Wang, H., Yang, Z., and Li, Z. (2022). Interaction mechanism between the tip leakage flow and inlet boundary layer in a highly loaded compressor cascade based on scale-adaptive simulation. *Physics of Fluids*, 34:116112.